Investigation of nanostructural dynamics and rigidity percolation in network glasses

(ネットワークガラスにおけるナノ構造のダイナミクスと硬さのパーコレションの研究)

by

Toshihiro Nakaoka　　中岡　俊裕

Dissertation in Physics

The Osaka University

Graduate School of Science

2001

Table of Contents

List of Figures

List of Tables

Acknowledgements

There are numerous people who were instrumental in assisting the author to finally complete this degree. First, the author wishes to express his sincere gratitude for the valuable suggestions, continuous encouragements and supports from Prof. Kazuo Murase throughout this research. He is very indebted to Dr. Osamu Matsuda for guidance on the experiments, and Dr. Yong Wang for valuable advice in this research and writing this manuscript. He is also grateful to Dr. Sadao Takaoka and Dr. Kenichi Oto for their various suggestions on the experiments and stimulating discussion.

The author would like to acknowledge Dr. Koichi Inoue for his advise and helpful discussion, Dr. Popović for providing high-quality crystalline $GeSe_2$ grown by Bridgman technique, and Dr. Mitsutaka Nakamura for helpful remarks. He also thanks Mr. Tatsuya Komamine, Mr. Hirotaka Murakami, Mr. Kohei Tanaka, Mr. Syunsuke Murakami, and Mr. Masaki Nakamura, for their assistance in experiments and their help with some of the lab works. Finally, it is a pleasure to thank all the members of the Murase group for their friendly encouragement and interesting discussion.

Abstract

Interrelationship between physical properties and structures of disordered systems is one of the main problems in condensed matter physics. We investigate structural changes induced by heating and/or light irradiation in Ge_xSe_{1-x} network glasses by means of Raman scattering and photoluminescence measurements. We propose concrete nanoscopic structures which play essential role on the thermally- and photo-induced structural changes, respectively. We show (i) how the compositional variation of the nanoscopic units affects the structural changes, and (ii) the difference between the thermally- and photo-induced structural changes.

First, we investigate the compositional dependences of Raman spectra at high temperatures (30°C $\sim$ 480°C) including the glass transition temperatures (T_g). We characterize the Ge_xSe_{1-x} glasses by the average coordination number $\langle r \rangle$ according to the constraint counting theory which predicts a mechanical transition $\langle r \rangle = 2.40$, or $x = 0.20$ from the *floppy* networks ($\langle r \rangle < 2.40$, or $x < 0.20$) to the *rigid* ones ($\langle r \rangle > 2.40$, or $x > 0.20$). We find that the spectral profiles of low-frequency Raman spectra of floppy glasses changes with temperature in a definitely different manner from that of rigid glasses does. Only in the floppy glasses "relaxational modes" can be observed in the quasielastic scattering range. The origin of the relaxational modes is attributed mainly to the rotational degrees of freedom in Se_n ($n > 2$) segments. We propose that the decrease of the number of the Se_n ($n > 2$) segments with $\langle r \rangle$ is essential for the rigidity transition. In addition, we report a study of the resonant Raman scattering of Ge_xSe_{1-x} glasses at room temperature, and show that the decrease of the number of Se_n ($n > 2$) segments is consistent with the compositional dependence of the resonant Raman spectra.

Next, we study structural changes at a fixed average coordination. We focus on the structural changes of stoichiometric $GeSe_2$ glass upon heating towards crystallization temperature We investigate them for 50 samples by low- (10 cm^{-1}–100 cm^{-1}) and high- (120 cm^{-1}–350 cm^{-1}) frequency Raman scattering. We find that three distinct crystalline phases can be formed from apparently the same glass structure ("trifurcated crystallization"). We show that precursors of these different structural transformation routes can be detectable already in the glassy state below T_g. The cause of trifurcated crystallization can be attributed to the *intrinsic* inhomogeneous distribution of nanoscopic structural units in the glass. Significant changes in high-frequency vibrational modes are mainly caused by the breaking of Ge–Ge bonds. On the other hand, significant changes in low-frequency vibrational modes are raised by the growth of domains topologically similar to the layered crystalline $GeSe_2$. Both of the spectral changes

in the low- and high- frequency ranges are almost reversible. The reversibility suggests that the nanoscopic structural units or domains play a key role on the network stability.

Finally, we investigate relaxation processes of photoexcited carriers in $GeSe_2$ glass and crystal by resonant Raman scattering and photoluminescence measurements at 15K to understand how nanoscopic structural units affect on photoinduced structural changes. We observe "excess" resonant Raman enhancement in $GeSe_2$ glass, following photodarkening (a increase of the absorption coefficient upon illumination), and its reversible change for the excitation power. We demonstrate that these two phenomena have the same origin, and discuss the mechanism from a nanoscopic point of view. We also study the relationship between local structures and electronic states of layered crystalline $GeSe_2$ which has a similar electronic structure and photoluminescence spectrum to the $GeSe_2$ glass. Combination of resonant Raman scattering with photoluminescence measurements reveals the relaxation process of the excitons localized between layers.

Chapter 1

Introduction

For crystalline materials with long range periodicity, Bragg's equation gives, in principle, a method for uniquely determining the lattice structure, and enables us to understand relationships between microscopic structures and macroscopic physical properties. On the other hand, we have still no established techniques capable of identifying the structure of disordered materials due to their lack of long range periodicity, and hence physics on glasses is far behind that on crystals.

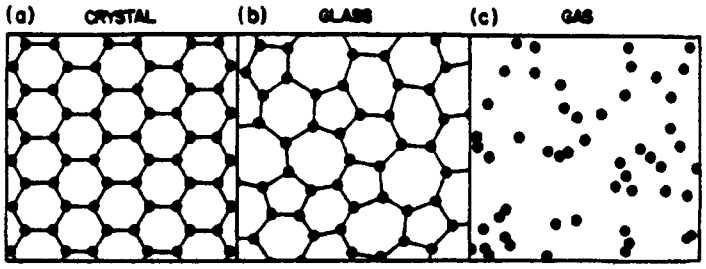

Figure 1.1: Schematic sketches of the atomic arrangements in (a) a crystalline solid, (b) an amorphous solid, and (c) a gas. From Ref. [1].

Glasses have no long range periodicity which is characteristic of crystals. It should be kept in mind that even though one breaks the long range periodicity of a crystal by displacing every atom in a random manner, the random structure is not identified with a glass. The glass structure has a difference in *topological* bonding structure from a crystalline one in addition to the randomness, as sketched in Fig. 1.1. Thus, topological concepts are important for discussing the structures of glasses.

To characterize the topological bonding structure, the concept of an *average atomic coordination number* $\langle r \rangle$ is very useful. It was first used by Phillips [2] nearly 20 years ago in the constraint counting theory that explains the strong glass-forming tendency of certain alloy compositions. The theory predicts a mechanical critical point ("rigidity transition") at $\langle r \rangle = 2.4$, where the number of constraints per atom equals the degree of freedom per atom. The mechanical property of the network undergoes a qualitative change from being easily deformable at $\langle r \rangle < 2.4$ to being rigid at $\langle r \rangle > 2.4$. At $\langle r \rangle = 2.4$, the glass-forming tendency is optimized. The idea was later refined by Thorpe and co

workers [3,4] who formulated it as a problem of rigidity percolation by introducing the number of zero-frequency "floppy" modes, which extrapolates linearly to zero when $\langle r \rangle$ increases to 2.4.

The binary Ge_xSe_{1-x} system is particularly well suited to studying the topological bonding structures due to its high covalency, small differences in the atomic sizes of Ge and Se, and its wide glass-forming region ($0 \leq x \leq 0.40$). Obeying the so called $8-N$ rule (N is the valency of an atom), the numbers of nearest neighbor atoms for Ge and Se are, respectively, 4 and 2. Then, the average coordination number $\langle r \rangle$ of Ge_xSe_{1-x} glasses is given by $\langle r \rangle = 4x+2(1-x)$. One can easily change $\langle r \rangle$ from 2.0 to 2.8 passing through the rigidity transition point $\langle r \rangle = 2.4$. Many experiments on this system have shown the relevance of the average coordination number in describing the networks [5], as we shall review later in Section 2.1.3. However, how the glassy structure varies with $\langle r \rangle$ and what variation of the structure changes its property at the rigidity transition are not still clear.

In addition to the concept of $\langle r \rangle$, there is another indispensable concept for understanding the properties of disordered materials, i.e., *inhomogeneity*. The inhomogeneity, or the existence of a variety of configurations, comes from the nature of glass. Since glass is a frozen state of liquid where numerous disordered configurations can be regarded as a manifestation of thermal fluctuation, the frozen state is in one of quasiequilibrium states having different configurations. Thus, inhomogeneity exists as an inherent property of glass, and it is an essential problem for glass science. For crystalline materials, the properties of a single crystal can be in principle uniquely determined under a combination of temperature and pressure. In contrast, for glassy materials, the properties are different from sample to sample depending on the preparation condition, the thermal history and so forth [1,6,7]. The diversity of the properties may be reduced when the preparation method is restricted to melt quenching in a fixed condition. However, looking at the structure of glasses in detail, the glass is *intrinsically* more or less inhomogeneous at least on a *nanometer* scale. It is still not clear whether the nanoscopic structural differences can lead to diversity of macroscopic properties.

The structures of Ge_xSe_{1-x} glasses can easily be transformed by heating and/or light irradiation. In other words, heating and/or light irradiation can transfer one of the quasiequilibrium glassy states into another glassy state. By light irradiation on glass at low temperature, a glassy state can be transferred to another keeping the low kinetic energy, and then the state confined by low potential barriers, which is unstable at high temperatures, can be realized.

The occurrence of photoinduced structural changes are related to inherent properties of chalcogenides, such as its low coordination, steric flexibility, and a strong localization of photoexcited carriers. The low coordination and the flexibility are related to the high

glass-forming tendency of chalcogenide alloys. The strong localization of the band tails due to lack of atomic periodicity is a general feature of amorphous semiconductors. Thus, the investigation of the mechanism of photo-induced structural changes should be instrumental in understanding the relation between the structure and properties of glass.

Our aim of this thesis is to reveal the structures corresponding to the quasiequilibrium states in Ge_xSe_{1-x} glasses, and to identify the essential structural units for the thermally- and photo-induced structural changes through the following three aspects. First, we discuss the structural changes seemingly governed by the *topological* bonding structure, described by the concept of $\langle r \rangle$. We explain the $\langle r \rangle$ dependence by the variation of *nanoscopic* structural units. Second, at a fixed composition of stoichiometric $GeSe_2$, we investigate the inhomogeneity on a nanoscopic scale, and show that the inhomogeneity leads to macroscopic structural differences. Finally, we discuss the role of the characteristic electronic structures and the flexible structural units on photoinduced structural changes.

The outline of this thesis is as follows.

Chapter 2 presents a literature review of theoretical and experimental works of rigidity transition, photoinduced structural changes, and properties of Ge–Se alloys.

Chapter 3 Compositional dependence of relaxational modes appearing around liquid–glass transition temperature is investigated by low-frequency Raman scattering. We propose the nanoscopic structural units responsible for the relaxational modes, and explain the difference in the appearance of relaxational modes between floppy ($\langle r \rangle < 2.4$) and rigid glasses ($\langle r \rangle > 2.4$). In addition, we discuss the compositional dependence in connection with the recently developed concept "self-organization" which is not only an indispensable supplement of random network model, but has also been applied to many phenomena in areas of condensed matter science [8–10].

Chapter 4 gives high-frequency Raman scattering results on structural changes upon heating towards crystallization temperature in the stoichiometric $GeSe_2$ glass. We find that three distinct crystalline phases can be formed from apparently the same glass structure ("trifurcated crystallization"). We show that precursors of these different structural transformation routes can be observed already in the glassy state below T_g. We discuss the origin of the trifurcated crystallization in terms of the *intrinsic* inhomogeneous distribution of nanoscopic structural units in the glass.

Chapter 5 provides low-frequency Raman scattering results on structural changes on a medium range scale in $GeSe_2$ glass upon heating toward crystallization. We study the correlation between the low-frequency dynamics and the crystallization rate, and explain the correlation based on the nanoscopic inhomogeneity of structural domains similar to layered crystalline $GeSe_2$. We extend the obtained structural view for $GeSe_2$

glass to other rigid glasses in order to complete the discussion in Chap. 3.

Chapter 6 Compositional variation of local structures responsible for the band-tail electronic states is investigated by resonant Raman scattering at RT. Because, in Ge–Se glasses, the electronic states in the band-tail region are localized; we can investigate local structures around which the resonant electronic states are localized. Based on the investigation, we proceed to draw the picture proposed in Chap. 3, and show what happens around the rigidity transition composition.

Chapter 7 In this and subsequent chapters, we study photoexcited electronic states toward understanding of photoinduced changes characteristic of chalcogenide glasses. Resonant Raman studies of photoinduced structural changes are given. We observe *excess* resonant enhancement at 15 K, induced by the structural change causing photodarkening (an increase of the absorption coefficient upon illumination). In addition, we find a reversible change in the excess resonant enhancement for the excitation power, and discuss the mechanism from a nanostructural point of view.

Chapter 8 Localized exciton and its interaction with lattice vibrations in layered crystalline $GeSe_2$ are studied by resonant Raman scattering. Since we have shown in Chap. 5 that $GeSe_2$ glass involves a cluster topologically similar to the layered crystal, the information on the electronic structure and the electron-phonon interaction in the crystal helps to understand the photoinduced structural changes in the glasses. We demonstrate that the localized exciton is located around a particular pair of Se atoms which form a π-type *interlayer* interaction.

Chapter 9 presents the results of time-resolved photoluminescence (PL) measurement on the layered crystal. Due to its strong electron-phonon interaction the PL spectrum exhibits a large Stokes-shift; the PL follows a relaxation of photoexcited states. We investigate decay profiles of two PL bands that are the final states of the relaxation. The localized exciton discussed in Chap. 8 is one of the initial states of the relaxation. Thus, combining these two experimental results, we propose the relaxation process of the localized exciton and the radiative structure.

Chapter 10 is devoted to a summary of this thesis.

Appendices review theories of Raman scattering. Appendix A deals with a conventional theory of Raman scattering from crystals and disordered materials. Appendix B outlines the method which we use to analyze the low-frequency vibrations.

Chapter 2

Historical backgrounds

In this thesis, toward drawing a structural picture of disordered networks, we investigate the compositional dependences of vibrational and electronic properties in Ge_xSe_{1-x} glasses, especially focusing on changes at the rigidity transition. The constraint counting procedure which predicts the rigidity transition and experimental evidences of the rigidity transition in Ge_xSe_{1-x} glasses will be shown in Sec. 2.1. We also investigate electronic structure and its interaction with lattice vibrations in Ge_xSe_{1-x} glasses for understanding the photo-induced structural changes which are characteristic features of chalcogenide glasses. We shall survey experimental studies and proposed models for the photoinduced changes in Sec. 2.2. We shall review in Sec. 2.3 the structures and properties of Ge_xSe_{1-x} glasses and crystalline $GeSe_2$.

2.1 Rigidity transition in network glasses

2.1.1 Description of network glass

Generally, "glass" is defined as a condensed state of matter which has become frozen by the continuous slow-down of its degrees of freedom fluctuating at a rate. The point at which the fluctuations become frozen is called "glass transition". This definition is satisfied by not only conventional glasses such as silica glass and chalcogenide glasses, but also spin glasses, orientational glasses, and vortex glasses. Usually a conventional glass is identified as an amorphous solid capable of passing continuously into the viscous liquid state accompanying by an abrupt increase in heat capacity. In this thesis, we use the term of "glass" to refer to the conventional glass.

In glasses, we can change *continuously* the elemental ratios. Especially, in covalent glasses, one can change continuously the network topology. This enables compositional studies which seem to be vitally important for studying the glassy structure. The study of the structure of network glasses has progressed since the pioneering work of Zachariasen [11] in 1932, which has introduced the idea of the continuous random network (CRN). He has proposed that "...the atomic arrangement in glass is characterized by an extended three dimensional network which lacks symmetry and periodicity." Such a network is shown in Fig. 2.1. The CRN model describes properties of network glasses fairly well [12]. However, Raman and Mössbauer spectroscopic results [5,13,14] have shown that some fractions of homopolar bonds (Ge–Ge, Se–Se, or S–S) and very stable

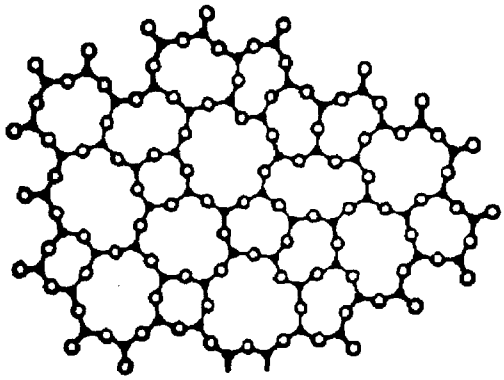

Figure 2.1: Zachariasen's random network diagram. Small black dots denote threefold coordinated atoms such as Al and As, and large open circles denote twofold coordinated atoms such as O, S, and Se. From Ref. [11].

building blocks composed of $Ge(Se,S)_{4/2}$ tetrahedra appear to be an intrinsic feature of the completely relaxed stoichiometric $GeSe_2$ and GeS_2 bulk glasses. The presence of a finite and reproducible broken chemical order and clustering should be strongly influenced by packing constraints. Essential network properties including the broken chemical order and clustering have been well understood in terms of topological principles using the idea of force field constraints [9,14–16].

2.1.2 Algorithm for counting constraints

In this thesis, we describe the networks of Ge_xSe_{1-x} glasses which have a negligible number of dangling bonds except for a transient state of photo-induced structural changes (for details, see, Sec. 2.2). If the total number of atoms is N and there are n_r atoms with coordination r ($r = 2$ or 4), then

$$N = \sum_r n_r. \tag{2.1}$$

We can define the average coordination $\langle r \rangle$ by

$$\langle r \rangle = \frac{\sum_r r n_r}{\sum_r n_r} = 2 + 2x. \tag{2.2}$$

We note that $\langle r \rangle$ gives a partial, but very useful, mean-field description of network properties.

The constraint counting proceeds as follows. There is a single constraint associated with each bond, and one can assign as $r/2$ constraints for each r-coordinated atom. In

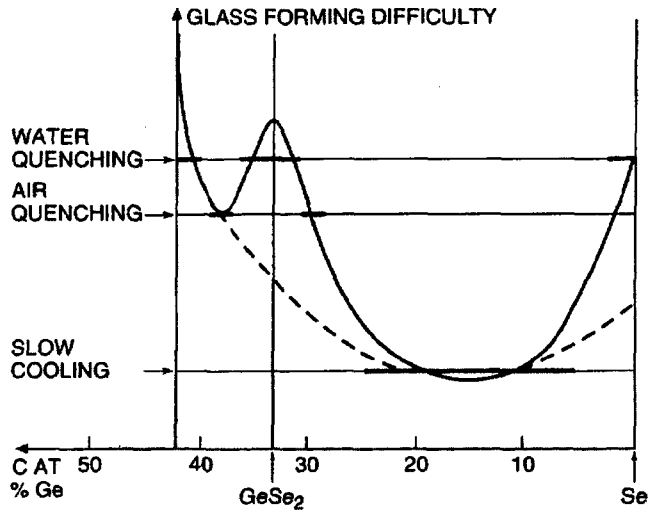

Figure 2.2: The glass-forming difficulty (solid line) in Ge_xSe_{1-x} glasses [17]. A broken curve represents the difficulty if the effects of compound stoichiometries (see, Fig. 2.19) are omitted. From Ref. [2].

addition, there are constraints associated with the angular forces; there are a total of $2r-3$ angular constraints. Thus, the total number of constraints, n_c, is

$$n_c = \sum_r n_r[r/2 + (2r-3)]. \tag{2.3}$$

Phillips has predicted that when n_c equals the number of degrees of freedom, $n_d = 3N$, a network is mechanically optimized. And then, upon quenching a melt of this critical composition, glass formation instead of crystallization. This condition is satisfied at $\langle r \rangle = 2.4$, according to Eq. 2.3. Indeed, a high glassy-forming tendency at the point is observed in a variety of chalcogenides such as As_2(S or Se)$_3$ and Ge(S or Se)$_4$ glasses. The minimum of the glass forming difficulty (or the maximum of glass-forming tendency) at the composition in Ge–Se glasses is displayed in Fig. 2.2.

Through a normal mode analysis, Thorpe has recognized that the fraction, f, of zero-frequency ("floppy") modes is given by

$$f = (n_d - n_c)/3N \tag{2.4}$$

$$= [3N - \sum_{r=2}^{4} n_r[r/2 + (2r-3)]]/3N \tag{2.5}$$

$$= 2 - \frac{5}{6}\langle r \rangle. \tag{2.6}$$

As $\langle r \rangle$ increases, the floppy modes are quenched out and vanish around the critical coordination for glass-formation $\langle r \rangle = 2.4$. In other words, the network becomes rigid

above the critical coordination. Underconstrained networks ($\langle r \rangle < 2.4$, $n_c < 3N$) are easily deformable while overconstrained ones ($\langle r \rangle > 2.4$, $n_c > 3N$), are intrinsically rigid. Thus, the condition for the glass-forming tendency to be optimized coincides with the onset of rigidity. For this reason, the nature of the rigidity transition in network glasses has attracted particular attention in glass science.

2.1.3 Experimental evidences

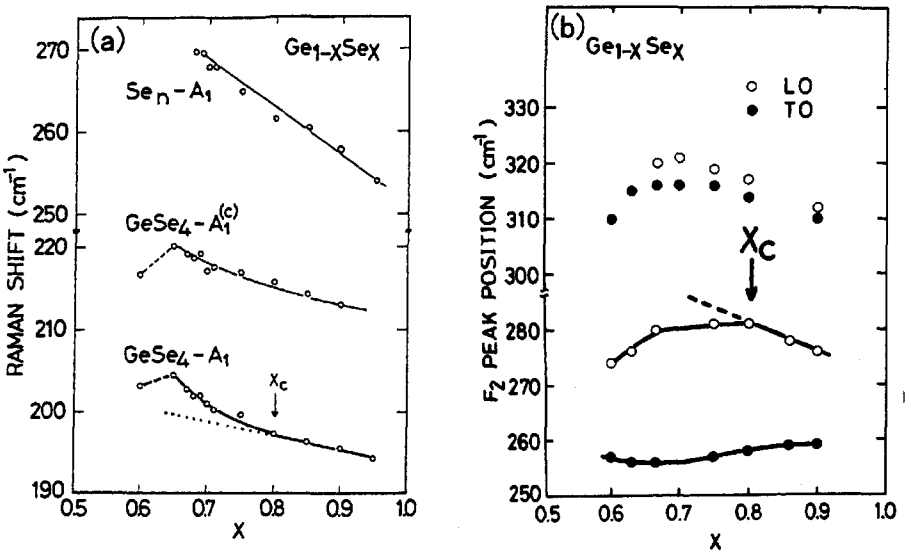

Figure 2.3: Composition dependence of (a) Raman spectra and (b) IR spectra in $Ge_{1-x}Se_x$ glasses. From Ref. [18].

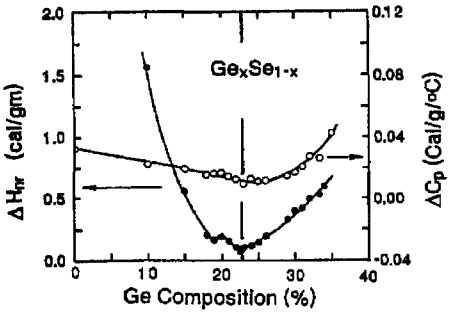

Figure 2.4: Compositional dependences of nonreversing heat flow $\Delta H_{nr}(T_g)$ (filled circles) and specific heat ΔC_p (open circles) from modulated differential scanning calorimetry (MDSC) measurements in Ge_xSe_{100-x} glasses. From Ref. [9].

We give in Table 2.1 an overview of principal experimental studies demonstrating a transition of various properties around $\langle r \rangle = 2.4$ in chalcogenide glasses. Broadly

Table 2.1: Experimental works of rigidity transition.

Method	Result	Author & Ref
Raman scattering and IR absorption	Mode frequency shows a kink at $\langle r \rangle = 2.46$	Murase *et al.* (1983) [13,18] (Fig. Feng *et al.* (1996) [19] Boolchand *et al.* (1999) [9]
Modulated DSC	Nonreversing heat flow $\Delta H_{nr}(T_g)$ shows minimum around $\langle r \rangle = 2.40$	Feng *et al.* (1996) [19] (Fig. 2.4) Boolchand *et al.* (1999) [9]
Thermodynamical measurements	Activation energy for viscosity, excess heat capacity shows minimum around $\langle r \rangle = 2.40$	Tatsumisago *et al.* (1990) [20] (Fig. 2.5) Senapati *et al.* (1995) [21]
Density-Archimedes Method	Molar volume shows minimum around $\langle r \rangle = 2.40$	Feltz *et al.* (1983) [22] (Fig. 2.6)
Inelastic neutron scattering	Low-frequency mode ($\sim$5 meV) shows mild kink at $\langle r \rangle = 2.40$	Kamitakahara *et al.* (1991) [23] (Fig. 2.7)
Resistivity measurement at high pressure	Metal-insulator transition pressure shows kink at $\langle r \rangle = 2.40$	Asokan *et al.* (1988) [24] (Fig. 2.8)
^{129}I Mössbauer spectroscopy	Site intensity ratio displays a local maximum at $\langle r \rangle = 2.46$	Bresser *et al.* (1986) [25] (Fig. 2.9)
Normal and inverse photoemission spectroscopies	Electronic structures of valence and conduction bands change abruptly at $\langle r \rangle = 2.40$	Taniguchi *et al.* (1996) [26] (Fig. 2.10)
High temperature Raman scattering	Crystallization occurs around and above $\langle r \rangle = 2.40$ in an experimental time period	Wang *et al.* (1998) [27] (Fig. 2.11)
Low-frequency Raman scattering	Disappearance of bending fracton above $\langle r \rangle = 2.40$	Nakamura *et al.* (1998) [28] (Fig. 2.12)

speaking, the rigidity transitions are shown by two types of experiments. One is the study on glassy melts at $T \gtrsim T_g$ where thermal properties change remarkably with temperature and glass composition. The second one is the study on glassy solids at $T \ll T_g$ where electronic and vibrational properties show the onset of rigidity. In this thesis, we shall treat both types of rigidity transition.

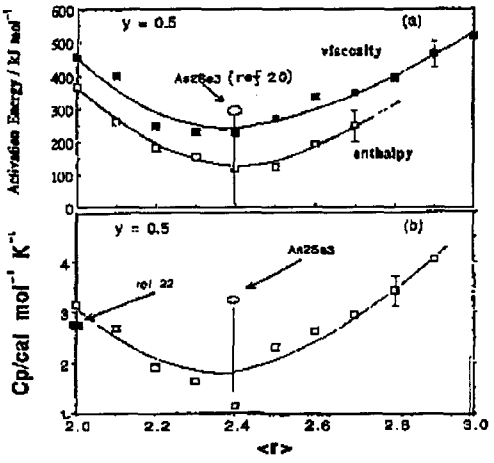

Figure 2.5: (a) $\langle r \rangle$ dependence of activation energies for viscosity and enthalpy relaxation. (b) Dependence of excess heat capacity at T_g. From Ref. [20].

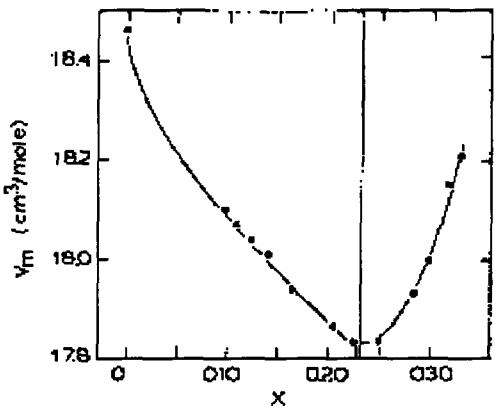

Figure 2.6: Molar volumes of Ge_xSe_{1-x} glasses as a function of x. From Ref. [22].

Difference between floppy and rigid glasses

Figure 2.13 shows T_g for Ge–As–Se glasses along various pseudobinary cuts. Below the rigidity transition threshold ($\langle r \rangle \lesssim 2.4$), T_g is a universal function of $\langle r \rangle$. In other words, T_g is determined only by the network connectivity, independent of the species of atoms (Ge or As) in floppy glasses. However, above $\langle r \rangle \sim 2.5$, T_g depends on the species of atoms even at the same $\langle r \rangle$, reflecting the individuality of the atoms. It has been believed that the diversity is a signature of the formation of Ge–Se and/or As–Se clusters in rigid glasses.

The clustering in rigid glasses has also been suggested by the investigation of the glass forming tendency of $(Ge_{1-y}Sn_y)_xSe_{1-x}$, depicted in Fig. 2.14. The glass phase boundary shows a critical behavior near at $x_c = 0.20$. When the Ge composition x is smaller than 0.2, the glass forming Sn composition range is wide ($0 \leq y \lesssim 0.9$). Above the critical Ge composition x_c, the boundary Sn composition y_b decreases with x. The glass forming Sn composition range is very narrow in around the stoichiometric composition $x = 0.33$. This tendency of the exclusion of Sn atoms from the glass at $x \gtrsim 0.20$ has been explained on the basis of the existence of strongly bonded region composed

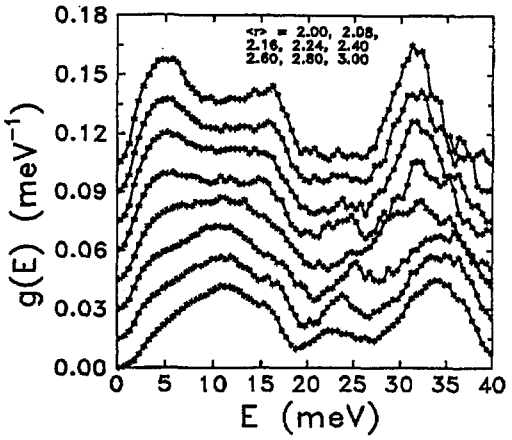

Figure 2.7: Vibrational density of states measured by inelastic neutron scattering. The top curve is for pure Se glass ($\langle r \rangle$=2.0). The other glasses in order correspond to $\langle r \rangle$ = 2.08, 2.16, 2.24, 2.40, 2.60, 2.80, and 3.00. From Ref. [23].

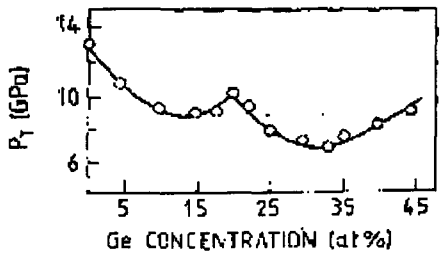

Figure 2.8: Composition dependence of glassy semiconductor-metal-transition pressure of Ge_xSe_{1-x} glasses. From Ref. [24].

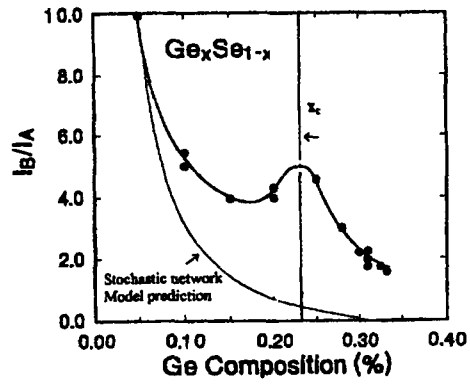

Figure 2.9: Mössbauer site-intensity ratio I_A/I_B as a function of x in $Ge_x(Se_{0.99}Te_{0.01})_{1-x}$ glasses. A and B correspond to different local configurations around Se sites. From Ref. [25].

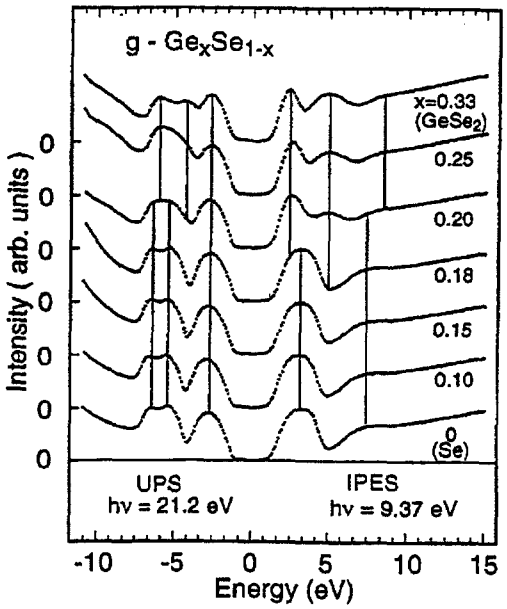

Figure 2.10: Valence-band UPS (ultraviolet photoemission spectroscopy) and conduction-band IPES (inverse photoemission spectroscopy) of Ge_xSe_{1-x} glasses. Vertical bars indicate the positions of structures. Energies are referred to the Fermi level. From Ref. [26].

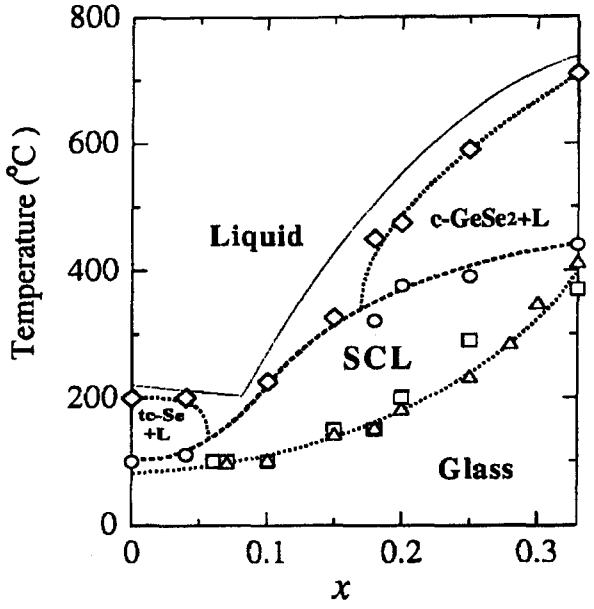

Figure 2.11: The value of T_g (squares), T_c (circles), and T_m (diamonds) determined by using Raman scattering. The value of T_g from DSC measurement (triangle) is also shown. From Ref. [27].

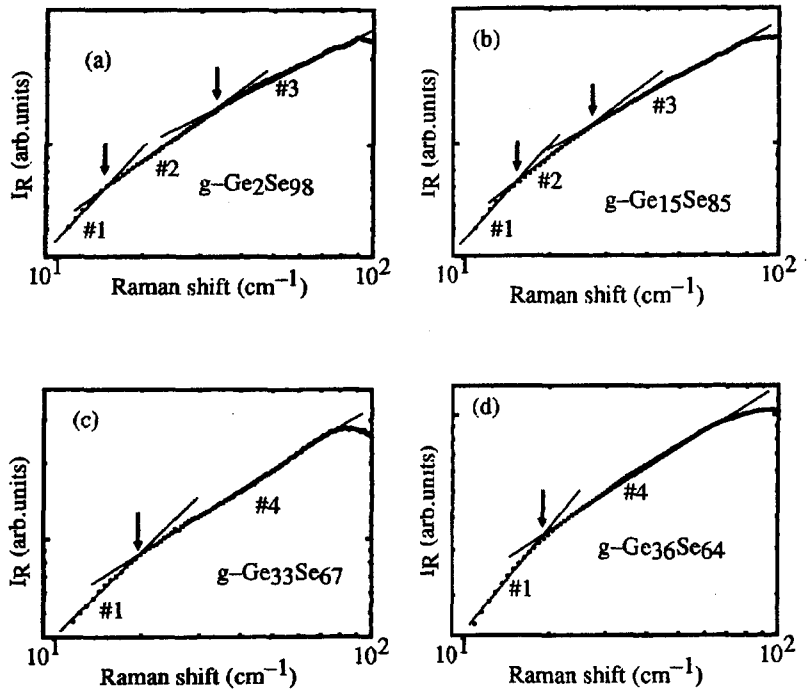

Figure 2.12: The log-log plots of reduced Raman spectra $I_R(\omega) = I/[n(\omega) + 1]$ of Ge_xSe_{1-x} glasses in the low-frequency region. The data of #1 correspond to Debye behavior. The data of #2 are due to bending-fractons, and those of #3 and #4 are due to stretching fractons. From Ref. [28].

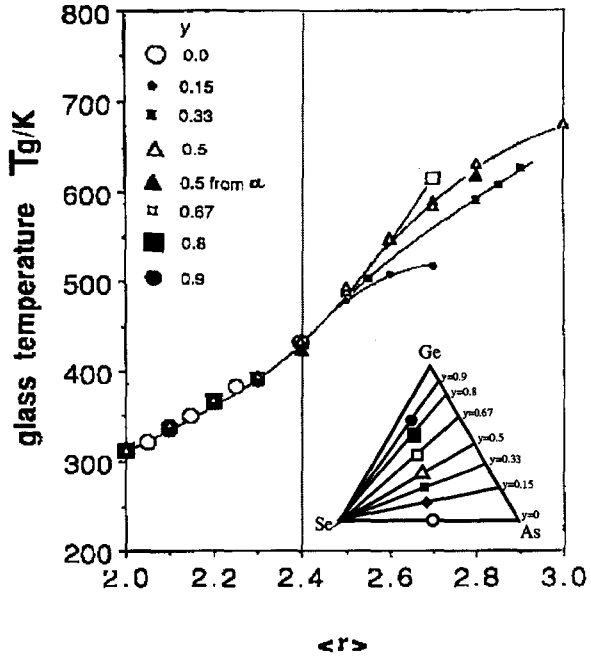

Figure 2.13: $\langle r \rangle$ dependence of T_g from DSC and thermal-expansivity measurements for Ge–As–Se glasses along various pseudobinary cuts $(Ge_yAs_{1-y})Se_{1-x}$ as indicated in the inset.

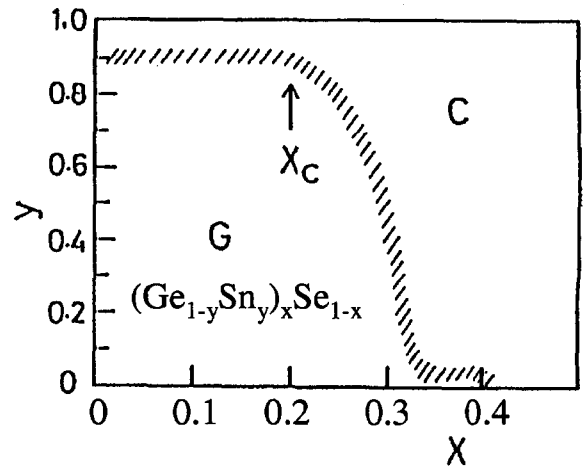

Figure 2.14: Glass forming region of $(Ge_{1-y}Sn_y)_xSe_{1-x}$ when prepared by melt-quenching method. G: glass forming region, C: crystallization is seen in this region by X-ray analysis.

of Ge and Se atoms, i.e., Ge–Se cluster. It has been speculated that incorporation of the Sn atoms into the Ge–Se clusters is unfavorable due to its large ionic radius and ionicity.

2.1.4 Self-organization

So far in this chapter, we have dealt with models of random networks. However, realistic glassy networks will have some nonrandom features. Even though bulk glasses are formed at high temperatures where entropic effects are dominant, it is clearly not correct to completely ignore energy considerations; the glasses can favor particular local structural arrangements. A simple example is local chemical ordering where bonding between certain same-type atoms is unfavorable. This chemical effect is, for example,

seen in glass-forming tendency shown in Fig. 2.2. Another nonrandom example is partial topological ordering in order to minimize the free energy. This subtle structural correlation is referred to as "self-organization".

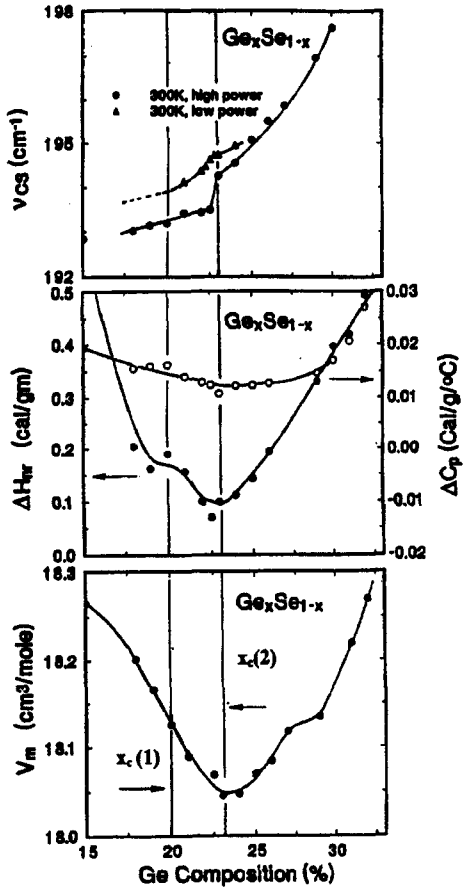

Figure 2.15: Ge concentration dependence of CST mode frequency ν_{CS}, nonreversing heat flow ΔH_{nr}, and Molar volume V_M in Ge_xSe_{1-x} glasses. The composition $x_c(1)$ and $x_c(2)$ represent the onset and completion of rigidity in the glasses. From Ref. [9].

Very recently, this effect for rigidity transition has been manifested by Boolchand *et al.* [9]. They have suggested that the rigidity transition is richer in nature than that predicted by the previous mean-field constraint theory, on the basis of the results of Raman scattering, Mössbauer spectroscopy, modulated differential scanning calorimetry (MDSC), and molar volumes, as shown in Fig. 2.15. They have proposed the existence of an intermediate phase which starts near $\langle r_{(1)} \rangle = 2.40$ and is completed near $\langle r_{(2)} \rangle = 2.46$ ($x = 0.23$).

Thorpe *et al.* have proposed, based on numerical simulations [29], that the glasses in the intermediate phase are "self-organized" at some level, and not random networks. The basic idea for the construction of the self-organized network is as follows. The construction is stated with a smaller coordinated floppy network and bonds are added to the network. This addition leads to formation of rigid regions. When each bond length (angle) can have its natural length (angle) without being forced to change by the surrounding environment, we call the bond "unstressed", and otherwise "stressed". As long as the added bonds are unstressed, they are retained. If adding a bond would

result in a creation of a stressed (overconstrained) region, then that move is abandoned. Results of the simulations are shown in Figs. 2.16 and 2.17. Figure 2.16 shows the existence of the intermediate phase where rigidity percolates while stress does not; the percolating rigid and stressed fractions turn zero at different points (isostatic transition at $\langle r \rangle = 2.376$ and stress transition at $\langle r \rangle = 2.392$), between which the intermediate phase exists. Figure 2.17 shows the comparison of numbers of floppy modes in random (conventional) and self-organized networks. Since there are no stressed region in the network below the stress transition, the number of floppy modes follows mean field counting (Eq. 2.6) exactly (which means it is perfectly linear in $\langle r \rangle$). This linearity means that the isostatic transition is not seen in the number of floppy modes and is second order while the stress transition is accompanied with the change of the slope, as is expected for the first order transition [29]. As another effect of self-organization on network, there is an inhibition of formation of small rings. It has been shown that removing the small rings cause the mechanical threshold to change from a second order to a first order transition; the transition is sharpened.

2.2 Photo-induced structural changes

Chalcogenide glasses exhibit various kinds of photoinduced structural changes as listed in Table 2.2. Since the pioneering work of Ovshinsky *et al.* [31–33] who have found that the steric flexibility of chalcogenides permits reversible alternations of the local

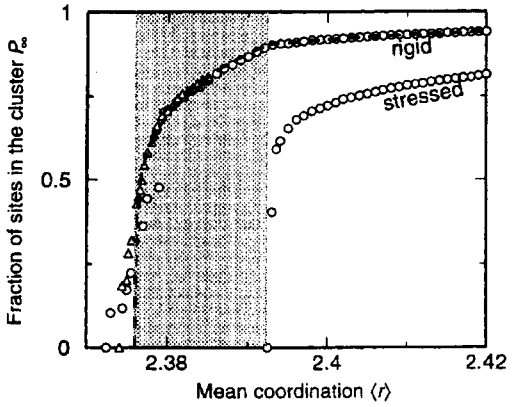

Figure 2.16: The fractions of bonds (P_∞) in percolating rigid and stressed clusters. The intermediate phase is shaded, where rigid percolating clusters exist while the stressed ones scarcely exist. From Ref. [30].

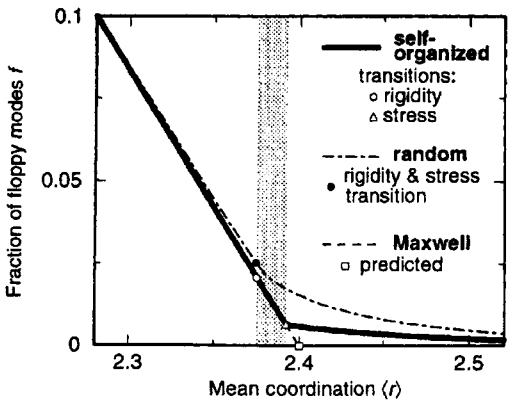

Figure 2.17: The fractions of floppy modes per degrees of freedom for a 3D network in self-organized and random cases. From Ref. [30].

structures and the opto-electronic properties, photoinduced structural changes have attracted many researchers in theoretical and technological aspects; these phenomena are expected for the production of optical storage materials, electronic switching and memory devices.

In chalcogenide semiconductors, generally, the lone-pair p orbitals of chalcogens form the highest filled band, which is the valence band [34]. The unfilled conduction band consists of antibonding orbitals of the covalent bonds. The lone pair electrons are localized in the band tail of the valence band and are easily excited, usually by light exposure using a photon energy close to the band gap. According to Street [35], the exciton generated by photoexcitation can be either self-trapped with a strong distortion of lattice in a localized state, which has higher energy than the ground state, or can recombine back to the ground state. He has argued that the energy level of the trap should be considerably lower in comparison with that of the exciton so that the energy barrier from the exciton level to the trap is small. The filled trapped state is the cause of the redshift. Larger redshift in chalcogenides is due to the strengthening of the localized state by the creation of a kind of defect in the atomic bonding configuration, such as the so called valence alternation pairs (VAP) described by Kastner, Adler, and Fritzsche [36]. This VAP has been widely accepted as a possible mechanism for photodarkening. The basic assumptions for this are that the atomic bonding configuration can be altered due to illumination, resulting in, locally, an overcoordinated center with a positive charge (D^+ or C_3^+) and an undercoordinated center with a negative charge (D^- or C_1^-). The energy of the resulting D^+, D^- pair is slightly higher than the ground state. Thermal annealing can relax the light induced defect and can excite the trapped exciton back to the ground state.

Table 2.2: Typical photo-induced phenomena of chalcogenide glasses. They are usually classified into reversible change and irreversible one by annealing just below T_g [37,38].

Term	Phenomenon	Reversibility for annealing
Photo-darkening	Red shift of band gap energy	Reversible
Photoinduced-anisotropy	Dichroism by polarized light	Reversible
Photoinduced-fluidity	Decrease of viscosity	Reversible
Photo-expansion	Volume change	Mainly reversible
Photo-bleaching	Blue shift of band gap energy	Mainly irreversible
Photo-doping	Diffusion of metals into chalcogenides	Irreversible
Photoinduced-crystallization	Crystallization	Irreversible
Photo-decomposition	Phase-separation	Irreversible

Although numerous efforts have been devoted to the investigation of photo-induced structural change, the microscopic mechanism of photo-induced structural change is

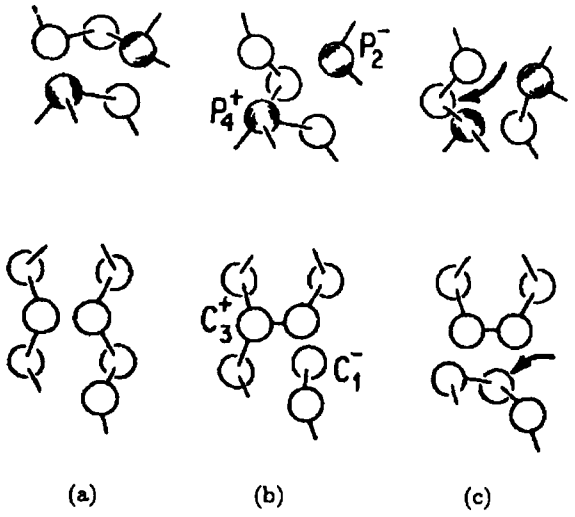

Figure 2.18: Examples of elementary steps of photostructural changes. White balls are chalcogens (C) and shaded balls are pnictide atoms (P). (a) Initial bonding configuration, (b) transient self-trapped exciton after photon excitation, (c) one of several new bonding configurations after recombination with motion of atom indicated by arrow. From Ref. [39].

still controversial. We show here a microscopic picture for creation of metastable defects (VAP), which results in bond-switching. It has been believed that bond-switching is one of elemental steps of various structural changes. The self-traping of photoexcited carriers induces a bonding change, as illustrated in Fig. 2.18(b). This state is transient and non-radiative recombination occurs with dissipation of the rather large recombination energy via a local deformation associated with its formation and subsequent annihilation. While many of the recombination processes will restore the original bonding configuration of Fig. 2.18(a), this does not necessarily occur and conversion to other configurations is possible. Two of those configurations are shown in Fig. 2.18(c). Thus, further structural changes are induced. The number of homopolar and heteropolar bonds may also change in these processes as demonstrated by Raman scattering [40] and XAFS [41].

2.3 Review of researches on germanium selenide alloys

2.3.1 Ge–Se glasses

Phase diagram of Ge–Se system

The phase diagram of Ge_xSe_{1-x} system is given in Fig. 2.19. In the composition range of $0 \leq x \leq 0.08$, the liquidus temperature (T_m) is nearly constant at about 220°C. With increasing x, T_m increases in a monotonic way up to $x = 0.33$, and then, T_m starts to decrease. When the melts ($0 \leq x \leq 0.40$) above such a liquidus line are quenched into iced water, Ge_xSe_{1-x} glasses can be obtained (for experimental conditions of our sample preparation, see, Sec. 3.2).

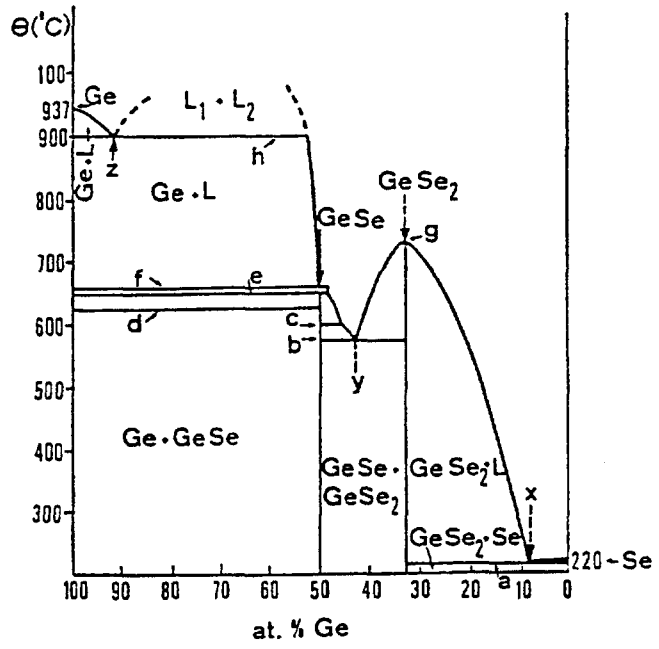

Figure 2.19: Phase diagram of Ge–Se system summarized in Ref. [12]. ***a*∼*h*** denote temperatures, and ***X*∼*Z*** denote the compositions, as follows.
a: 218°C *1;
b: 580°C *2, 578°C *3, 573°C *4;
c: 630°C *2, 603°C *4;
d: 623°C *2;
e: 660°C *3, 651°C *4;
f: 666°C *3, 661°C *4;
g: 740°C *2, *3, *4;
h: 900°C *3, 890°C *4;
X: at.% Ge = 8 *1;
Y: at.% Ge = 38 *2, 40∼42 *3, 43 *4;
Z: at.% Ge = 88∼89 *3, 86 *4
(*1: Dembovskii *et al.* [42], *2: Vinogradova *et al.* [43], *3: Ross *et al.* [44], and *4: Quenez *et al.* [45]).

Structural units on short and medium range scales

The short range order of Ge_xSe_{1-x} glasses has been studied using x-ray diffraction measurements [46], infrared and Raman spectroscopies [12,47], and Mössbauer spectroscopy [48]. The short range order is dominated by $GeSe_{4/2}$ tetrahedral units, ethan-like Ge–Ge units and Se chains.

The medium range order (MRO) is current interest in relation to its physical properties. One manifestation of MRO is the first sharp diffraction peak (FSDP) observed in the structural factor, $S(Q)$. The FSDP is believed to be a signature of the medium range correlation extending beyond the nearest neighbor distances. In $GeSe_2$ glass, the FSDP is observed at 1.0 $Å^{-1}$ as shown in Fig. 2.20.

Phillips [50] has proposed a raft model to describe the atomistic scale structure of $GeSe_2$ glass. In his model the interlayer correlations, similar to those in the crystalline $GeSe_2$, are responsible for the FSDP. However, the x-ray diffraction measurement [51] on thin $GeSe_2$ films could not give direct evidence for such low dimensional correlations. A molecular dynamics (MD) study of molten and glassy $GeSe_2$ by Vashishta *et al.* [52] has shed light on the structural and dynamical properties of chalcogenide glasses. The MD results manifest the formation of a network structure composed of $GeSe_{4/2}$ tetrahedra. However, the medium range structure has not been fully specified. Thus, despite of

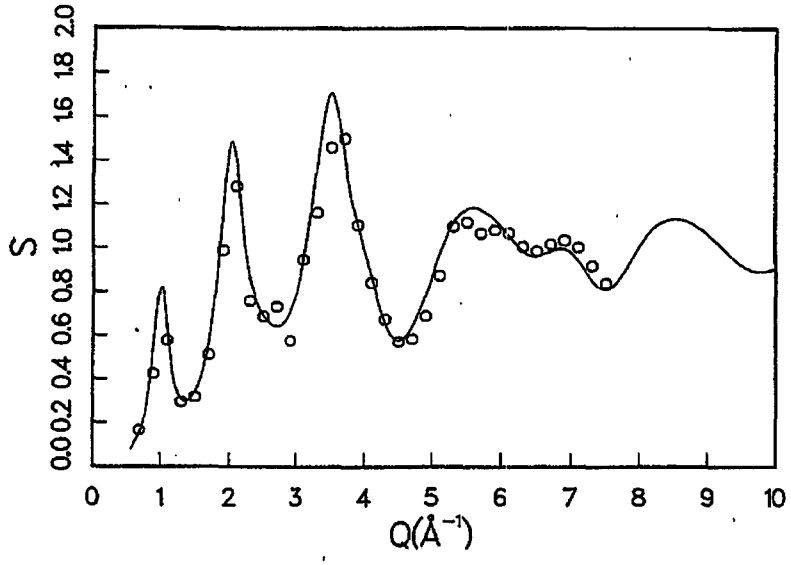

Figure 2.20: S(Q) of $GeSe_2$ glass derived from integration of S(Q,E) from inelastic neutron scattering (open circles) with that measured in a diffraction experiment (solid line) [49].

numerous studies for FSDP, the origin remains controversial.

Vibrational properties

Raman spectroscopy has been an important tool for investigating the vibrational properties of chalcogenide glasses for over two decades [5,13,54]. Fig. 2.21 shows the Raman spectra of Ge_xSe_{1-x} glasses ($0 \leq x \leq 0.33$) investigated by Murase *et al.* [18]. In the Raman spectra of pure glassy Se ($x = 0$), a strong Raman band is observed around 250 cm^{-1}, and the intensity decreases with increasing Ge content x. This band has been ascribed to the stretching mode of Se–Se bonds. In all the Raman spectra of Ge_xSe_{1-x} except for $x = 0$, a Raman band (A_1) is observed around 200 cm^{-1}, which grows up with increasing x. The A_1 band has been ascribed to the symmetric breathing mode (A_1 mode according to the notation of group theory) of the corner-sharing $GeSe_{4/2}$ tetrahedra (CST). The F_2 mode of $GeSe_{4/2}$ tetrahedra is expected to be observed around 250-330 cm^{-1} [55–57]. At $x = 0.33$, the A_G band is observed on the low-frequency side of A_1 band, which has been interpreted as the stretching mode of Ge–Ge bonds [55–57].

On the high-frequency side of A_1 band, a companion band (A_1^C) is observed above $x \gtrsim 0.15$, and the intensity rapidly increases as x approaches 1/3. Historically, the origin of this band has attracted attention of many researchers in relation to the MRO, and had been controversial. Matsuda *et al.* [58] have investigated resonant Raman scattering of

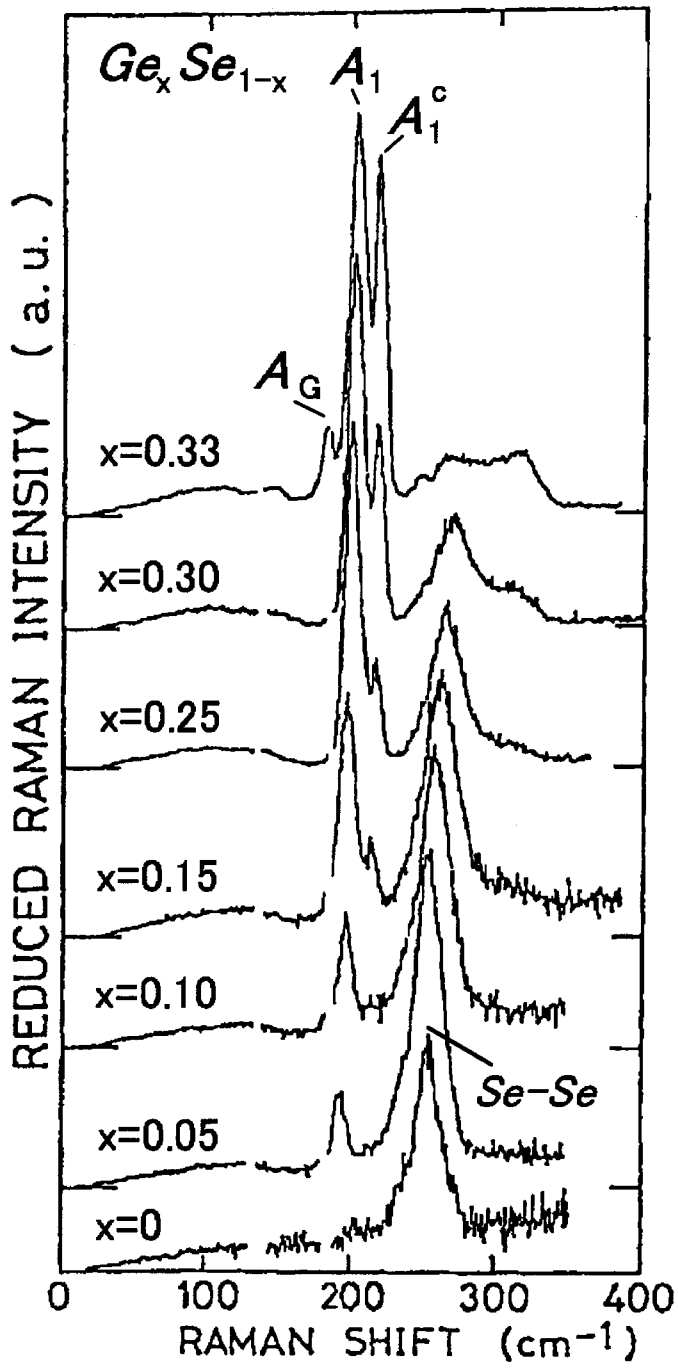

Figure 2.21: Reduced Raman spectra of Ge_xSe_{1-x} glasses at 50K. Excitation photon energy is 1.96 eV. The reduced intensity is given by $I(\omega,T)/(n(\omega,T)+1)$, where n($\omega$,T) is Bose population factor. From Ref. [18].

crystalline $GeSe_2$ and have found that the energy position of a resonant mode, A^* is very close to that of the A_1^C band of $GeSe_2$ glass. Inoue *et al.* [59–61] have calculated

the vibrational modes, based on valence force field model (VFF), and have assigned the A^* Raman band to the in-phase breathing vibrations quasi-localized at the edge sharing $GeSe_{4/2}$ tetrahedra (EST) [60]. Thus, the A_1^C band has been ascribed to the breathing mode of EST.

These assignments for the Raman bands have been supported by recent theoretical calculations. Jackson *et al.* [62] have calculated directly from first principles vibrational modes for three cluster building blocks of the glasses, CST, EST and ethan-like Ge–Ge units; and have succeeded in reproducing the experimental measured Raman spectra. Cobb *et al.* [63] have made *ab initio* molecular dynamics (MD) study using a 216 atom model. In their model, the A_1 band is dominated by tetrahedral breathinglike motions. They have also confirmed that Ge–Ge stretching modes contribute significantly to the A_G band. Their calculated vibrational density of states (VDOS) in the 230 cm^{-1}–330 cm^{-1} energy region comes from F_2-type motions of $GeSe_{4/2}$ tetrahedra. Se atoms with homopolar bonds also contribute significantly to the modes in the energy region.

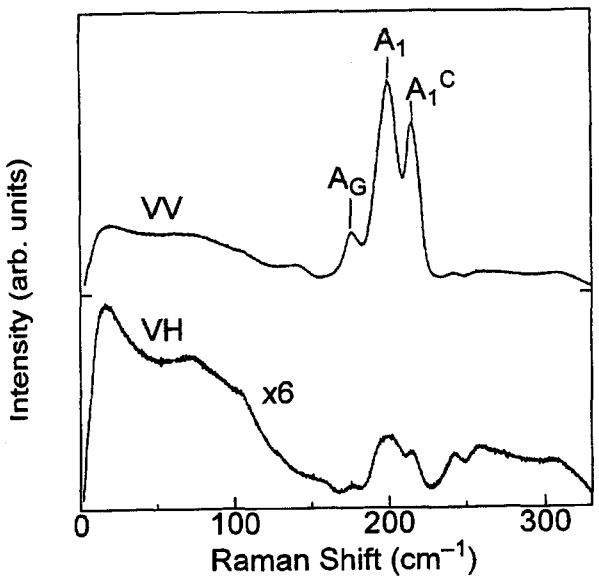

Figure 2.22: Raman spectra of $GeSe_2$ glass at room temperature. The spectra are taken in VV and VH polarization configurations with a 1.72 eV excitation energy.

In recent years, a particular effort has also been directed towards the frequency range from 5 cm^{-1} to 100 cm^{-1} which is expected to reflect the cooperative motions of atoms over correlation lengths in the nanometer range [28]. In this low-frequency range, the Raman spectrum of most glasses is dominated by a strong broad line usually called the boson peak (BP). This peak is observed around 20 cm^{-1} in $GeSe_2$ glass, as shown in Fig. 2.22. The appearance of the BP is a universal property in glassy materials while

it is not observed in single crystals. Then, the nature of this peak is considered to be determined by the general peculiarities of the glass structure, but the origin is still a matter of debate.

Electronic structure

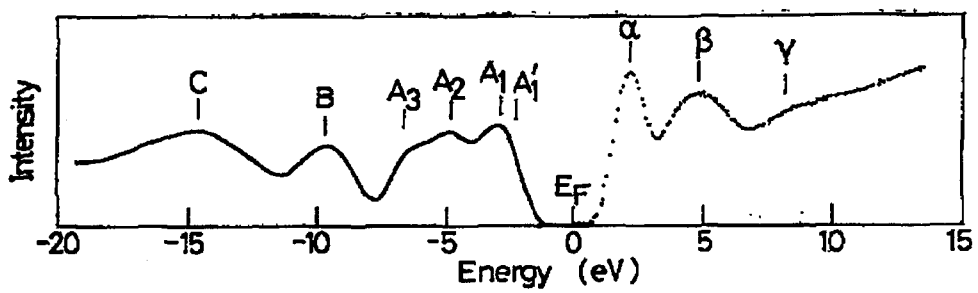

Figure 2.23: Photoemission (solid line) and inverse-photoemission (dotted line) spectra of amorphous $GeSe_2$. Energies are referred to the Fermi level. From Ref. [64].

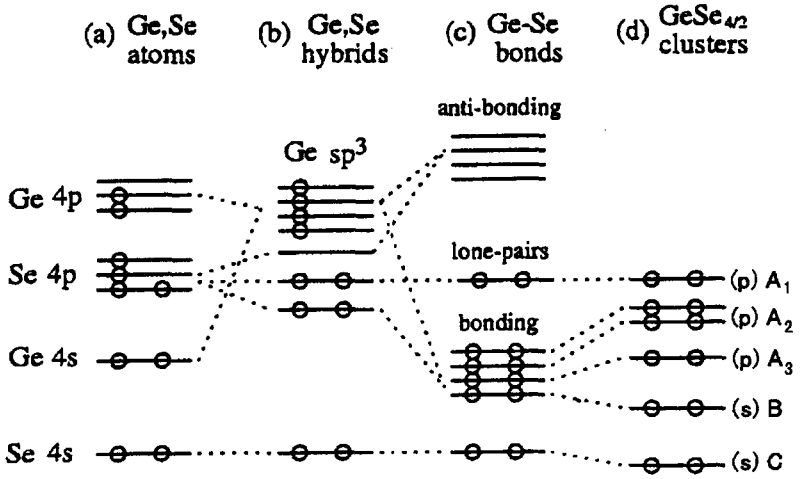

Figure 2.24: Schematic energy diagram for $GeSe_2$ alloy. (a) Energy level of valence electrons for separated Ge and Se atoms. (b) Three Ge $4p$ and one Ge $4s$ orbitals hybridized to a Ge sp^3 orbital. (c) A Ge sp^3 hybrid and one Se $4p$ orbitals make Ge-Se bonding and anti-bonding states. There remains two Se $4p$ orbitals as lone-pair electrons. (d) Clustering of $GeSe_{4/2}$ tetrahedra resolves the degeneracy of four Ge-Se bonding orbitals.

The valence and core electronic states has well been characterized by photoelectron and photoemission spectroscopies [64–66]. Figure 2.24 shows a schematic energy diagram for the valence and the conduction bands of $GeSe_2$. The six valence bands $(A_1, A_1', A_2, A_3, B, C)$ have been observed in the photoemission spectrum of amorphous $GeSe_2$, as shown in Fig. 2.23. By clustering of $GeSe_{4/2}$ tetrahedra, the degeneracy of four Ge–Se bonding orbitals is resolved. The highest two levels A_1 and A_1' in the valence states come from the Se $4p$ lone-pair electrons, the next two levels A_2 and A_3 from the Ge–Se bonding electrons, the B level come from the Ge s-like bonding electrons, and the lowest C level from the Se $4s$ electrons. On the other hand, the three conduction bands (α, β, γ) have been observed in the inverse-photoemission spectrum. The first and second peaks has been assigned to the antibonding states of the Ge–Se covalent bonds, and the third one to the $4d$ and/or $5s$ states of both the Ge and Se atoms. Thus, roughly speaking, the top of the valence band of $GeSe_2$ are formed by the $4p$ lone-pair electron states of Se atoms, and the bottom of the conduction band consist of the antibonding states of Ge–Se covalent bonds. These electronic structures have been confirmed by some theoretical calculations [63,65,67].

Resonant Raman scattering in chalcogenide glasses

For studying the relation between localized electronic states and structural units, resonant Raman scattering is a powerful tool. The first observation of the resonant Raman scattering from an amorphous solid, As_2S_3 glass, has been reported by Kobliska and Solin [68]. Kawazoe *et al.* [69] have reported more detailed resonant enhancements of the Raman peaks of As_2S_3 glass, and have shown that the enhanced peaks arise from As–As and S–S homopolar bonds, which are assumed to provide the band tail states. Recently Tanaka *et al.* [70,71] have observed the resonant enhancements of the 430 cm^{-1} Raman band relative to the A_1 mode in GeS_2 glass. This resonance feature has been attributed to the structural units such as S–S dimers and/or Ge_2S_6 EST, producing the band-tail states.

2.3.2 Crystalline $GeSe_2$

Structure

Depending on growth temperature, germanium diselenide appears mainly in two crystallographic modifications [72]: the high temperature (β)–$GeSe_2$ with two-dimensional layered structure [73] (Fig. 2.25) and the low temperature (α)–$GeSe_2$ with a three dimensional crystal structure [74] (Fig. 2.26). In both phases, the basic structural units are $GeSe_{4/2}$ tetrahedra. In the β phase, the tetrahedra are connected both via common corners and via common edges. On the other hand, in the α phase, the tetrahedra are

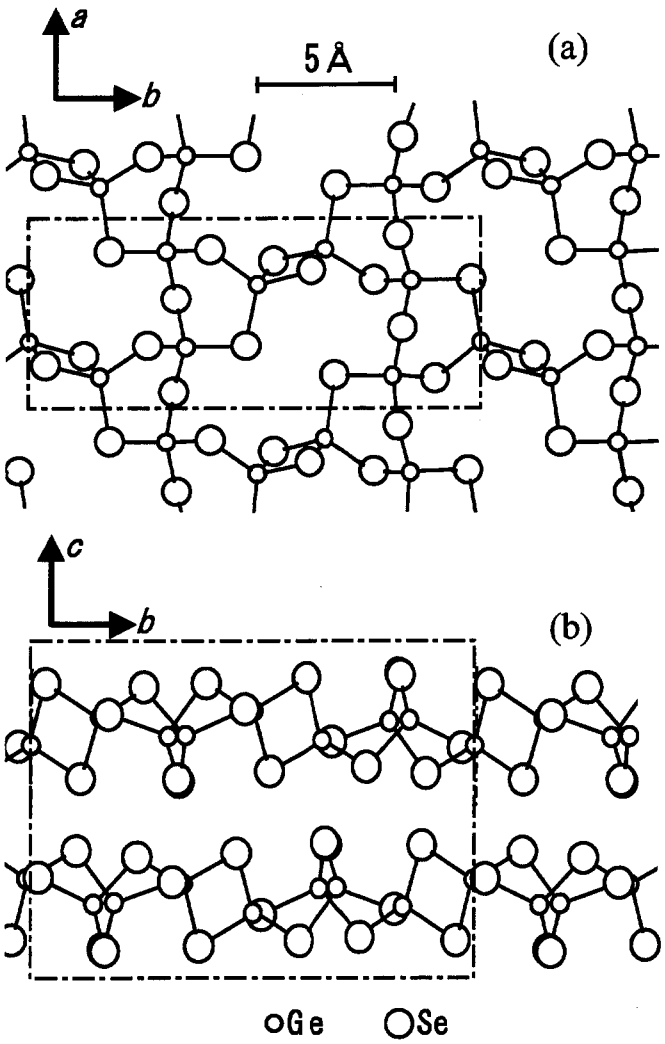

Figure 2.25: Projections of the structure of β-$GeSe_2$ (a) parallel and (b) perpendicular to the layer planes. The unit-cell is bounded by a dashed-and-dotted line.

connected only via common corners.

Vibrational properties

The vibrational properties of crystalline $GeSe_2$ have been investigated through the infrared and Raman scattering spectroscopy [56,72,75,76]. The β-$GeSe_2$ has two layers per unit cell. The corresponding space group is $P2_1/c$. These 48 atoms in a unit cell make 144 phonon branches (72 Raman active, 69 IR active and 3 acoustic modes). Factor group analysis predicts 36 A_g+ 36 B_g modes as Raman active modes. The twofold axis lies on the ***ab***-layer plane along crystallographic axis y, $C_2^y \parallel \boldsymbol{b}$. Then, the A_g

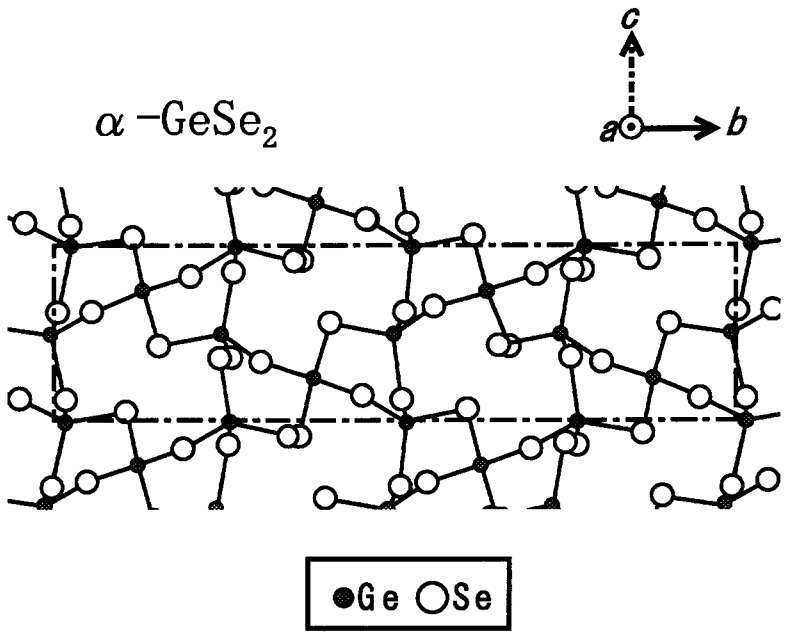

Figure 2.26: Schematic network connections in low temperature phases of crystalline $GeSe_2$ (α-$GeSe_2$). The unit-cell is bounded by a dashed-and-dotted line. The framework is a linear chain of CST units, and the chains are connected by CST units to form the three dimensional structure.

modes are observed for parallel (xx, yy, zz) and crossed (xz) polarizations while the B_g modes are observed for crossed polarizations (xy, yz). However, the full assignments of these expected phonons have not been completed yet.

Two characteristic peaks, A at 211 cm^{-1} (the most intense peak) and A^* at 216cm^{-1} have been studied by using a valence-force-field model combined with a bond polarizability model(VFF-BP) [59–61]. The A peak has been attributed to in-phase breathing vibrations extended along the chain of CST while the A* peak has been attributed to in-phase breathing vibrations quasi-localized at the EST. Figure 2.27 shows the calculated phonon dispersion curves as well as the VDOS for β-$GeSe_2$. The dispersion of the uppermost branch, which corresponds to the A^*mode, is small and this branch leads to a narrow peak of the VDOS at 215 cm^{-1}. On the other hand, the dispersion of the A mode is large and leads to a broad peak of the VDOS at 205 cm^{-1}. These features confirm that the A mode is extended along the chain structure, and the A^* mode is quasi-localized at the EST.

A characteristic feature of layered structure materials is the existence of "rigid layer" (RL) modes. These low-frequency Raman modes have been identified by Zallen *et al.* in layered chalcogenide crystals [77,78]. The RL modes are the Davydov partner of the

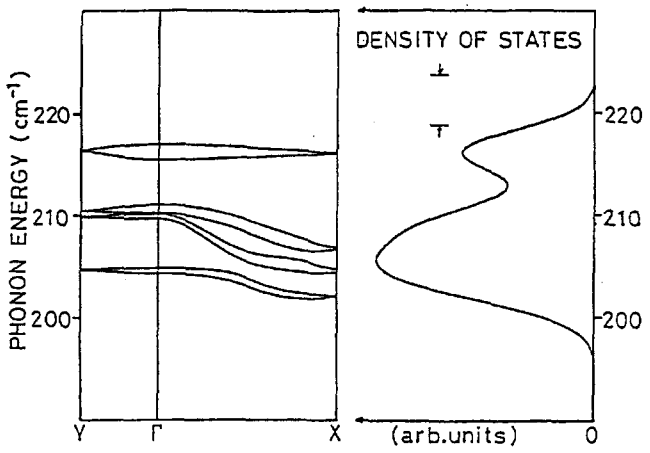

Figure 2.27: The phonon dispersion curves and the density of states calculated by the VFF model. The density of states is calculated on the assumption of Gaussian peaks with a width of about 5 cm^{-1} FWHM. From Ref. [60].

acoustic modes; the Davydov splitting is due to the existence of the weak interlayer interaction. The RL modes originate from the vibrations of the layers which move relative to each other as rigid units. They can be generally observed in the materials which have more than two layers in the primitive cell.

In the Raman spectra of crystalline $GeSe_2$, three RL modes are predicted by symmetry considerations. They are one compressional RL mode (B_g symmetry) in which adjacent layers beat against each other in oppositely directed motions normal to the layer plane, and two shear RL modes (A_g and B_g symmetry) in which adjacent layers slide over each other in oppositely directed motions parallel to the layer planes.

Resonant Raman scattering of β-$GeSe_2$

Matsuda *et al.* have studied the excitation energy dependence of the Raman spectra of β–$GeSe_2$ [58]. In most cases, the A peak is stronger than that of the A^* peak, but at 2.71 eV excitation in the $c(a,a)\bar{c}$ configuration, the A^* peak becomes stronger than the A peak, as shown in Fig. 2.28. On the other hand, there is no notable change in the ratio, A^*/A, in the $c(b,b)\bar{c}$ configuration. This feature has been connected with the exciton transition which is observed in the absorption spectra of $\boldsymbol{E} \parallel \boldsymbol{a}$ near 2.7 eV at room temperature [79]. They have proposed a model as follows. The exciton is related to the electronic transition from the $4p$ lone-pair states quasi-localized at the Se atoms of the edge sharing bridge to the s-like anti-bonding states of Ge atoms of the edge sharing bridge. They have recognized the enhancement of the ratio A^* band to A band to be due to an electron-phonon interaction between the exciton and the A^* phonon.

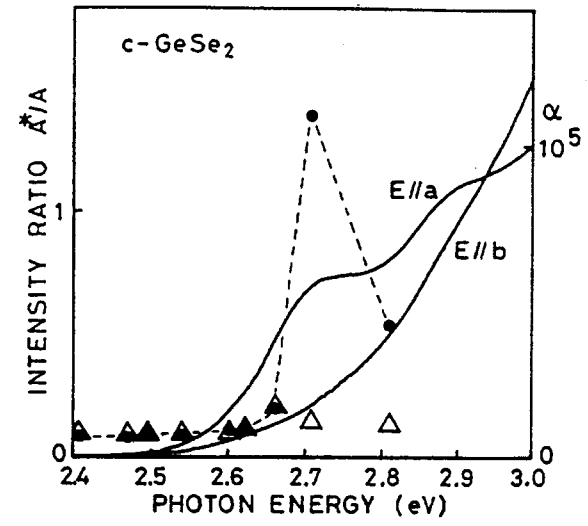

Figure 2.28: Excitation energy dependence of the Raman intensity ratio A^*/A of β-$GeSe_2$. The closed circles show the ratio in the $c(a,a)\bar{c}$ configuration, and the open triangles show the ratio in the $c(b,b)\bar{c}$ configuration. The dashed line is a guide to the eye. The absorption coefficient, α (in cm^{-1}) is also shown by solid lines for two polarization conditions. From Ref. [60].

Absorption spectra

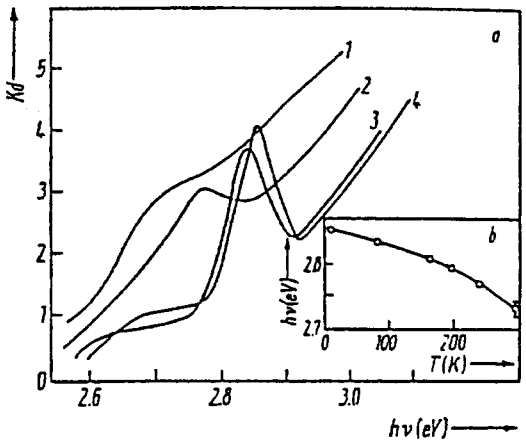

Figure 2.29: (a) Absorption spectra of β-$GeSe_2$ in the $\boldsymbol{E} \parallel \boldsymbol{a}$ polarization, at (1) 300 K, (2) 240K (3) 77K, and (4) 4.2K. The inset (b) shows temperature dependence of the exciton transition energy. The exciton absorption peak becomes sharp and moves toward the higher energy side with decreasing temperature. From Ref. [79].

Boiko et al. have reported a strongly anisotropic optical property of β-$GeSe_2$ [79]. In the absorption spectra at 4.2 K for $\boldsymbol{E} \parallel \boldsymbol{a}$ polarization, where $\boldsymbol{E}$ is the electric field of light, they have found an exciton absorption peak at 2.854 eV which has not been observed for $\boldsymbol{E} \parallel \boldsymbol{b}$ polarization. The exciton peak energy decreases with increasing temperature as shown in Fig. 2.29. The exciton transition energy is about 2.7 eV at RT.

Popović et al. have measured the absorption coefficient (α) in more dental have obtained the direct energy gap by extending the linear portion of the absorption curves to intersect with the $h\nu$ axis in the plot of α^2 versus $h\nu$ [80]. The direct energy gap is presented in Table 2.3. They have also suggested that the absorption where $\alpha > 1000cm^{-1}$ corresponds to direct transition while the absorption where $\alpha < 1000cm^{-1}$ corresponds to indirect transition.

Table 2.3: Direct energy gaps in c–$GeSe_2$

T(K)	E_g(eV)	
	E ∥ a	**E ∥ b**
300	2.50	2.49
77	2.675	2.685
4.2	2.725	2.735

Photoluminescence spectra

Due to the existence of strong electron-phonon interaction, radiative recombination in chalcogenide semiconductors is dominated by strong lattice relaxation following optical excitation; with a visible light excitation, the PL emission appears in near-infrared region. The relaxation processes following optical excitation have been subjects of considerable interest for understanding the mechanism of photoinduced structural changes in these materials [81–84].

The peak energy of the PL slightly depends on the excitation energy. The peak energy is about 0.99 eV with an excitation light of 2.54 eV, while 1.14 eV with an excitation light of 2.71 eV in β-$GeSe_2$ [85]. The decay time of the PL is about 300 μ sec at 4 K, and decreases to 25 μsec at 80 K [86]. The dependence of the decay time on excitation light energy is not quite clear yet.

A lot of similarity has been found in the PL spectra between the crystalline form and the glassy form in many chalcogenides. This similarity suggests a relaxation mechanism that arises from peculiarities of the chemical bonds rather than native defects or impurities. The $GeSe_2$ is also one of these materials, but according to the radiative decay curve, an apparent difference between the crystalline and glassy $GeSe_2$ can be observed [86,87]. The decay curve in glassy $GeSe_2$ consists of a fast component whose lifetime is about 0.4 μsec and a slow component whose lifetime is about 0.08$\sim$0.5 msec. The time profile in c–$GeSe_2$ is described by an exponential form while that of the slow component in g–$GeSe_2$ is described by a stretched exponential form which is frequently seen in the relaxational process of a random system.

Chapter 3

Relationship between network structures and glass transition

The central theme in this chapter is to determine the relationship between structures and dynamics in network glasses by using Raman scattering. To describe the network structures, we use the constraint counting theory that classifies networks into "floppy" and "rigid" ones according to their mechanical properties. We show a definite difference in relaxational behavior between the floppy and rigid glasses, and discuss the origin of the difference.

3.1 Introduction

A liquid cooled below its melting point may exist in a state of metastable equilibrium called a supercooled liquid. With further cooling, the atomic motions slow down. Below the glass transition temperature, the supercooled liquid falls out of configurational equilibrium and forms a glass. Upon cooling, relaxations in supercooled liquids bifurcates into a slow α-process and a fast β-process. The characteristic time constant of the slow process (τ_α) increases by more than ten orders of magnitude by cooling. The time constant is seen in macroscopic (viscosity) as well as microscopic (structural reorientation) observables [88–90]. On the other hand, the characteristic time of the fast process (τ_β) is an order of picosecond, and is nearly temperature-independent as measured by inelastic neutron scattering (time of flight spectroscopy) in several glass forming systems [91–94]. The physical origin of such a fast process and its possible connection to the α relaxation are questions which are at present completely unclear. The structural relaxations around the glass transition temperature (T_g) are subjects of increasing interest in connection with the poorly understood glass transition phenomenon. However, the fundamental information on the relaxation that is the correlation with the structures of glasses has not been clear. We discuss the structural relaxations in Ge_xSe_{1-x} covalent glasses in terms of network connectivity.

To describe the network structure, we use the constraint counting theory [2,3,9,15], where the network connectivity can be parameterized by simply using an average coordination number $\langle r \rangle$. A mechanical critical point ("stiffness transition") exists at $\langle r \rangle = 2.40$ ($x = 0.20$), where the number of constraints per atom equals the degree of freedom per atom. The character of the network undergoes a qualitative change from

being easily deformable at $\langle r \rangle < 2.40$ to being rigid at $\langle r \rangle > 2.40$; the network can be changed from a floppy network ($\langle r \rangle < 2.4$) to a rigid one ($\langle r \rangle > 2.4$) [9,15].

It was also shown that topological effects rather than chemical ones must be considered to explain the energetic relaxations among glassy configurations in Ge–As–Se chalcogenides as probed by infrared hole burning at cryogenic temperatures [95]. The relevance of the concept of $\langle r \rangle$ has also been explored in the liquid state [20,96,97]. These studies of ternary chalcogenide alloys provided evidence for a correlation between the rigidity percolation and the departure from Arrhenius behavior, i.e., the fragility. This raises a question of whether another key aspect of the glass transition, viz., the structural relaxation also shows a systematic composition dependence in this system.

3.2 Experimental

Ge_xSe_{1-x} glasses were prepared by a standard melt-quenching method. High purity Ge (99.9999%) and Se (99.999%) elements were etched in CP4 (a solution of HNO_3, HF, and CH_3COOH in a volume ratio 8:10:5) and a KOH water solution, respectively. The etched elements were sealed in an evacuated ($\sim 10^{-6}$ Torr) silica ampoule in a desired molar ratio. The ampoule was slowly heated up to 960°C in a rocking furnace and the melts were homogenized for at least 24 hours. Then, they were equilibrated at about 150°C above the liquidus for an additional 24 hours before quenching in iced water.

The experimental setup for Raman scattering is shown in Fig. 3.1. Raman scattering was measured in a backscattering configuration, excited by a DCM dye laser (1.83 eV) pumped by an Ar^+ ion laser (Spectra-Physics Stabilite 2017). At the excitation energy, resonant Raman effect is negligible. The excitation light was focused onto a rectangular region of about 2×0.2 mm^2 (line-focusing) with a low-power density less than 1 W/cm^2 to avoid any photo-induced structural changes and additional heating effects. The scattered light was analyzed with a triple grating polychromator (JOBIN YVON T64000) and detected by a charge-coupled-device (CCD) detector. The samples were sealed in a silica tube in an argon gas atmosphere ($\sim$360 Torr) to avoid oxidation, and they were heated stepwise in an electric furnace. The temperature during the accumulation for each spectrum was fixed within ± 1°C. The heating rate between the successive measured temperatures was about 3°C/min. During the accumulation, no change was observed in the spectra below T_g, and the changes were very small even above T_g except at the crystallization temperature. The glass transition temperature was measured by using a Perkin–Elmer model DSC–7 differential scanning calorimeter at a heating rate of 10°C/min.

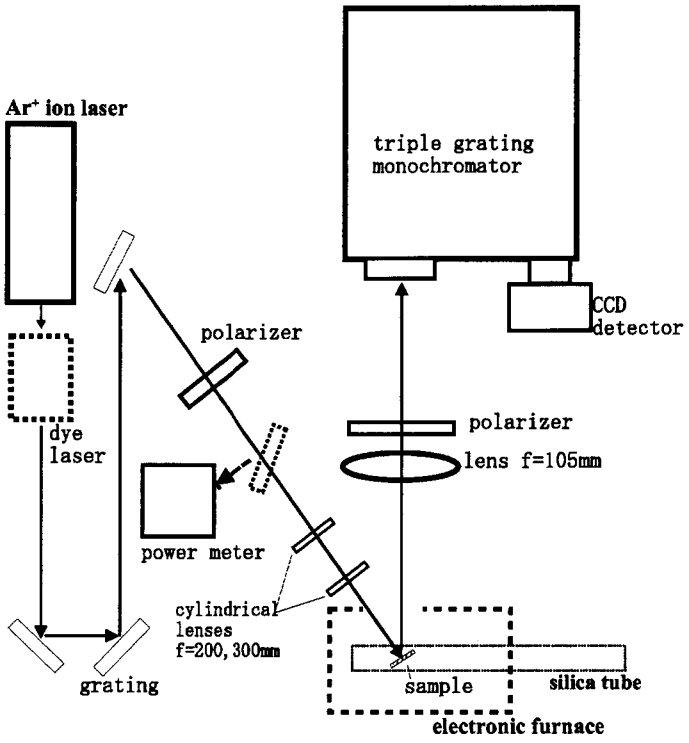

Figure 3.1: Experimental setup for the high temperature Raman scattering measurement.

3.3 Results and discussion

Generally, the low-frequency Raman spectra of glasses and supercooled liquids usually contain two contributions: relaxational (overdamped) and vibrational ones. Below T_g, the intensity $I(\omega)$ of the vibrational part of the spectra varies according to the Bose factor $n(\omega)$, i.e., $I(\omega) \propto n(\omega)+1$ in many glasses [98,99]. The vibrational part is termed the boson peak (BP). In contrast to the vibrational contribution, the relaxational part of the dynamical structure factor varies with temperature more strongly than the Bose factor, and it becomes virtually dominating at temperatures higher than T_g [100–102]. As an example of low-frequency Raman scattering, we show the Stokes Raman spectra of $Ge_{10}Se_{90}$ in Fig. 3.2. The Raman spectra are normalized, for convenience, by the integrated intensity of optical modes between 170 cm^{-1} and 330 cm^{-1}, including the A_1 mode of CST around 195 cm^{-1}, the breathing mode of EST around 211 cm^{-1}, and the stretching mode of Se–Se bonds around 255 cm^{-1} (for details of the optic modes, see, Section 2.3.1 and Section 4.3.1). The following discussion do not significantly effected by the normalization way; we focus on only the *line-shape* of the low-frequency spectra. At 30°C (the room temperature), the low-frequency spectra are dominated by a strong

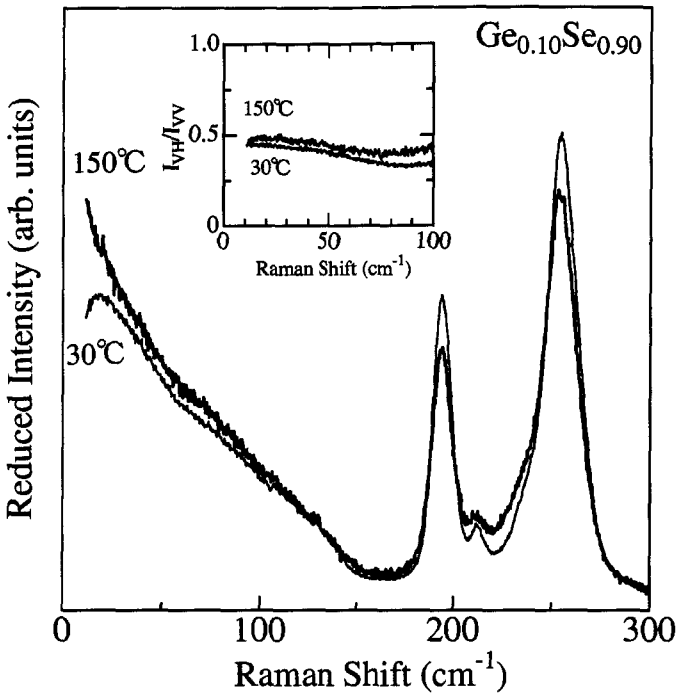

Figure 3.2: Raman spectra of $Ge_{0.10}Se_{0.90}$ glass at room temperature and above the glass transition temperature (T_g=100°C) in VV polarization configuration. The inset shows the depolarization ratio (I_{VH}/I_{VV}).

BP around 20 cm^{-1}. Since the Raman spectra are reduced by the temperature factor $[n(\omega, T)+1]/\omega$, the BP intensity should be independent of temperature. At 150°C a quasielastic contribution arising from relaxational modes is superposed on the BP. No Rayleigh line contribution is confirmed by the depolarization ratio, defined as a ratio of the scattered intensity with propagation of the electric field parallel to the scattering plane (I_{VH}) to the corresponding vertical one (I_{VV}), shown in the inset in Fig. 3.2. With decreasing the frequency to zero, no sudden drop is observed at either room temperature or above T_g. We inquire the composition dependence of the relaxational mode.

Figure 3.3 shows the normalized and reduced low-frequency Raman spectra of Ge_xSe_{1-x} glasses in the composition range ($0.07 \leq x \leq 0.35$) covering the rigidity transition ($x = 0.20$). At room temperature, the low-frequency spectra are dominated by the BP around 20 cm^{-1} in all the glasses. With increasing temperature, the quasielastic contribution resulting from relaxational modes appears around T_g in the "floppy" glasses ($x \leq 0.20$), and it grows. The relaxational modes are observed only in the floppy glasses ($x < 0.20$). The apperance of the relaxational modes in the threshold composition (x=0.20) is due to breaking parts of the bond-bending constraint from Se atoms [19]. We regard the $Ge_{20}Se_{80}$ glass as floppy ones in the following discussion as well.

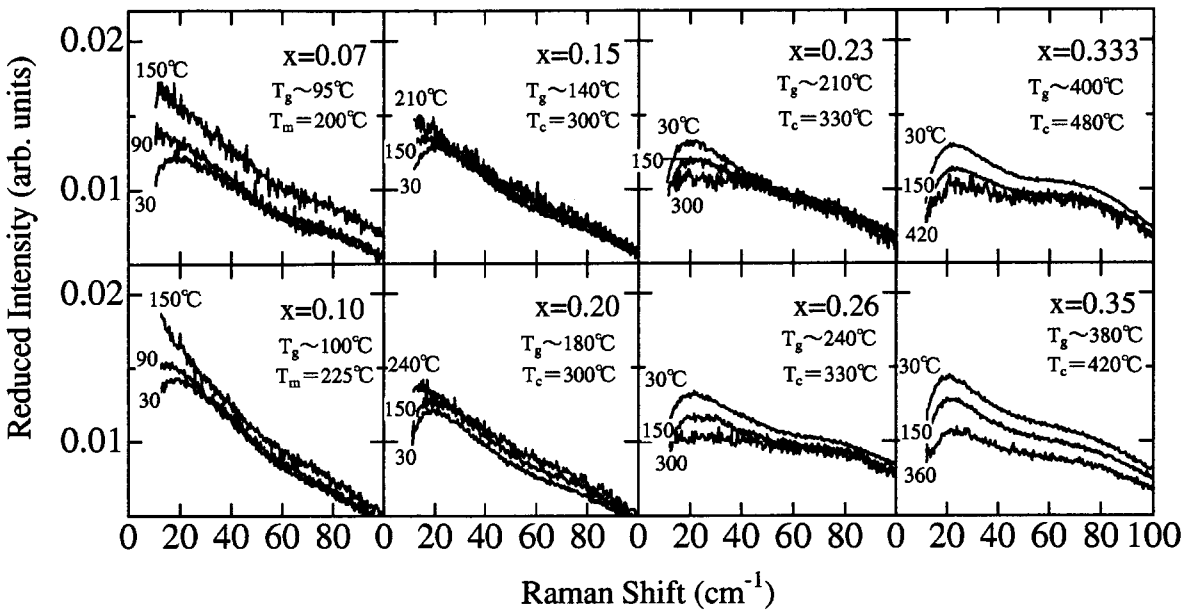

Figure 3.3: Temperature dependences of the low-frequency Raman spectra of Ge_xSe_{1-x} in VV configuration. The spectra are reduced by the temperature factor $[n(\omega, T) + 1]/\omega$, and normalized to the integrated intensity of the optic modes (170–330 cm^{-1}).

On the other hand, the strong quasielastic contribution is not detected in the rigid glasses ($x \geq 0.23$) even above T_g. On the contrary to the floppy glasses, the intensity around BP decreases with temperature. We will discuss the origin of such a decrease in Chapter 5 in terms of structural changes occurring in rigid glasses. which should be related with the instability due to the existence of configurational strains in the rigid glasses. Thus, it is found that the dynamics around T_g is distinctly different between the floppy glasses and rigid ones.

3.3.1 Relaxational modes

To discuss the relaxational modes further, we fit the quasielastic spectra. Two main approaches to the low-frequency Raman data fits have been suggested, where the quasielastic (QE) and BP contributions are represented either as a convolution or as a superposition.

The first approach, or the convolution model, relies on ideas originated from the "indirect" scattering mechanism of Winterling [103], where it is assumed that the QE line represents a low-frequency relaxation like part of the one phonon response function. In other words, the vibrational excitations are coupled to some relaxing variable that induces broadening to each frequency of the BP [104]. This way of interpretation of

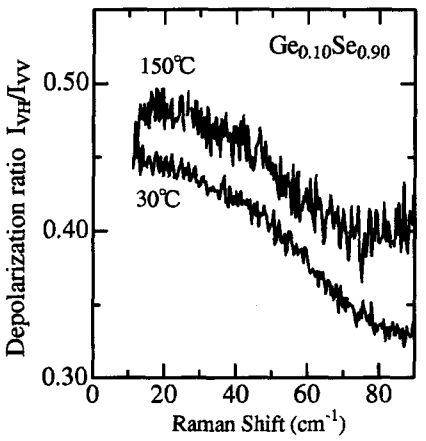

Figure 3.4: Expanded view of depolarization ratio of $Ge_{0.10}Se_{0.90}$ glass.

low-frequency Raman spectra has been essentially based on the following three putative similarities between the spectra of QE scattering and the BP. (i) There is a correlation between the dynamic character of an amorphous material (fragility) and the strength of the fast dynamics described by the relative strength of the QE scattering and the BP [102]. However, it has recently been shown that the correlation is not completely systematic [105]. (ii) The depolarization ratio is strictly constant, e.g., independent of the frequency, in the whole region of both the QE line and the BP since the QE line is caused by the BP vibration. This constancy is not hold good in some glasses [105]. In Ge_xSe_{1-x} glasses, the depolarization ratio in that frequency region is not constant as shown in Fig. 3.4. (iii) The phonon-photon coupling coefficient $C(\omega)$ is constant in the frequency range from the QE line ($\sim$0 cm^{-1}) up to the BP maximum frequency ($\sim$20 cm^{-1}). Recent experimental determinations of the phonon-photon coupling coefficient, through the comparison of neutron and Raman-scattering data, have shown that the statement (iii) does not definitely hold [106]. Thus, the aforementioned statements, which are used as the stronger evidence in favor of the convolution model, is based on incomplete informations. From the above argumentation we will employ the second approach, or the superposition model, in the subsequent analysis.

In the superposition model, the spectrum is modeled [107] as a sum of two separate contributions: QE contribution described by a Lorentzian line and the BP contribution. We assume a very small QE contribution at room temperature and a temperature-independence of the BP intensity in floppy glasses. These assumptions enable us to extract QE contribution by subtracting the spectrum at room temperature from those at high temperatures: $I^{qe}(T) = I^{exp}(T) - I_{BP}(30°C)$, where $I^{exp}(T)$ and $I_{BP}(30°C)$ are the experimentally measured intensity reduced by the Bose factor at T(°C) and 30°C, respectively. Although the extraction from the lower temperature spectrum ($<$ 30°C) might be better, the photoexcited carriers having the longer decay times at the lower temperatures may affect the spectrum more effectively in the Ge–Se system (for example, see, Chap. 7).

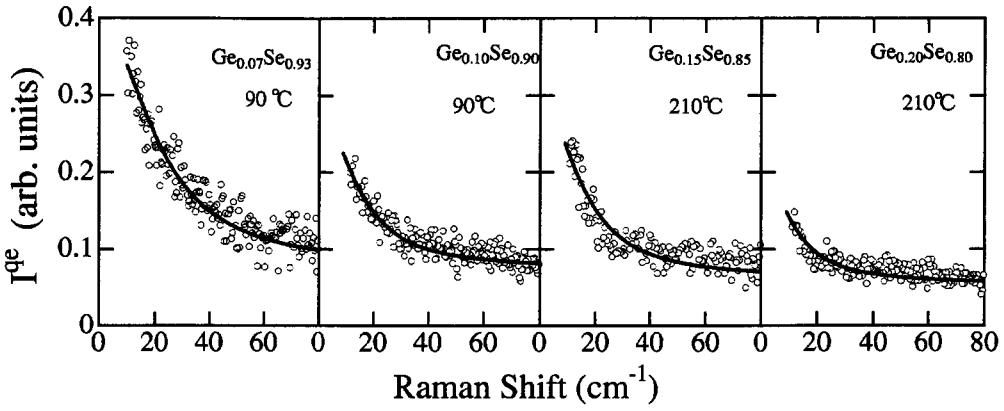

Figure 3.5: Representative sets of extracted quasielastic spectra of Ge_xSe_{1-x} glasses, subtracted by BP. Each spectrum is well fitted by a single Lorentzian function (solid line).

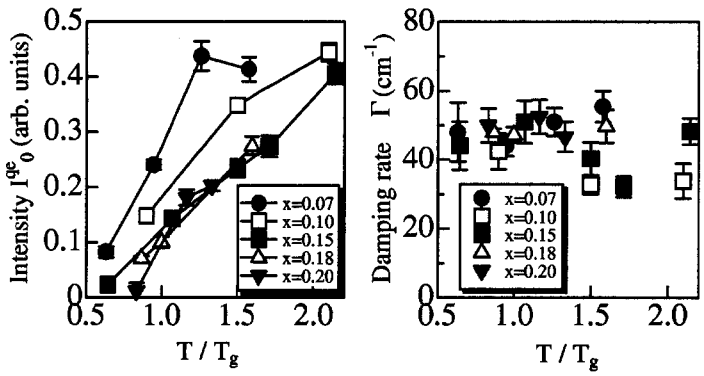

Figure 3.6: Quasielastic intensity I_0^{qe} and the damping rate Γ obtained by a Lorentzian fit to the low-frequency spectra (10–80 cm^{-1}) of floppy Ge_xSe_{1-x} glasses. Temperature is normalized to T_g.

Figure 3.5 shows the extracted QE contribution (10–80 cm^{-1}) being well fitted by a Lorentzian function:

$$I^{qe} = I_0^{qe}(\Gamma/2\pi)/[\omega^2 + (\Gamma/2)^2], \tag{3.1}$$

where I_0^{qe} is the QE intensity and Γ is the damping rate. The resulting fit-parameters, I_0^{qe} and Γ are presented in Fig. 3.6. In all of the floppy glasses, the QE intensity I_0^{qe} increases with temperature. At T_g, the QE intensity progressively increases with increasing Se content. The structural units involving Se atoms should play an important role on the relaxational motions. The damping rate Γ is nearly independent of both

temperature and composition. The temperature independence supports that the QE contribution originates from the fast (β) process of relaxation. From the inverse of the average damping rate, we can estimate the corresponding relaxation time in a first approximation. The estimated time of about 0.8 psec is consistent with the result of neutron spin echo measurement for amorphous Se, that the fast relaxation time has been much shorter than 2 psec [108]. The composition independence of the relaxation time demonstrates that the relaxation mechanism itself does not change significantly with composition.

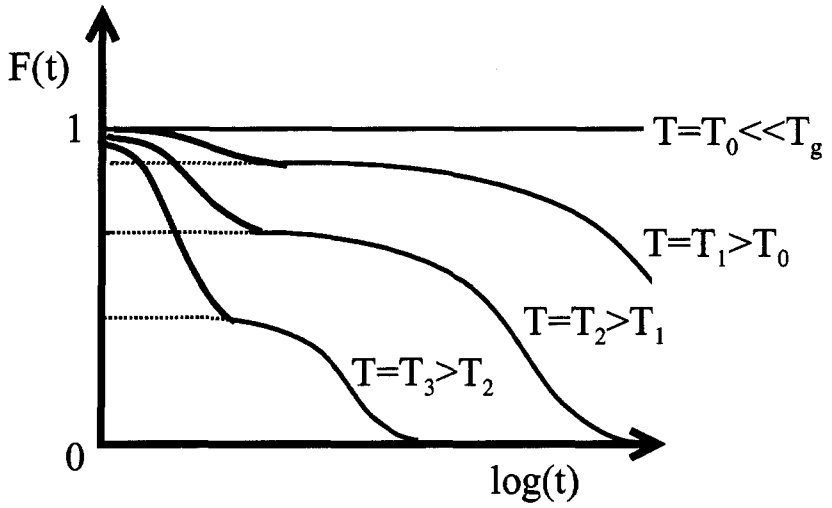

Figure 3.7: Schematic view of the time-dependent density-density correlation function $F(t)$ shown in a semilogarithmic plot. Each curve consists of a slow relaxation component (thin solid line) and a fast relaxation (thick solid line)

Now we explore a quantity that corresponds to the QE intensity, I^{qe}, in the dynamical glass transition theory. Let us consider the essential quantity to discuss the glass transition, that is the density-density correlation function $F(t)$. The function has been calculated by mode coupling theory (MCT) [109] and molecular dynamics simulation [110]. $F(t)$ can be experimentally obtained by neutron spin-echo experiments [108,111] and inelastic neutron scattering [91–94], as well. Figure 3.7 shows the schematic view of a typical shape of $F(t)$ curves at various temperatures. $F(t)$ is normalized to $F(0) = 1$. Each curve consists of a slow relaxation component (α relaxation) and a fast relaxation component (β relaxation). Historically, the slow component has been described by the empirical Kohlrausch-Williams-Watts formula [112]:

$$F(t) = f_0 exp(-t/\tau_{slow})^{\beta}, \tag{3.2}$$

where τ_{slow} is the characteristic slow relaxation time, β is the Kohlrausch stretch ex-

ponent typically ranging between 0.3 and 0.9 for structural glasses, and f_0 is the extrapolation to $t = 0$ of the slow relaxation component. The complement of f_0, namely, $1 - f_0$, is the relative "weight" of the fast relaxing part of the correlation function. The weight increases from a finite value at T_g to 1 far above T_g without a large change of the fast relaxation time, according to the theory and experiments. One notices that the quantity $1 - f_0$ behaves like I_0^{qe}. The density fluctuations can cause fluctuations in the susceptibility. Since the Fourier transformation of the space-time correlation function of the susceptibility fluctuations is generally proportional to the Raman scattering intensity (see, Eq. A.16 in Appendix), the fast relaxing weight of $1 - f_0$ should qualitatively reflect in the QE intensity I_0^{qe}. The weights of the fast and slow components correspond to the number of the degrees of freedom of atomic motions relaxing fast and slow, respectively. The QE intensity increasing with temperature will be due to the increase of the fast relaxing degrees of freedom.

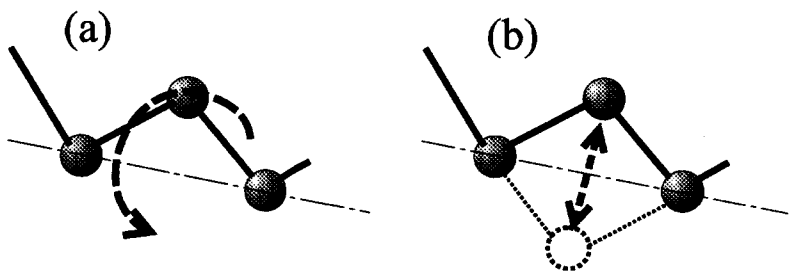

Figure 3.8: Schematic view for atomic arrangements of Se_n segments ($n = 3$). The damping (a) and the jumping (b) motions of the rotating segments are proposed for the dominant motions contributing to the QE scattering.

In view of the composition dependence of the QE intensity, we now identify the structural units mainly responsible to the relaxational motions. With increasing Ge content x, the QE intensity at T_g decreases. With further increasing x, the relaxational modes do not appear in the glasses at and above $x = 0.23$. The threshold composition is close to the rigidity transition threshold of $\langle r_c \rangle = 2.4$. Thus we discuss the relaxational modes in terms of the constraint counting theory. By considering a Kirkwood-Keating type of potential [113,114], the floppy networks, in which the number of degrees of freedom per atom (that is 3 in a three dimensional space) is larger than the number of constraint per atom, have low-frequency (ideally, zero-frequency) floppy modes [3,115]. The fraction of floppy modes available in a network is $f = 2 - (5\langle r \rangle/6)$; the fraction decrease to zero at $\langle r_c \rangle$ with increasing $\langle r \rangle$. The composition dependence of the floppy modes is very similar to that of the QE intensity. Thus, one arrives at the following

picture; a part of the motions in the floppy modes causes relaxational (damping or jumping) motions around and above T_g, which couple with light to result in the QE scattering. In other words, the number of relaxing degrees of freedom in the floppy modes corresponds to the weight of the fast relaxing component corresponding to the QE intenisty.

In Ge–Se system, the rotating motion of the Se_n ($n > 2$) segments, as shown in Fig. 3.8, has been proposed as the probable microstructural explanation for the floppy modes [10,116]. This kind of rotating modes has been discussed in computer simlations for modeling the flexible and rigid regions in the Se-containing network glasses and proteins [16,117]. We propose that the Se_n segments cause the relaxational motions involving damping or jumping motions around and above T_g. Such motions of the Se_n segments should play an essential role on the relaxational modes or QE.

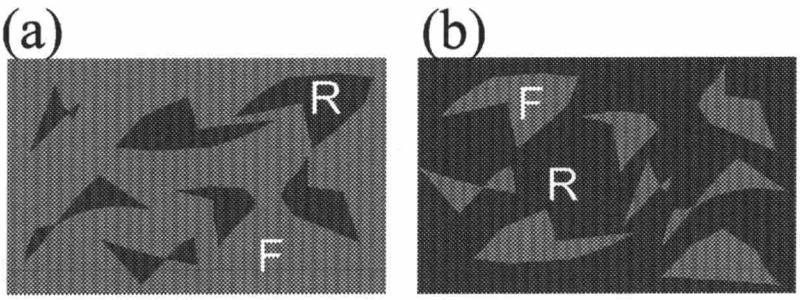

Figure 3.9: Schematic illustration of floppy and rigid regions. In floppy network (a), the floppy regions percolate while in rigid one (b), the rigid regions percolate.

Next we discuss the possibility of the interesting connection of the increase of the QE intensity with a free volume model [118]. The free volume model is one of the conventional theoretical approach for the liquid–glass transition, which can successfully describe the change of viscosity as well as the thermodynamic quantities, specific heat, and thermal expansion at the liquid-glass transition. According to the theory, a glass-forming system consists of solid-like and liquid-like cells. When the temperature increases, the fraction of the liquid-like cells p increases. When p is larger than a percolation threshold p_c, there is an infinite, connected, liquid-like cluster and the material turns into the liquid state. When p is less than p_c, it lies in the glass state. Thus, the liquid-glass transition is treated as the percolation of the liquid-like cells. We now connect the free volume model to the rigidity transition. The rigidity transition is also treated as a percolation problem [3]; in floppy networks floppy units percolate while rigid units do not, as shown in Fig. 3.9. We assume that, with increasing temperature, the floppy units become the liquid-like cells in which the motions relax or

damp. Since the floppy units percolate in floppy glasses, it follows that the liquid-like cells percolate around T_g. The percolation of the liquid units arising from the floppy units should achieve the strong QE line in our spectral range. We suppose that both of the increases of fast relaxing degrees of freedom and the number of the liquid-like units with temperature lead to the increase of the QE intensity. In our spectral range, the QE contribution is hardly observed in rigid glasses. This will be due to no "remaining" degrees of freedom in rigid units according to constraint counting theory; the number of constraints is larger than that of degrees of freedom. Then, even though the rigid units become liquid-like cells, the relaxational motions of the liquid-like rigid units will be quite different with floppy ones; the characteristic time may be beyond our spectral range.

3.3.2 Self-organization

We now return to discuss the relationship between the appearance of the relaxational modes and the connectivity of the glassy networks. We emphasize again that the relaxational modes observed in Se-rich glasses ($x \leq 0.20$) are hardly observed when the Ge content is slightly increased from $x = 0.20$ to 0.23. We feel that the transition for the appearance of the relaxational modes is surprisingly sharp beyond the expectation from the mean-field constraint theory.

Boolchand *et al.* [9] have suggested that the rigidity transition was richer in nature than that predicted by the previous mean-field constraint theory [2,3], based on the results of Raman scattering, Mössbauer spectroscopy, modulated differential scanning calorimetry, and molar volumes. They proposed the existence of an intermediate phase that starts near $\langle r_{(1)} \rangle = 2.40$ ($x = 0.20$) and is completed near $\langle r_{(2)} \rangle = 2.46$ ($x = 0.23$). Recent numerical simulations [29] have shown that the glasses in the intermediate phase are "self-organized" at some level. The network in the intermediate phase is rigid, but is formed with less (or no) overstressed region with the help of self-organization. WIth the self-organization processing, some constraints are removed from the overstressed region to apply on some floppy units. This process decreases the global constraints on the overconstrained region through sacrificing the degrees of freedom of the floppy region locally.

As displayed in Fig. 3.3, when the relaxational modes do not appear, the BP intensity decreases with temperature. The decrease of the BP intensity is caused by structural changes, as we will discuss in Chap. 5. The structural changes occurring in the intermediate phase ($x = 0.23$) should have a tendency to self-organize the network. The self-organization process moving the constraint on the overconstrained units to floppy ones should decrease the local degrees of freedom of some floppy units. By this process, the number of responsible units for the relaxational modes, which may still be

slightly remained in the $x = 0.23$ glass, is reduced to an undetectable number in our system. Thus, the self-organization process sharpens the transition from floppy to rigid in the relaxational dynamics.

3.4 Conclusions

We have found that the quasielastic contribution appears in the floppy glasses ($x \leq 0.20$), but it is undetectable in the rigid glasses ($x \geq 0.23$). The rigid glasses crystallize without the appearance of the relaxational modes. We comfirm that the quasielastic contribution originates from the fast (β) process of relaxation. We suceed in fitting the quasielastic contribution by using a single Lorentzian curve according to the superposition model for low-frequency Raman spectra. The quasielastic intensity increases with temperature, which corresponds to the increase of the weight of the fast relaxing component of density-density correlaiton function. The compositional dependence of the quasielastic intensity is well explained by the constraint counting theory under the assumption that the origin of the relaxational modes is from the floppy modes. We attribute the relaxation modes mainly to the damping or jumping motions of the rotating Se_n segments.

The shapness of the transition of the relaxational dynamics from floppy to rigid can be explained in terms of self-organization concept which is not only an extension of the constraint counting theory but also has broad consequences in many areas of condensed matter science [10].

Chapter 4

Trifurcated crystallization and inhomogeneity of $GeSe_2$ glass

In this chapter, we focus on the stoichiometric $GeSe_2$ glass, and study the thermally-induced structural changes by Raman scattering for over 50 samples. We find that the $GeSe_2$ glasses crystallize into three different phases, β–, α–, and ϕ–$GeSe_2$ ("trifurcated crystallization"), relating to the degree of the changes of glassy spectra which are almost identical at room temperature. On the basis of the observed structural changes, we discuss the nanoscopic structure and the thermal stability of $GeSe_2$ glass.

4.1 Introduction

Historically, the structure of $GeSe_2$ network glass has been described in analogy to SiO_2 as a continuous random array of chemically ordered structural units, i.e., $GeSe_{4/2}$ tetrahedra, where Ge–Ge and Se–Se homopolar or "wrong" bonds, called for broken chemical order, may occur accidentally [12]. However, intrinsic breaking of the chemical order has been suggested by Raman scattering and Mössbauer spectroscopy measurements [14,13,119,5]. Recently, a significant concentration of the wrong bonds has been predicted by theoretical calculations [62,120,121], and it has been directly confirmed by the isotopic substitution method in neutron diffraction [122]. The existence of the wrong bonds poses a new question of how the intrinsic wrong bonds affect the network stability. The wrong bonds play an important role on the structural changes in various kinds of thermally-induced [55,123] and photo-induced [38,5] structural changes. In this work, we study the role of the wrong bonds in the network stability in view of thermally-induced structural changes of $GeSe_2$ glass from RT to the crystallization temperature.

From $GeSe_2$ glass, two crystalline phases, β- and α-$GeSe_2$ shown in Fig. 4.1, can be produced either by heating [5,124] or by light irradiation [125,126]. The obtained crystalline phase depends on the growth temperature or on the excitation power density of the laser light [127,171]. The high temperature phase (β–$GeSe_2$) has a layered structure which consists of parallel chains of the corner sharing tetrahedra (CST) cross-linked with pairs of edge sharing tetrahedra (EST) [73,129]. The low temperature phase (α–$GeSe_2$) has a three dimensional structure constructed by CST only [5]. The similarity of the structures between the glass and the β–$GeSe_2$ has been intensively discussed

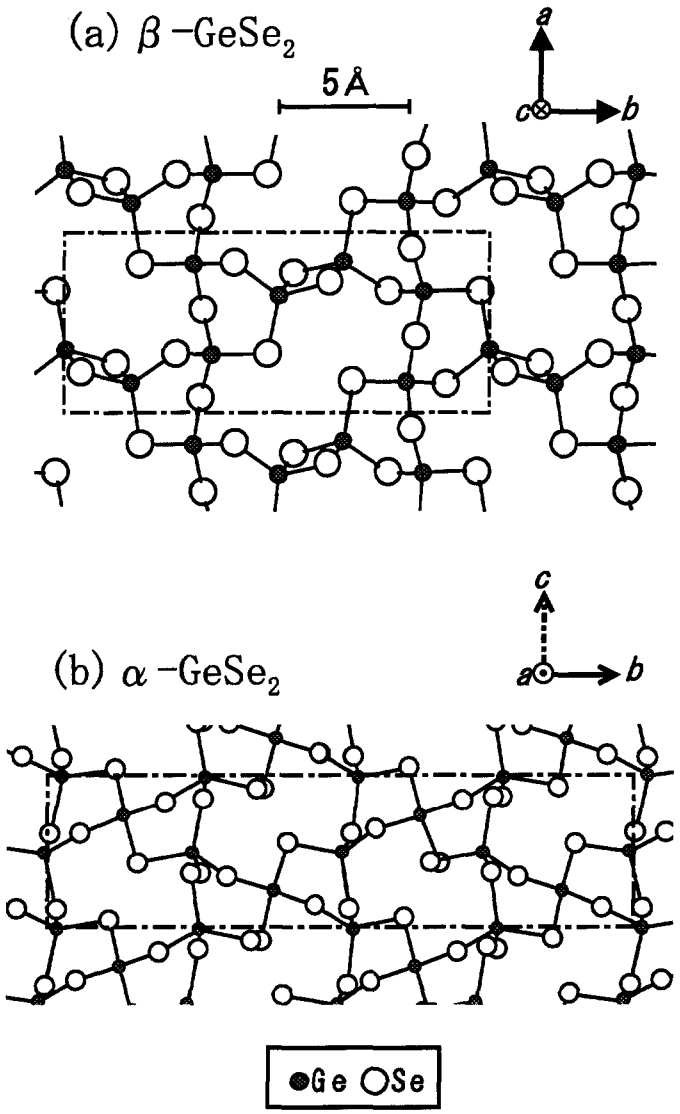

Figure 4.1: Schematic network connections in high temperature (a) and low temperature (b) phases of crystalline $GeSe_2$. The unit-cell is bounded by a dashed-and-dotted line. The common framework is a linear chain of CST units. The essential difference is that the chains are connected by EST units in the high temperature phase to form the layered structure while the chains are connected by CST units in the low temperature phase to form the three dimensional structure.

by Raman, X-ray, and neutron scattering measurements [5,50,51,56,124,130,131].

4.2 Experiments

High purity Ge (99.9999%) and Se (99.999%) elements were sealed in an evacuated fused-silica ampoule in vacuum of $\sim 10^{-6}$ Torr. The elements were reacted at 960°C, which is 220°C above the liquidus, and then quenched into iced water.

The experimental setup for Raman scattering is the same as shown in Fig. 3.1. Raman scattering was measured in a backscattering configuration, excited by a DCM dye laser (1.83 eV). The excitation light was line-focused ($\sim 2 \times 0.2$ mm^2) with a low power density less than 1 W/cm^2. The samples were sealed in a silica tube in an argon gas atmosphere ($\sim$360 Torr) to avoid oxidation, and they were heated stepwise with a rate of about 4°C/min in an electric furnace.

4.3 Results and Discussion

4.3.1 Trifurcated crystallization

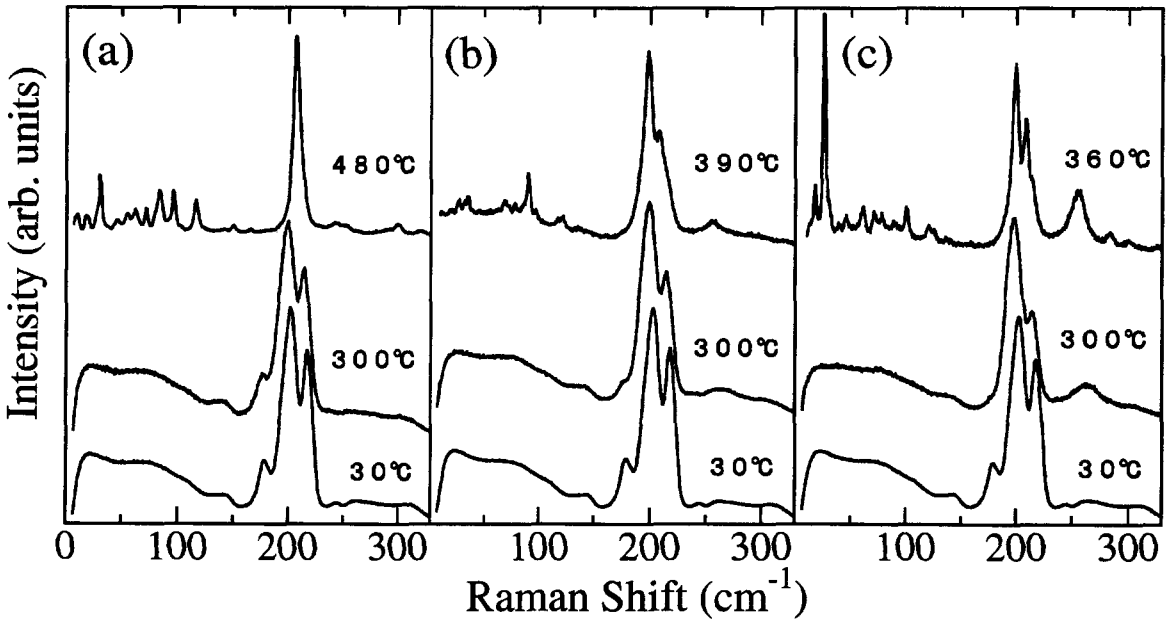

Figure 4.2: Three types of temperature dependences of the Raman spectra in $GeSe_2$ glasses. Each spectrum is normalized at the most intense peak around 200 cm^{-1}. Although all the Raman spectra at RT are the same, the glasses crystallize into (a) the β phase, (b) the α phase, and (c) the ϕ phase (see text) depending on the changes in the intensities of the three Raman bands around 200 cm^{-1}.

Figure 4.2(a), (b), and (c) show three types of temperature dependences of the

Raman spectra of $GeSe_2$ glasses from room temperature (RT) to the crystallization temperatures. As reviewed in Sec. 2.3.1, the Raman bands have been assigned as follows. The intense Raman band at 200 cm^{-1} at RT represents an A_1 in-phase breathing vibration of CST. The A_1 companion (A_1^c) band at 215 cm^{-1} is related to a breathing vibration quasi-localized at EST [60,62,5]. The A_G band at 176 cm^{-1} is interpreted as the stretching mode of Ge–Ge bonds involved in ethane-like units [56,62,132]. With increasing temperature, spectral changes are observed even well below T_g; the integrated intensity of the A_G and A_1^c bands decrease relative to that of the A_1 band. No distinguishable difference is observed among the Raman spectra at RT because all the measured $GeSe_2$ glasses are prepared at the same conditions. However, the degree of the spectral changes and the crystallized phase obtained by further heating definitely differs among samples. Here, we restrict the discussion on an initially appeared crystalline phase although some of them can be transformed into another one after holded at the same temperature for a long time ($\sim$ 60 hours) [133].

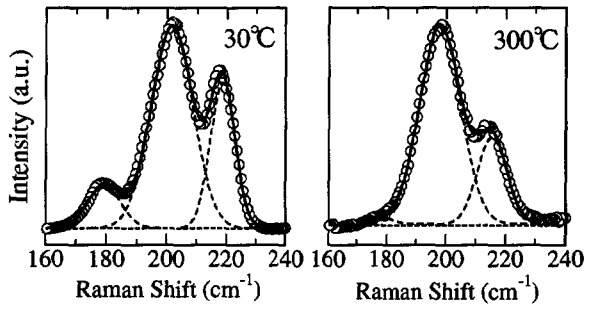

Figure 4.3: Raman scattering line shape at 30°C and 300°C, deconvoluted in terms of three Gaussians. The fitted curves (solid lines) reveal excellent fits.

We follow integrated intensity ratios of both the A_1^c and the A_G bands to the A_1 band by least-squares fitting the observed line shapes. The spectra around 200 cm^{-1} are well fitted by three Gaussians, as shown in Fig. 4.3. A strong correlation between the crystallized phase and the degree of the decreases of integrated intensity ratios, $S(A_G)/S(A_1)$ and $S(A_1^c)/S(A_1)$, is shown in Fig. 4.4. The β phase appears when the intensity ratios show slight decreases with increasing temperature before the increases above T_g. The α phase appears when the intensity ratios show larger decreases than the case of the β phase crystallization. An unreported Raman spectrum of a crystalline phase [Fig. 4.2(c)] is obtained when the intensity ratios show the largest decreases among three types of the crystallization processes. This crystalline phase is assigned to the ϕ phase which was reported to appear when Se-rich Ge_xSe_{1-x} glasses ($0.15 < x < 0.32$) were well-annealed [17,134] because the same crystalline spectrum as in Fig. 4.2(c) was

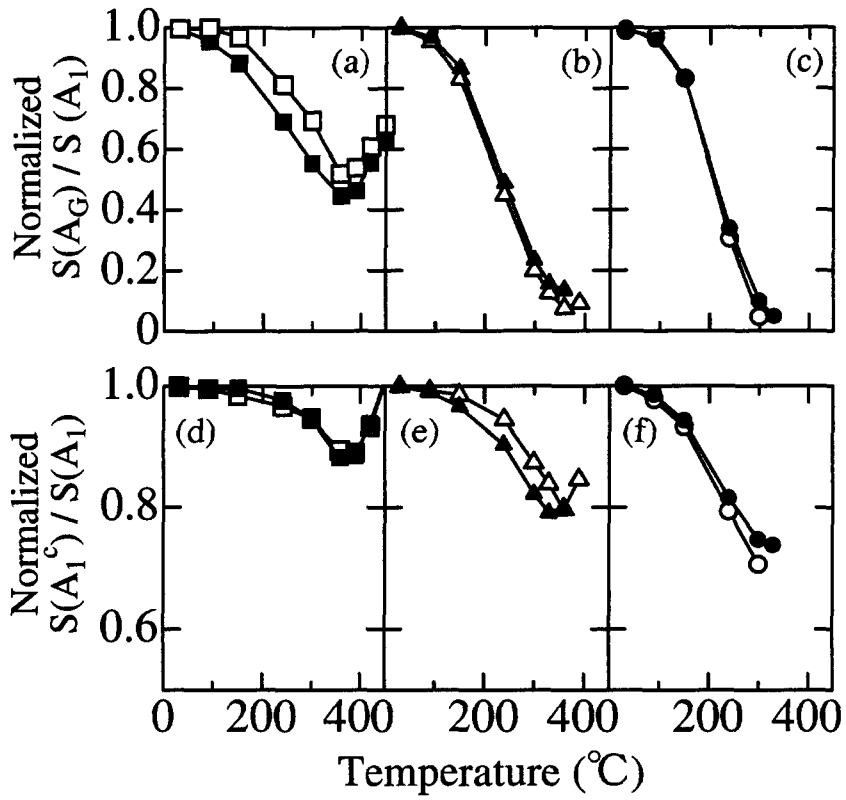

Figure 4.4: Integrated intensity ratio of the A_G band to the A_1 band (a)–(c), and the ratio of the A_1^c band to the A_1 band (d)–(f) as a function of temperature. The ratios are normalized to those at RT. The $GeSe_2$ glasses crystallize into the β phase [(a) and (d)], the α phase [(b) and (e)], and the ϕ phase [(c) and (f)]. The solid lines are drawn as guides for the eye and the error bars are included in the data symbols. Two representative sets of the ratios of samples are shown for each crystalline phase in the measured 50 sets. It is worth mentioning that if the changes of the intensity ratios are between those towards the β and α phases crystallization, a mixture of the β and α phases appears. Similarly, a mixture of α and ϕ phases is realized.

obtained by annealing the Se-rich glasses $Ge_{28}Se_{72}$ and $Ge_{30}Se_{70}$. The frequency of the strong Raman band around 200 cm^{-1} of the ϕ phase exactly coincides with that of CST vibrational mode of the α phase, implying that this crystalline phase is composed of CST. But definite differences are observed in the low frequency spectrum displayed in Fig. 4.5; for example, the Raman bands at 25 cm^{-1} and 60 cm^{-1} are hardly observed in the spectrum of the α phase. This assignment to the ϕ phase is consistent with the observed crystallization behavior; the crystallization of the ϕ phase, easily formed from Se-rich (x ~0.30) glasses, always follows a strong growth of the Raman bands of Se–Se

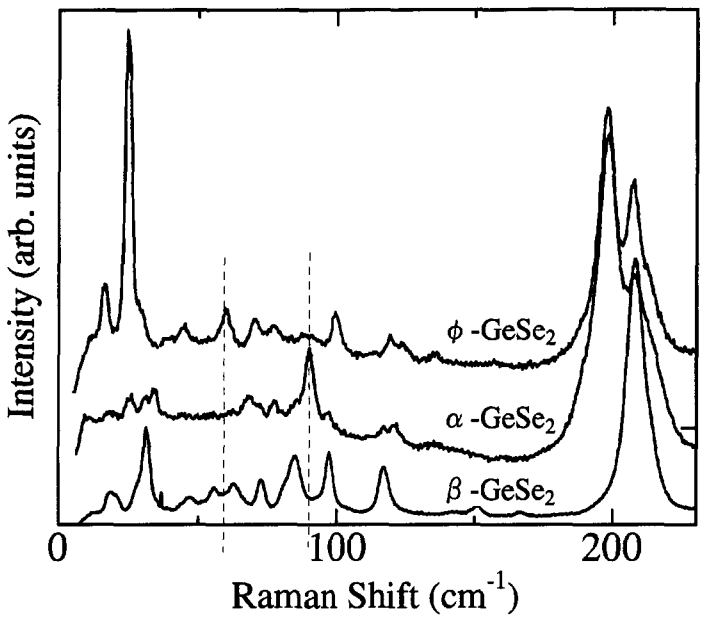

Figure 4.5: Expanded view of the Raman spectra of thermally formed crystals. The spectrum of the ϕ–$GeSe_2$ is similar to the α–$GeSe_2$ around 200 cm^{-1} but is different in the low frequency range; for example, the Raman peaks at 25 cm^{-1} and 60 cm^{-1} of the ϕ–$GeSe_2$ are very weak in the spectrum of the α–$GeSe_2$, and the peak at 90 cm^{-1} of the α–$GeSe_2$ is hardly observed in the spectrum of the ϕ–$GeSe_2$. The appearance of the very weak peaks of another crystalline phase will be due to a slight admixture of the phases.

stretching modes [55] around 260 cm^{-1}, as shown in Fig. 4.2(c).

Here we show temperature dependence of the full width at half maximum (FWHM) of the A_1 and A_1^c bands in Fig. 4.6. The width of the A_1^c band increases monotonically with temperature while that of the A_1 band decreases above a certain temperature. What has to be noticed is that the lower the temperature at which the A_1 band width starts to decrease, the larger the decreases of the $S(A_G)/S(A_1)$ and $S(A_1^c)/S(A_1)$ ratios. Since the $S(A_G)/S(A_1)$ ratio decreases much larger than the $S(A_1^c)/S(A_1)$ ratio in all the cases, we focus especially on the relation between the decrease of the $S(A_G)/S(A_1)$ ratio and the narrowing of the A_1 band. The decreasing of the $S(A_G)/S(A_1)$ ratio nearly to zero should be ascribed to the breaking of a significant number of Ge–Ge bonds in addition to the deformation. We believe that the breaking of the Ge–Ge bonds involved in ethan-like $Ge_2Se_{6/2}$ units leads to a formation and growth of CST units. This growth promotes an ordering of the CST units, and then narrow the A_1 band. This picture of CST formation from the Ge–Ge units explains the correlation between the degree of

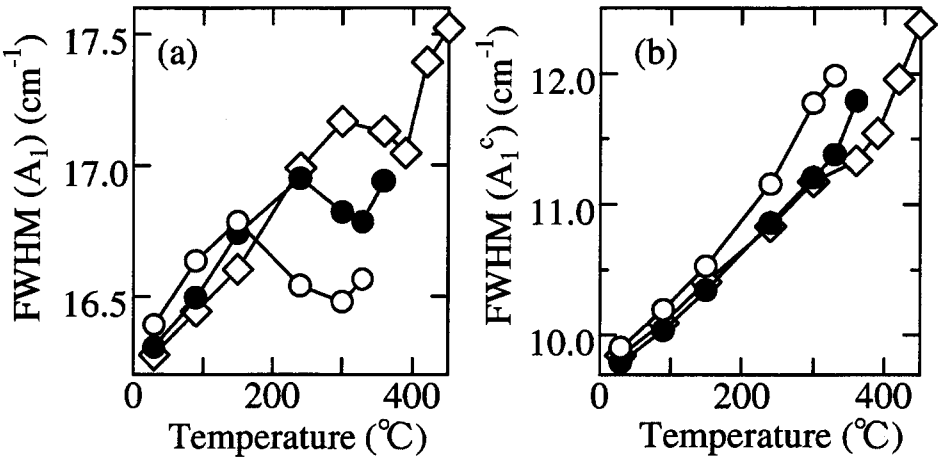

Figure 4.6: Temperature dependence of the full width at half maximum (FWHM) of the A_1 band (a), and the A_1^c band (b) in the $GeSe_2$ glasses which are crystallizing to the β phase (◇), the α phase (●), and the ϕ phase (○). Lines are added to guide the eye. The FWHM of the A_1 band increases with temperature and then starts to decrease while that of the A_1^c band increases monotonically.

the decrease of the $S(A_G)/S(A_1)$ ratio and the crystallized phase; the α and ϕ phases, composed of CST units, appear after the larger decrease of the $S(A_G)/S(A_1)$ ratio than the β phase.

4.3.2 Structural model

We explain the trifurcated crystallization by a structural model. The crystallization process that the smallest structural changes among three types of the crystallization processes lead to the β phase stresses the similarity of the structure between the $GeSe_2$ glass and the β phase. We propose that the fragments topologically similar to the β crystalline phase is significantly involved in the network of $GeSe_2$ glasses.

This proposed structure explains the rapid increase of the $S(A_1^c)/S(A_1)$ ratio above T_g before β phase crystallization, shown in Fig. 4.4(d). To crystallize to the β phase, rearrangements of the fragments must be needed. Below T_g, a high viscosity prevents rearrangements of the fragments. Above T_g, a significant lowering of the viscosity will allow the rearrangements. The rearrangements cause a growth of the β-like structures involving EST. This structural change increases the $S(A_1^c)/S(A_1)$ ratio. The following increase of the $S(A_G)/S(A_1)$ ratio will be discussed in the next section.

Boolchand *et al.* [135] have recently suggested the existence of a nanophase borne by Ge–Ge ethan-like units in the Ge-rich Ge_xSe_{1-x} glasses ($x \geq 0.33$), which is formed

separately from backbone of the glass, composed of the $GeSe_{4/2}$ tetrahedra. Together with our results, it follows that the Ge–Ge nanophases and the β–$GeSe_2$ like fragments, coexist in the as-quenched $GeSe_2$ glasses. It is probable that the Ge–Ge nanophase plays an important role in the trifurcated crystallization since the trifurcated behavior is not observed in $Ge_{28}Se_{72}$ and $Ge_{30}Se_{70}$ Se-rich glasses; the two Se-rich glasses always crystallize to the ϕ phase.

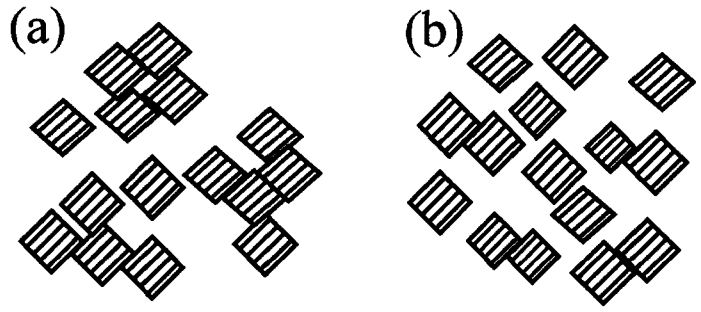

Figure 4.7: Schematic illustration showing size-inhomogeneity of Ge–Ge nanophases. (a) Large sizes of the Ge–Ge nanophases formed by high-concentrated Ge–Ge ethan-like units (shaded region). (b) Small sizes of the Ge–Ge nanophases due to relatively uniform distribution of the Ge–Ge units. It should be noticed that the average percentage of Ge–Ge units is the same for (a) and (b).

We introduce inhomogeneities of the Ge–Ge nanophases in size and the surrounding situations such as the sorts of surrounding units and the surrounding stresses. Generally, an inhomogeneity or a heterogeneity is a common property in disordered materials. For instance, an importance of the inhomogeneity to understand the dynamics at the glass transition has been indicated experimentally [136,137] and theoretically [138,139]. In our RT spectra, no evidence of inhomogeneities can be observed since the inhomogeneities are nanoscopic. However, the inhomogeneities of Ge–Ge nanophase at RT result in an observable inhomogeneity in degree of the formation of CST at high temperatures.

The initial inhomogeneities of the Ge–Ge nanophase cause a selective transformation from the ethan-like Ge–Ge units to the CST units. As the simplest case, we discuss a cause of the size-inhomogeneity as illustrated in Fig. 4.7. When the size of the Ge–Ge nanophases is larger than a certain volume, a large CST region is formed and then will grow due to a gain in volume free energy of the phase composed of CST units. On the other hand, when the size of Ge–Ge nanophase is much smaller than the volume, the Ge–Ge nanophase is not transformed to the CST region due to an insufficient gain in volume free energy. By this selective transformation, the scale of inhomogeneity

becomes large enough to observe it. Thus, we can read the inhomogeneities at high temperatures through the difference in the degree of CST formation among samples.

The increased scale of inhomogeneity in the degree of CST formation causes the trifurcated crystallization. The α or ϕ phase appears from an area where the size of CST region at the crystallization temperatures is large enough to compensate for any cost in interfacial free energy due to the gain in volume free energy of the CST phase. On the other hand, the β phase appears through the rearrangements of the β–$GeSe_2$ like fragments from an area where the CST regions remain smaller than the critical size even above T_g. It is important to note here that, from a thermodynamical point of view, the CST region can be stable even though their size is smaller than the critical size if their structure is not strictly crystalline. Besides the inhomogeneity in the CST formation, the inhomogeneity in the formation of Se-chain segments, which also comes from the initial inhomogeneities, plays an important role in the trifurcated crystallization; the excessive formation of Se chain segments leads to the ϕ phase. Thus, we attribute the origin of the trifurcated crystallization to the inhomogeneities in the initial distribution and surrounding situation of the Ge–Ge and Se–Se wrong bonds.

One of the reasons why our samples show such a clear trifurcated behavior may be the highness of our melt-quench temperature of 960°C; it exceeds the liquidus [17,140] by 220°C. High temperature quenching increases the percentage of the Ge–Ge bonds [135,141] and the inhomogeneities of the Ge–Ge nanophase. We believe that the high temperature quenching just enhances the properties causing the trifurcated crystallization, such as the existence of the Ge–Ge nanophase and the inhomogeneities; in other words, the properties are intrinsic since the annealed samples also show the trifurcated crystallization.

4.3.3 Reversibility

The stability of $GeSe_2$ glass is investigated by heating and cooling the glasses as follows. As-quenched $GeSe_2$ sample was heated and kept at 300°C (which is below T_g ~390°C) for five hours, and thereafter, it was cooled to RT. Figure 4.8 shows the temperature dependence of the $S(A_G)/S(A_1)$ and $S(A_1^c)/S(A_1)$ ratios in the first and the second heating cycles. The changes of the intensity ratios with temperature are nearly reversible in the first cycle, and they are fully reversible in the second one. The slightly irreversible parts in the first heating process are due to usual annealing effects. In the heating cycles, changes of FWHM's are also reversible.

The observed reversible changes are attributed to the temperature dependence of the stable structure of the glass, realized within a minute. At higher temperature (below T_g), the glassy structure similar to the ϕ or α phases composed of CST units becomes more stable than the structure of the as-quenched glass. The recovery of the

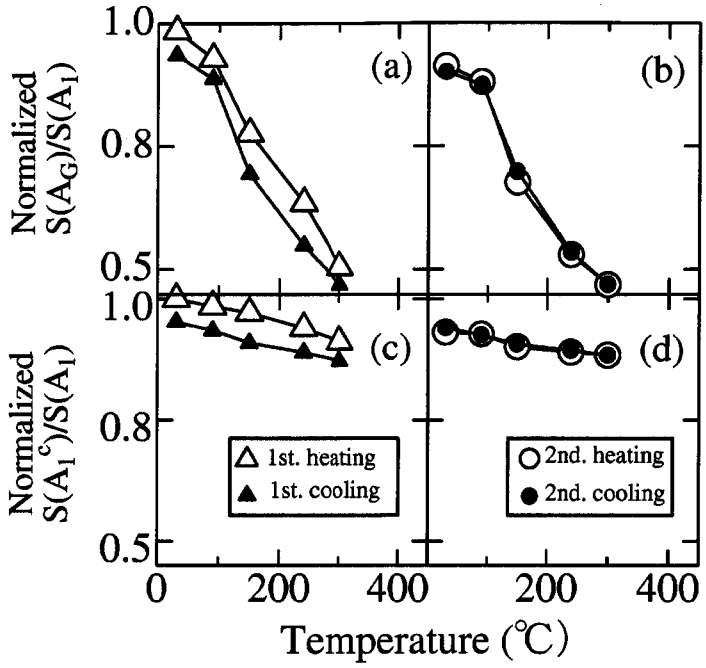

Figure 4.8: Integrated intensity ratio of the A_G band to the A_1 band [(a) and (b)] and the ratio of the A_1^c band to the A_1 band [(c) and (d)] as a function of temperature. The ratios are normalized to those at RT. The as-quenched sample was heated and kept at 300°C for five hours, and thereafter, it was cooled to RT. (a) and (c) shows the first cycle of the heat treatment and (b) and (d) the second one. Lines are added to guide the eye. The error bars are less than the size of the symbols.

$S(A_G)/S(A_1)$ ratio during the cooling process demonstrates that the network at a lower temperature prefers to involve a larger percentage of Ge–Ge *wrong* bonds. The recovery of the $S(A_G)/S(A_1)$ ratio is accompanied by that of the $S(A_1^c)/S(A_1)$ ratio; the recovery of Ge–Ge bonding is accompanied by the formation of EST units. This suggests that the Ge–Ge bonds are favored to possess the β–$GeSe_2$ like fragments. Thus, the Ge–Ge *wrong* bonds plays an indispensable role on the stability of the glassy structure.

In discussing the stability of the glass, it is very important to note that the glass is not in thermal equilibrium but in *quasi*-equilibrium. The structure of as-quenched $GeSe_2$ glass similar to the β phase arises from the quenching of the liquid structure [130,142]. Reflecting the β-like structure, when the structural changes with increasing temperature are small, the glasses do not crystallize into the α or ϕ phases even around 400°C despite the existence of a driving force to crystallize into these phases. The glassy state cannot surmount the high energy barrier to crystallize to the α or ϕ phases in the experimental time scale. This non-crystallization clearly shows the deviation of

the glassy structure from the equilibrium structure, namely the crystalline structure. Furthermore, the "stable" glassy structure varies reversibly depending on temperature. This is the evidence for the existence of the *quasi*-equilibrium state well defined by temperature. Thus, the observed trifurcated crystallization and the reversible structural changes clearly demonstrate the *quasi*-equilibrium nature of the glass.

Recently pressure induced amorphous–amorphous phase transition was reported in SiO_2 glass and amorphous ice [143–146]. The transition will be strongly related to the observed thermally-induced structural changes. In $GeSe_2$ glass, similar reversible change with the thermally-induced one is also caused by pressure; the as-quenched structure is changed to a quasi-three-dimensional structure composed of CST units [147]. The comparison between the thermally- and pressure-induced reversible changes is an interesting subject for future works in relation to the investigation of the amorphous–amorphous phase transition.

4.3.4 Relation to constraint counting theory

According to constraint-counting theory, the stoichiometric glass $GeSe_2$ is classified as an "overconstrained" glass where the number of constraints is larger than the degrees of freedom. The overconstrained glass has an excess configurational strain energy [2]. We now examine a connection between the observed structural change and physical properties expected in the overconstrained glass. The presence of the excess configurational strain energy has been suggested to lead to an anomalous thermal property [148]: thermodynamically 'fragile' but kinetically 'strong' in the sense of Angell [149]. The labels 'strong' and 'fragile' refer to the stability of the medium range order in the liquid against a temperature increase. High thermodynamic fragility is believed to reflect high density of local energy minima on a potential energy hypersurface [150]. This supports the existence of many metastable states whose depths of the potential energy are close to the ideal glassy state which have the lowest minimum except the crystalline state. In quenching from the melt of the thermodynamically fragile system, the liquid system is able to locate not only the ideal glassy state but also one of those metastable states. This will be the cause of the highly inhomogeneous distribution of the structural units in the as-quenched glass.

On the other hand, it is expected from the Adam-Gibbs equation [151] that low kinetic fragility arises from the high activation energy barriers for transitions between the energy minima. High energy barriers make it possible to store a strain energy. Structural transformations triggered by temperature introduce strains. Releasing parts of the strain and the excess configurational strain will assist another structural change. It is worth mentioning that even local structural changes taking place far from a given region can still affect the events in that region through the long-range strain field [152].

The strain field should have a "memory" of the initial potential energy minima. Such a strain field will play a key role in the highly reversible structural changes. The height of the energy barrier of $GeSe_2$ glass seems to appropriate to cause the structural changes. It is high, because of covalent bonding, enough to store the strain energy, and it is low, compared to a prototypical network as SiO_2 [153], enough to allow transformation easily triggered by temperature. Thus, both of the thermodynamically fragile and kinetically strong characters might be a necessary condition to cause the newly found structural change which is reversible and leads to trifurcated crystallization.

4.4 Conclusions

Structural changes with temperature in $GeSe_2$ glasses have been investigated by Raman scattering. First, we demonstrate the correlation between the spectral changes and the crystallized phase. The decreases of the $S(A_G)/S(A_1)$ and $S(A_1^c)/S(A_1)$ ratios are ascribed to the transformation from the ethane-like units involving Ge–Ge bonds to the CST units, which leads to an ordering of the CST chains. The degree of the formation of the CST units and the Se-chain segments determines the crystallized phase, β–, α–, or ϕ. Based on the trifurcated crystallization behavior, we suggests that the $GeSe_2$ glass involves significantly the β–$GeSe_2$ like fragments and the inhomogeneously distributed Ge–Ge nanophases and Se–Se bonds. Next, we show that the structural changes are reversible. The reversibility of the structural changes with breaking and forming of the Ge–Ge bonds demonstrate the importance of the Ge–Ge *wrong* bonds on the stability of the glassy network. The Ge–Ge bonds is favored to possess the layered fragments in the glassy state. The observed phenomenon seems to reflect the characteristic properties of the overconstrained network, which will serve for general understanding the nature of various kinds of reversible structural changes in the glass, such as pressure-induced transformations and light-induced processes.

Chapter 5

Low-frequency dynamics and crystallization

In the preceding chapter, we have demonstrated the correlation between the trifurcated crystallization [154] and the changes of the high-frequency optic modes. In this chapter, we analyze the low-frequency modes in relation to the crystallization process, and discuss the origin of the decrease of the BP intensity observed in rigid glasses.

5.1 Introduction

The short range structural order in amorphous materials can be usually established well from diffraction studies. On the other hand, the medium range structural order is not fully understand despite of many experimental data supporting the existence of medium range structural order [52,155–158]. Structural changes on a medium range scale have also been reported by neuron and X-ray scattering measurements [159–161]. However, it has been unclear how the network structure changes on the medium range scales.

In $GeSe_2$ glass the short range order is dominated by $GeSe_{4/2}$ tetrahedral units in addition to a small but significant amount of units involving Ge–Ge and Se–Se wrong bonds. In the preceding chapter, we have investigated structural changes attributed mainly to the short range structural transformation from the Ge–Ge ethanlike units to CST units.

In this chapter, we follow the changes in the low-frequency Raman spectra when such local structural transformations are occurring. In a number of models the low-frequency peak around 20 cm^{-1} (BP) in Raman spectra are explained by phonon localization due to strong scattering of phonons with wavelengths comparable to the length scale of static density fluctuations in the medium range (5–50 Å) [162], or to a regime of fractal dynamics (fractons) at higher frequencies [163–165]; the fracton modes are localized in nanodomains (~20 Å) [166,167] in Ge_xSe_{1-x} glasses. This allows us to study the medium range structural changes by the low-frequency Raman scattering.

5.2 Results and discussion

5.2.1 Comparison between low- and high- frequency dynamics

For the first order Raman process from harmonic vibrations, the scattering intensity is usually written in the form [53],

$$I(\omega, T) = C(\omega)g(\omega)[n(\omega, T) + 1]/\omega, \tag{5.1}$$

where $n(\omega, T) + 1$ is the Bose factor for the Stokes scattering, $g(\omega)$ the vibrational density of states (VDOS) and $C(\omega)$ the light-vibration coupling coefficient. The low-frequency Raman spectra reduced by the Bose factor are presented in Fig. 5.1 (a) and (b).

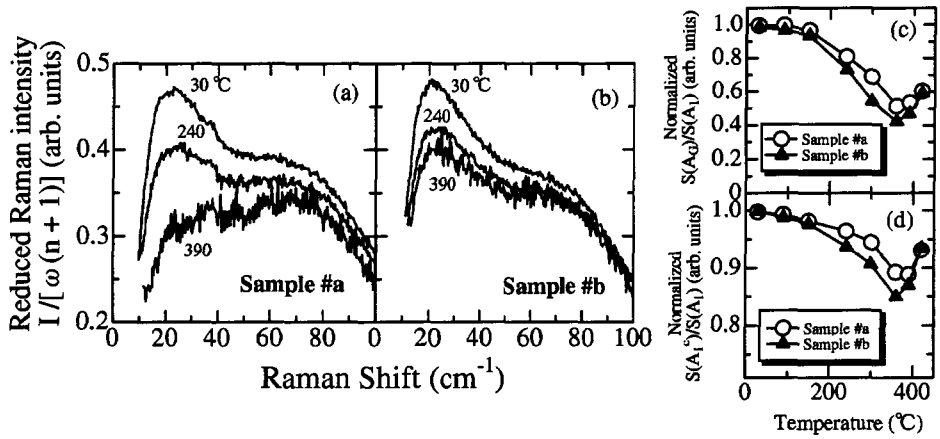

Figure 5.1: Comparison of reduced low-frequency Raman spectra [(a) and (b)] with integrated intensity ratios of high-frequency Raman modes [(c) and (d)] in two samples, #a and #b. The spectra are normalized at the peak intensity of the A_1 band. The intensity ratios are normalized to those at RT.

At RT, the spectra are dominated by a boson peak (BP). In many disordered materials, the low-frequency spectra can be scaled by the Bose factor to a temperature-independent lineshape at least below T_g [98,99]. However, we have observed a sample-dependent decrease of the BP intensity at high temperatures near T_g. Figure 5.1(a) and (b) show the two typical temperature dependences of the BP intensities. To compare them with the concurrent changes of the high-frequency spectra, we plot in Fig. 5.1(c) and (d) the temperature dependence of the integrated intensity ratios, $S(A_G)/S(A_1)$ and $S(A_1^c)/S(A_1)$. The temperature dependences of the intensity ratios are not so different between the samples #a and #b. In addition, with further increasing temperature, both samples crystallize into the same crystalline phase (a mixture of α and β phases, cf.

Fig. 4.4). However, the temperature dependences of the low-frequency spectra are significantly different; the BP intensity of sample #a decreases largely while that of sample #b decreases slightly. Thus, the low-frequency dynamics is not directly correlated with either the high frequency dynamics or the appearing crystalline phase.

5.2.2 Fracton model

To further discuss the sample dependent decrease of the BP intensity, we need to quantify the degree of the decrease. Here, we analyze the low-frequency vibrations around BP by using the theory of "fracton" dynamics [165] (see, Appendix B). This theory shows that the excess of the VDOS, responsible for the observation of the BP, can be understood on the basis of strongly localized vibrational excitation (fracton) in a fractal structure. Although the fractality is not a common picture for glasses, it has been shown that the fracton model is suitable for discussing the low-frequency dynamics in cross-linked networks such as polymers [168,169] and chalcogenide glasses [167,170,28]. One can then consider the fractal as a convenient model to describe strongly localized low-frequency vibrations in the networks. In the model, the density of such localized modes scales with frequency according to the law

$$g(\omega) \propto \omega^{\tilde{d}-1}, \tag{5.2}$$

where $\tilde{d}$ is the spectral dimensionality describing the degree of the localization of lattice vibrations [171] due to disordered structure of the networks. It has been reported that the coupling coefficient $C(\omega)$ of Ge_xSe_{1-x} glasses also shows a power law dependence in the fracton range [167].

Figure 5.2(a) and (b) show the double logarithmic plots of the two typical temperature dependences of the reduced Raman intensity following a power law as

$$I_R = I(\omega, T)/[n(\omega, T) + 1] = C(\omega)g(\omega)/\omega \propto \omega^{s-1}. \tag{5.3}$$

Each spectrum in the low-frequency range (20–80 cm^{-1}) is fitted well by a straight line in our wide temperature range. The frequency range is assigned to the stretching fracton-like localized vibrations. The spectra below 20 cm^{-1} is assigned to the Debye part of $g(\omega)$ [28,171], and the slope is nearly temperature-independent. The independence confirms the identification of the Debye range, which should not be too sensitive to the local structural changes. The power exponent s obtained from the slope of the fitted line is plotted in Fig. 5.2(c). The exponent s of sample #a increases superlinearly with temperature while that of #b increases almost linearly. The former corresponds to the large decrease of the BP intensity while the latter to the small decrease of it. Thus, this quantity s well describes the change of the vibrations around BP.

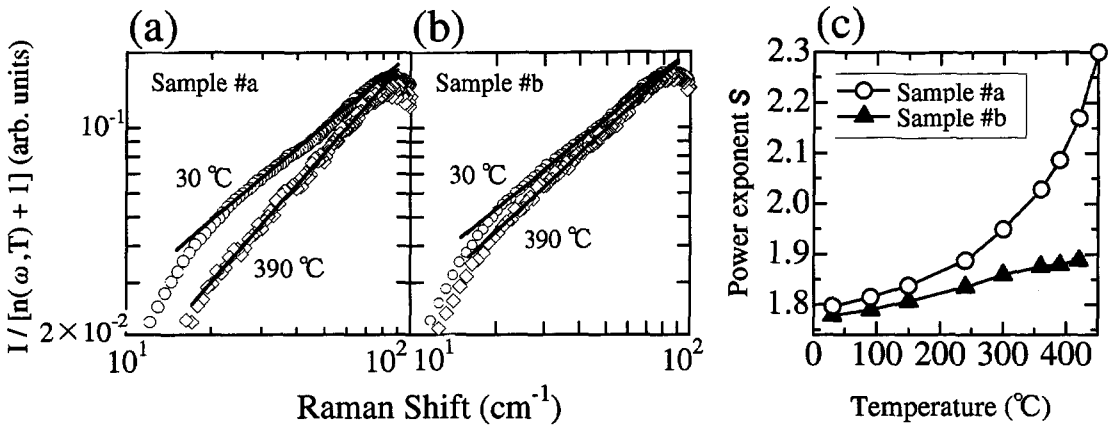

Figure 5.2: (a) and (b) show double logarithmic plots of the reduced Raman intensities at 30 °C and 390 °C. The solid lines represent the best fits of the intensities. (c) displays the temperature dependences of the exponents s obtained from the slope of the fitted line.

Here we discuss the quantity s. Comparison of the Raman spectra with the inelastic neutron ones [168,172,173], as well as with heat capacity data [174], has demonstrated that $C(\omega)$ is nearly proportional to ω in numerous glasses at RT. In other words, the power exponent of $C(\omega)$ is close to unity. Under the condition, the reduced Raman intensity represents the VDOS $g(\omega)$, and the power exponent s equals to the spectral dimensionality $\tilde{d}$.

With increasing temperature, due to the occurrence of structural changes, the proportionality for $C(\omega)$ may not be hold. Duval *et al.* [172] have derived the detailed expressions of $C(\omega)$ in fractal systems. In the case of a Raman mechanism of dipole induced dipole scattering, which explains well the low-frequency spectra of many disordered systems [175,176], the exponent of $C(\omega)$ can be described by only the two parameters, $\tilde{d}$ and the fractal dimension (D_f), although the formula depends on the system and the scattering process. We assume that the temperature dependence of $\tilde{d}$ is much larger than that of D_f determined by the glassy *structure* since the local *structural* change indicated by high-frequency modes do not directly correlate with the change of the power exponent. Although crystallizations into α or ϕ phases follow larger structural changes than the β crystallization, the temperature dependences of s are not always larger. Thus, the temperature dependence of s should reflect that of $\tilde{d}$.

5.2.3 Correlation between low-frequency dynamics and crystalline phases

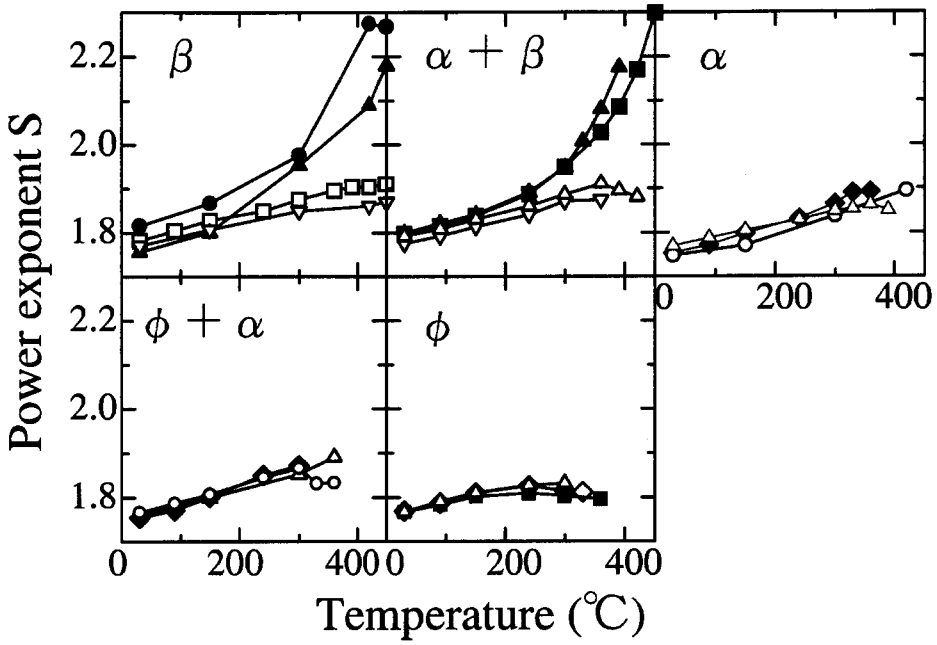

Figure 5.3: Temperature dependence of the exponent s classified according to the phases to which the glasses crystallize by further heating. Different symbols correspond to different samples. In the measured 50 samples, only the representative ones are plotted. The lines are guides to the eye.

Fig. 5.3 displays temperature dependences of s for many samples. They are plotted separately according to which phase the glasses crystallize into. In almost all the cases, s increases with temperature. We attribute the increase of s to a decrease of the localization degree of the vibrations. For example, a change of the network topology to decrease the number of dead-ends of the network (see, a nodes-links-blobs model depicted in Appendix B.2) weakens the localization of the lattice vibrations.

The behaviors of s can be roughly separated into two types. One is the superlinear increase exceeding 2, and the other is the almost linear increase not exceeding 2 at all the temperatures. The value of s exceeding 2 indicates $\tilde{d} > 2$ if the relation $C(\omega) \propto \omega$ still holds at the high temperatures. Such a high value of $\tilde{d}$ is anomalous within the usual fracton theory. This anomalous increase can be explained in terms of "bifractality" related to a high anisotropy of the structure to which the vibrations are localized. By making a Cartesian product of two fractals (bifractal) [177], it is possible to construct fractal lattices with $\tilde{d} > 2$. Thus, we attribute the anomalously large increase of s to a

Table 5.1: Correlation between the crystallized phases and the low-frequency dynamics. The number ratios of samples which crystallize into the β, α, ϕ, and their mixtures to that of all the measured samples (50) are listed. The number ratios of samples showing $\tilde{d} > 2$ to that of the samples which crystallize to the phases are also listed.

	β	α+β	α	ϕ+α	ϕ
Crystallization into the phase	8/50	24/50	5/50	9/50	4/50
Showing $\tilde{d} > 2$ when crystallizing into the phase	3/8	13/24	0/5	0/9	0/4

formation of a highly anisotropic structure in a medium range.

We now discuss the correlation between the crystallized phases and the anomalous increase of s. The number of samples to show the anomalous increase relative to the number of samples crystallizing into a phase is listed in Table 5.1. In our 50 measured samples, about one sixth and about one half of the glasses crystallize into the β and α+β (mixture) phases, respectively. Only when the glasses crystallize into these phases, $\tilde{d} > 2$ is observed. In other words, the glasses showing $\tilde{d} > 2$ always crystallize into the phases involving the β-$GeSe_2$. We suggest that the growth of the β–$GeSe_2$ like fragments in a medium range can change the network topology to increase the spectral dimensionality to an anomalously high value. The correlation with the crystallized phase is consistent with the layered or anisotropic structure of the β–$GeSe_2$ fragments.

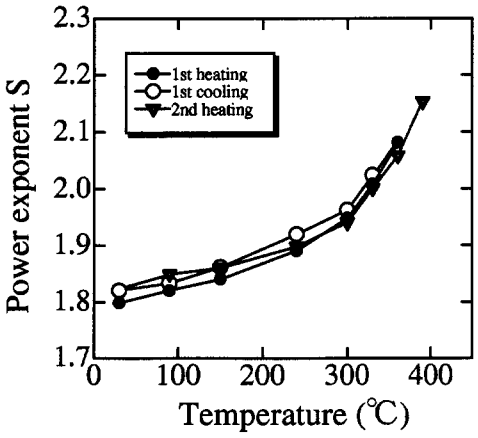

Figure 5.4: Reversibility of spectral dimensionality. The sample is heated to 360°C and then cooled to 30°C (1st heating cycle). After that, the sample is reheated until it crystallizes (2nd heating).

In many disordered systems, the medium range order has been signified by the first sharp diffraction peak (FSDP) [155,156]. The FSDP of the $GeSe_2$ glass behaves anomalously with temperature: the peak grows as the temperature is increased in a totally reversible manner [159–161]. This phenomenon has been interpreted in terms of the existence in the glass of structural elements derived from the corresponding β

crystalline structure. We emphasize that the change of s with temperature is also nearly reversible, as displayed in Fig. 5.4. These facts give support to our model for the low-frequency dynamics which is related to the growth of β like fragments.

5.2.4 Relation between spectral dimensionality and crystallization process

To further investigate the role of the growth of β like fragments in the increase of $\tilde{d}$, we examine the relation between $\tilde{d}$ and the growth of the β crystal. Here, we restrict our discussion to the glasses crystallizing into the β phases since the crystallization of the mixture of α and β phases will be complex. In addition, structural changes probed by high frequency Raman modes, is the smallest in the glasses, as demonstrated in Chap. 4. The change of D_f will be negligible, and we can trace the change of $\tilde{d}$ exactly.

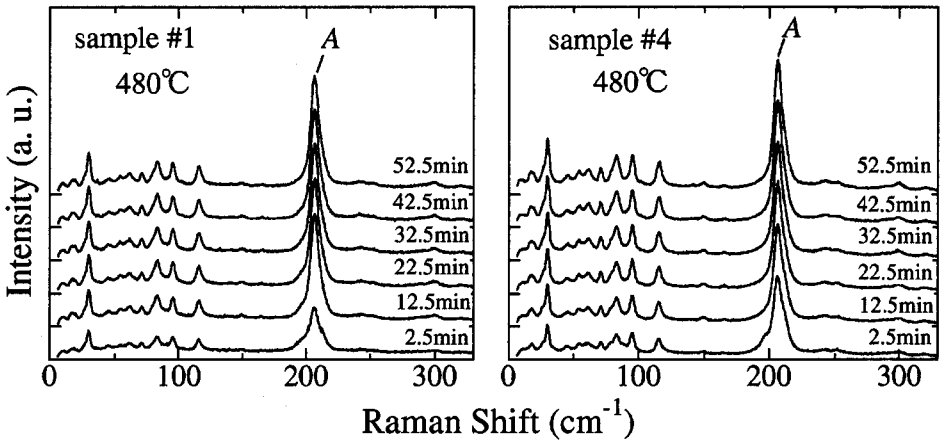

Figure 5.5: Time-resolved Raman spectra representing β crystallization at 480°C. The times after the temperature reached 480°C are shown. The sample numbers correspond to those in Fig. 5.6. The A peak is due to the CST breathing vibration of crystalline β phase. (for details of the crystalline spectrum, see, Chap. 8). The spectra are displaced vertically for clarity.

Figure 5.5 shows the time-resolved Raman spectra in the β crystallization of two representative glasses at 480°C. In the heating process from 30°C to 480°C, the sample #1 shows a superlinear large increase of s while the sample #4 shows a linear small increase, as plotted in Fig. 5.6(a). At 450°C both samples are still in the glassy state. With increasing temperature to 480°C (by taking 10 min), Raman peaks of the β crystalline phase appear. No significant differences are observed in the spectral shape of the crystallized glasses. However, the growth rate of the crystalline peak (A) differs.

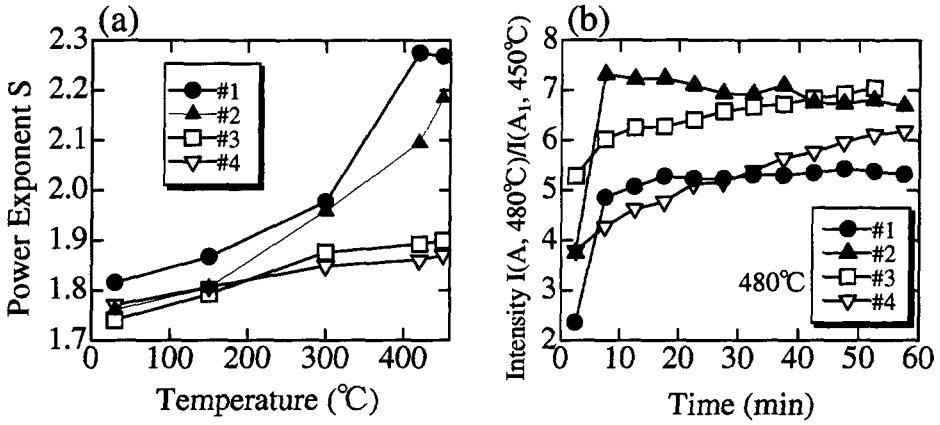

Figure 5.6: Comparison of the temperature dependences of $\tilde{d}$ (a) and growth curve of β crystalline phase (b) for representative 4 samples #1~#4. The intensity ratio of the A mode of the crystalline phase at 480°C to the A_1 mode of the glass at 450 °C is plotted. The lines are guides to the eye.

In order to compare the growth rates of different samples, we plot in Fig. 5.6(b) the intensity of the A peak normalized to that of the A_1 peak of the glass at 450°C. Since the β crystallization may start before the temperature reaches 480°C, we focus on the shape of the growth curve rather than the absolute value of the growth time. In the glasses showing the large increase of s ($s > 2$, sample #1 and #2 in Fig. 5.6), the A peak grows rapidly and then the growth of the intensity is nearly saturated. On the other hand, in the glasses showing the small increase ($s < 2$, sample #3 and #4), the A peak grows gradually and the growth is not saturated at least within an hour. Although only the representative data (4 samples) are shown in the Fig 5.6 for clarity, this correlation holds in all the glasses crystallizing into the β phase (8 samples).

We explain the correlation by nanoscopic picture of the growth of the β like fragments. Remembering that the large increase of the power exponent s is related to the growth of β like fragments, we propose the following picture for the sample dependent low-frequency dynamics and the β crystallization process. We suggest an ordering of network structure in a medium range induced by heating. The ordering is assumed to decrease the number of obstacles to lattice vibrations, such as dead ends, inducing localization of the vibrations. Such an ordering increases the exponent s. In addition, thef ordering forms strongly connected regions relative to the surroundings, which is similar to the β phase; we call it here "nanodomain". The scale of the strongly connected region is assumed to be nanoscopic and is larger than the scale of Ge–Ge nanophases. Figure 5.7(a) shows the β crystallization process of the sample showing the large increase of the power exponent s. The sample can become highly ordered by heating and

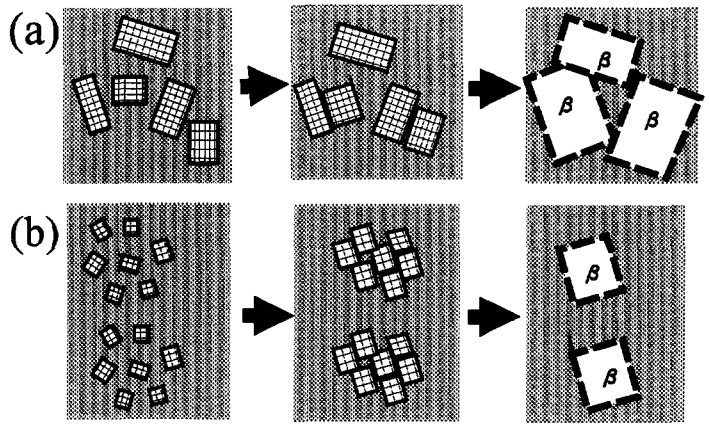

Figure 5.7: Schematic illustrations of the β crystallization processes when the power exponent s increases largely (a) and slightly (b). The checked rectangles represents strongly connected region similar to the β crystal. The region may not be surrounded by empty spaces, but by weakly connected regions.

has relatively large nanodomains (left figure). With increasing temperature the nanodomains will start to rearrange around T_g (middle figure), and forms nucleus of the β phase (right figure). In this case, we expect that during the growth of the nucleus, the β crystals crush against each other and the growth is saturated. On the other hand, in the sample showing the small increase of s [Fig. 5.7(b)], the ordering degree is low and the sample has relatively small nanodomains (left figure). With increasing temperature, the nanodomains will start to rearrange around T_g (middle figure). In this case, an assembly of the small nanodomains will be needed to form the nucleus (right figure). Then, the separation between the nucleus is enough to grow the β crystals and so, we expect that the growth is not saturated within our experimental time.

5.2.5 Low-frequency dynamics of rigid glasses

As we have shown in Fig. 3.3 in Chap. 3, the decrease of BP intensity is observed only in the rigid Ge_xSe_{1-x} glasses ($x \geq 0.23$), and the degree of the decrease of the BP intensity increases with increasing $\langle r \rangle$. Let us extend the picture of the increase of s, or the decrease of BP intensity in $GeSe_2$ glass, for understanding of the similar decrease of BP intensity in rigid glasses. As shown in Fig. 5.3, a small increase of the power exponent s is also observed when the glass crytallizes into the α or ϕ phase. The increase will be also caused by the growth of crystalline fragments similar to the α or ϕ phase although it is not significant as that caused by the growth of the β like fragments. All those crystalline fragments are formed by $GeSe_{4/2}$ tetrahedra and hence correspond

to rigid regions according to the constraint theory. We assume that, for the growth of the crystalline fragments, large rigid regions are needed. Such a large rigid region is realized only in rigid glasses according to the rigidity percolation model as illustrated in Fig. 3.9. Furthermore, the constraint theory predicts that excess configurational strains are inherent in the rigid glasses. The configurational stains seem to be good candidates for the driving force of the growth of the rigid regions.

5.3 Conclusions

The structural changes of $GeSe_2$ glass are investigated focusing on the low-frequency vibrations. Using the fracton model, we show that a significant change of the low-frequency vibration corresponds to an anomalous increase of the spectral dimensionality $\tilde{d}$ which is a parameter describing the localization degree of the vibration. The anomalous increase suggests a growth of a highly anisotropic structure. We attribute the anisotropic structure to the layered fragments similar to the β crystal on the basis of the experimental result that the significant change of the low-frequency vibrations is always followed by the crystallization of the β or the α+β mixture phase. Moreover, we find a correlation between the low-frequency dynamics and the growth rate of the β crystal; the anomalous increase of $\tilde{d}$ always leads to the saturation of growth of the Raman peak of the β phase during the crystallization. We suggest that the saturation is due to an excessive growth of the β like fragments in a nanoscopic (medium range) scale.

The changes of low-frequency vibrations observed generally in rigid glasses are explained in the similar way to that in $GeSe_2$ glass; the growth of rigid regions formed by $GeSe_{4/2}$ tetrahedra leads to an ordering to decrease the localization degree of the low-frequency vibration, which decreases the BP intensity.

Chapter 6

Investigation of structural variations with composition in Ge_xSe_{1-x} glasses by resonant Raman scattering

In Chap. 3, we have explained the composition dependence of the relaxational modes appearing around T_g in terms of the structural variation of the glassy network; with increasing Ge content, the number of the responsible structures or Se_n ($n > 2$) segments decreases. In this chapter, we trace the structural variation focusing on their electronic structures by resonant Raman scattering. Since, in Ge–Se system, the electronic states in the band-tail region are fairly localized; we can investigate the local structures by measuring the Raman scattering from phonons resonating with the localized electronic states.

6.1 Introduction

The electronic structures of Ge_xSe_{1-x} glasses have been investigated by means of inverse and normal photoemission spectroscopies [26]. Although the spectroscopies are the prove of the local electronic states abrupt changes with composition has been observed in the spectra at the threshold composition predicted by the mean-field constraint theory. This result suggests that local structures should also change at the threshold composition. However, it is not clear how the local structures vary.

Resonant Raman scattering is a powerful tool for studying the local structures and the local electronic states in the band tail region. Since Raman scattering by vibrations in semiconductors and insulators is mediated by electronic (excitonic) transitions, the resonance of lights with the transition enhance the Raman intensity (see, Appendix A.1.2). The intensity dependence with laser energy can hence be used to gain information on the electronic structures. In case of resonance with a localized electronic states, we can also gain the information on the local structures through the enhancement of characteristic vibrational modes.

6.2 Experimental

Raman spectra of Ge_xSe_{1-x} glasses ($x = 0.05 - 0.36$) have been studied at RT as a function of the incident photon energy (1.5 eV–2.6 eV). The experimental setup for Raman scattering is the same as that of Section 3.2. Raman scattering was measured in a backscattering configuration, excited by a DCM dye laser (1.83 eV) or an Ar^+ ion laser (Spectra-Physics Stabilite 2017). It is noteworthy that the effect of photo-darkening that is the red-shift of the optical gap during exposure of light is not significant at room temperature (that is significant at low temperatures for details, see Chap. 7).

6.3 Results and discussion

6.3.1 Resonant Raman scattering in $GeSe_2$ glass

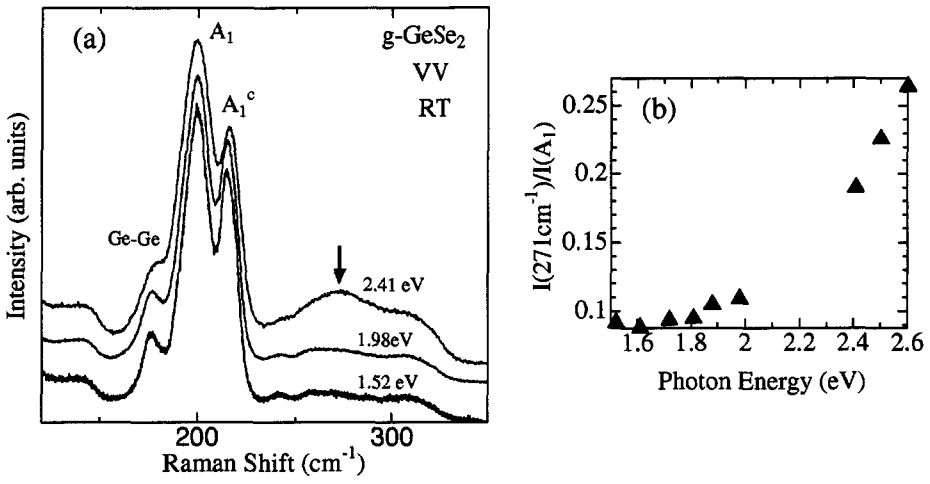

Figure 6.1: (a) Resonant Raman spectra of $GeSe_2$ glass (g–$GeSe_2$), taken in the VV configuration at some various excitation energies. The spectra are normalized to the intensity of the A_1 mode at 200 cm^{-1}. (b) Intensity ratio of 271 cm^{-1} mode to A_1 mode with varying the excitation photon energy from 1.52 eV to 2.60 eV.

First, we show the resonant Raman spectra of stoichiometric $GeSe_2$ glass in Fig. 6.1. The spectra are normalized to the intensity of the A_1 mode of CST increases at 200 cm^{-1}. With increasing the excitation energy, the normalized intensity around 271 cm^{-1} increases. The increase around the optical gap energy (about 2.2 eV at RT) is attributed to the resonance effect. Sample uniformity is comfirmed by measuring the spectra on different sides of a thin sample, as shown Fig. 6.2. No significant difference is observed between the spectra.

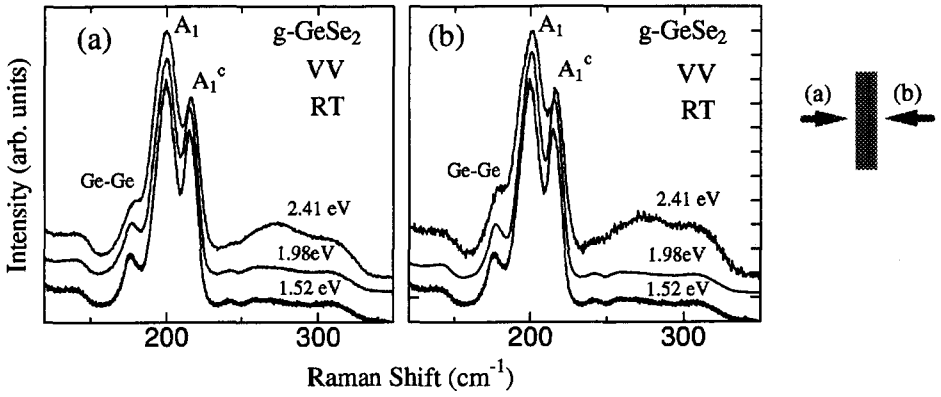

Figure 6.2: Comparison of the Raman spectra of g–$GeSe_2$ measured in the different side of a thin sample, the thickness of which is several hundreds micro meters, as illustrated in the small sketch right of the figures. The excitation energy is varied from 1.52 eV to 2.41 eV; the light penetration depth at 1.52 eV is beyond the sample thickness while that at 2.41 eV is about a few μm.

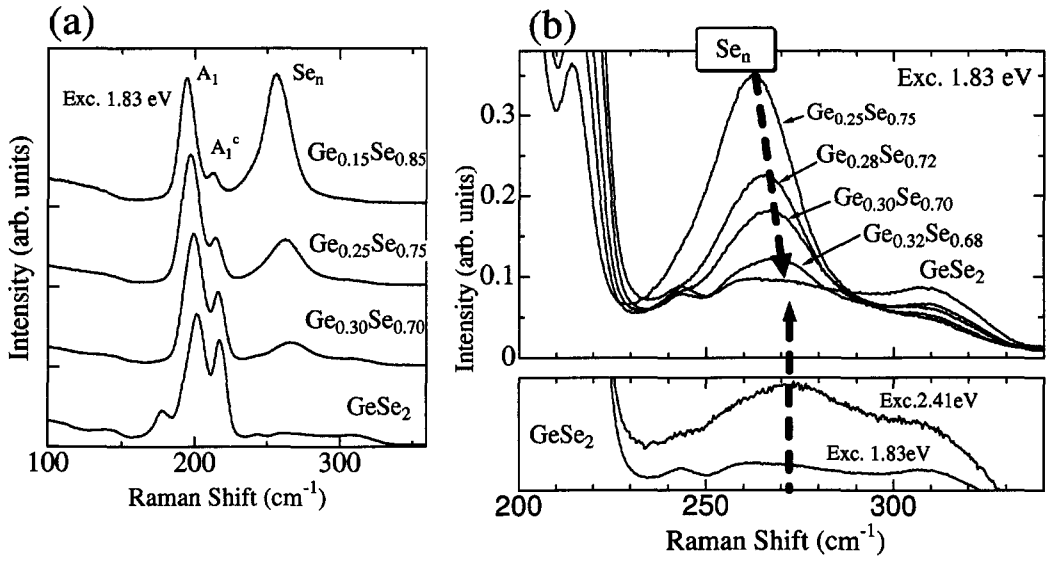

Figure 6.3: (a) Nonresonant Raman spectra of Ge_xSe_{1-x} glasses. (b) Comparison between the expanded view of the nonresonant spectra around Se_n chain mode of Ge_xSe_{1-x} glasses and the resonant spectra of $GeSe_2$ glass.

The resonant mode at 271 cm^{-1} has been assigned to the stretching mode of homopolar Se–Se bonds from its position and a decrease of the intensity by annealing around T_g [55]. To confirm the assignment, we investigate the composition dependence

of the nonresonant Raman spectra, as displayed in Fig. 6.3(a). The peak around 250 cm^{-1} observed in nonresonant Raman spectra of Se-rich glasses is definitely assigned to a strong stretching mode of Se_n chain. With increasing Ge content x, the Se_n chain mode intensity decreases relative to the A_1 mode intensity and the frequency shifts to the high-frequency side. As shown in Fig. 6.3(b), the expected frequency of the Se_n chain (segments) mode of the $GeSe_2$ glass coincides with the frequency of the resonant mode. Thus, the resonant mode is assigned to the stretching mode of Se–Se vibrations.

The Se-Se stretching mode resonates with the electronic transition around the optical gap energy. The resonant electronic states are attributed to Se lone-pair state and antibonding states of the Ge–Se bonds since they form the top of the valence band and the bottom of the conduction band, respectively [63,64,66,67,178]. In this Chapter, we focus on the composition dependence of the resonant Raman scattering.

6.3.2 Resonant Raman scattering in Ge_xSe_{1-x} glasses

Figure 6.4 shows the variation of the resonant Raman spectra with composition. These spectra are normalized to the A_1 mode intensity. Because the optical gaps are between 1.9 eV and 2.3 eV in all the glasses, as shown in Fig. 6.5; our excitation energy range from 1.83 eV to 2.60 eV includes the optical gaps. We plot in Fig. 6.6 the intensity ratio I(Se–Se)/I(A_1) as a function of excitation energy. With increasing excitation energy, the Raman intensity ratio of the Se_n chain mode to the CST mode (A_1) decreases in Se-rich glasses ($0.05 \lesssim x \lesssim 0.18$). There are two possible explanations for the decrease; one is the antiresonance of the Se–Se mode, and the other is the resonance of the CST mode. In the first interpretation, the intensity of the Se–Se mode decreases with increasing excitation energy by antiresonant process (see, Eq. A.11 in Appendix). However, before the excitation energy reaches the resonance energy, the intensity ratio should start to increase. Such an increase is not observed in all the glasses in our wide excitation energy range although the resonance energy is expected in the range. Thus, we attribute the decrease of the I(Se–Se)/I(A_1) ratio to the resonant enhancement of the A_1 mode relative to the Se–Se mode. To confirm this interpretation, we show in Fig. 6.7 (a) the second-order resonant Raman spectra. The second order A_1 mode is increase relative to the first-order one. The second-order resonance without the first-order resonance is only allowed in the crystal with indirect gaps, and hence should not occur in disordered materials. Thus, the second order resonance suggest the resonance of the first order A_1 mode. A small change also observed in the second-order Se–Se modes may suggest a weak resonant enhancement of the Se–Se mode. We conclude that the resonant enhancement of the A_1 mode is much stronger than that of the Se–Se mode in the Se-rich glasses.

With increasing Ge content, the decrease of the intensity ratio becomes small. Then,

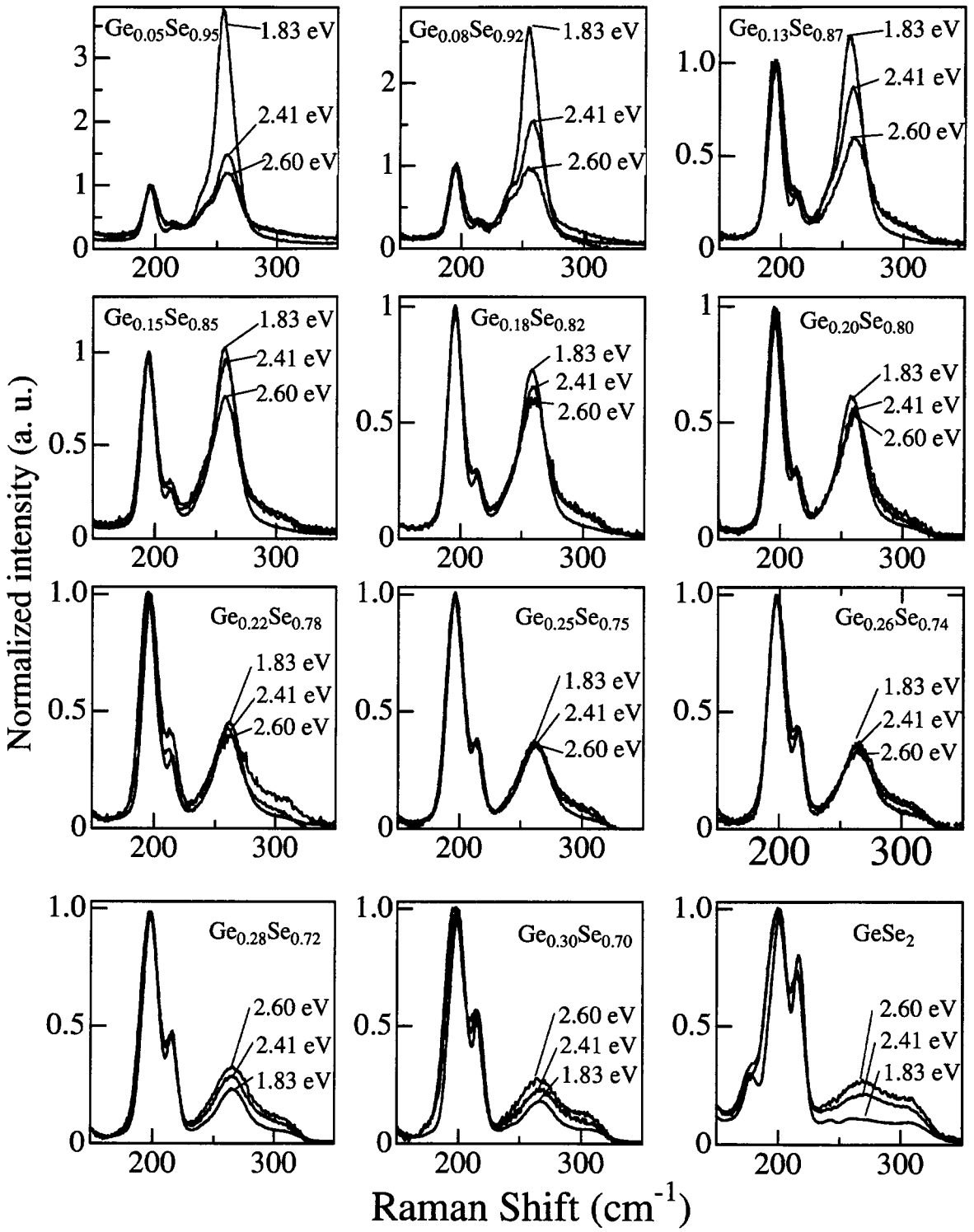

Figure 6.4: Resonant Raman spectra of Ge_xSe_{1-x} glasses. The spectra are normalized to the intensity of the A_1 mode of CST.

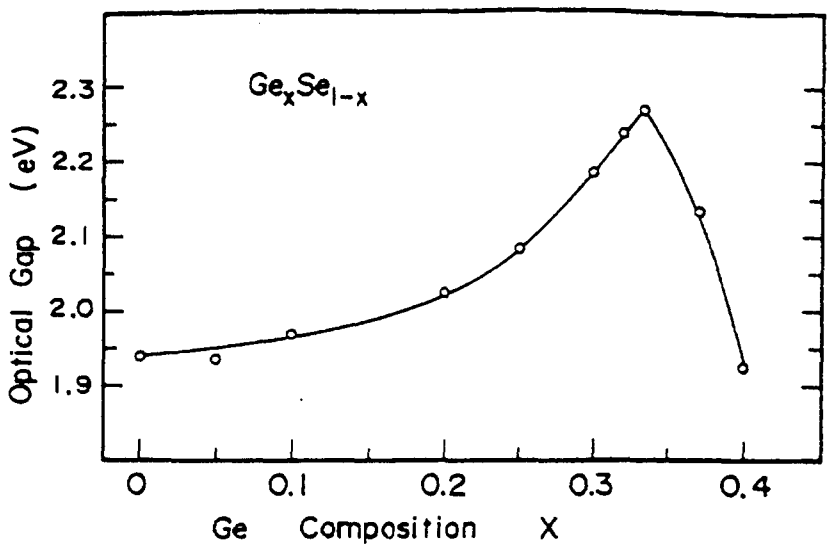

Figure 6.5: Composition dependence of the optical gap at 20°C [179]. The optical gap is defined as the photon energy at which the absorption coefficient takes the value of 10^3 cm^{-1}.

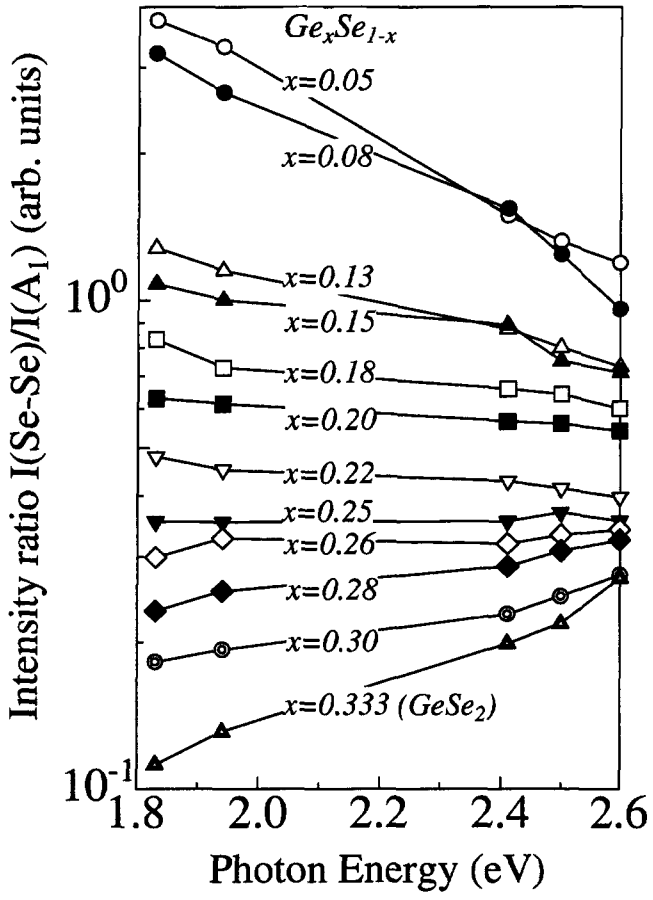

Figure 6.6: Incident photon energy dependence of intensity ratio I(Se–Se)/I(A_1) in semilogarithmic plot for Ge_xSe_{1-x} glasses. The lines are guides to the eye.

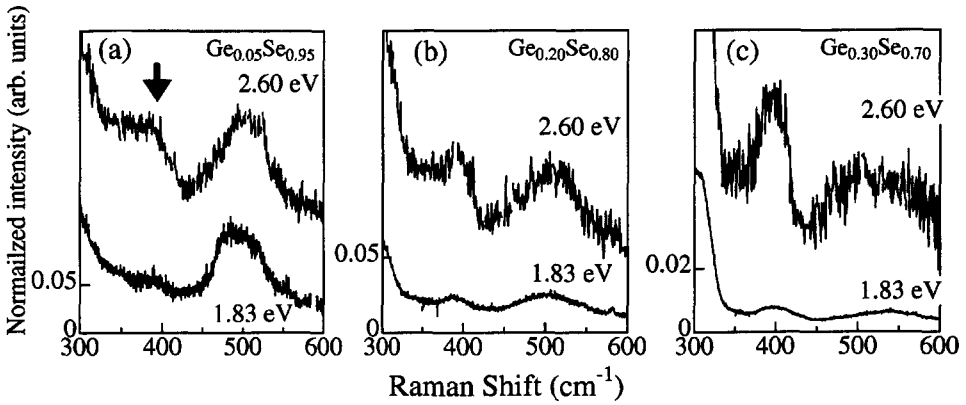

Figure 6.7: Expanded view of the second-order resonant Raman spectra of Ge_xSe_{1-x} glasses [x = 0.05 (a), 0.20 (b), 0.30 (c)]. The spectra are normalized to the intensity of the first-order A_1 mode of CST around 200 cm^{-1}. The second-order resonant peak of the CST mode and that of the Se–Se mode are observed around 400 cm^{-1} and 500 cm^{-1}, respectively.

in the Ge_xSe_{1-x} glasses ($0.20 \lesssim x \lesssim 0.26$), the intensity ratio is nearly independent of the photon energy. As shown in Fig. 6.7(b), the second-order modes of both the Se–Se mode and the A_1 mode increase relative to the first-order A_1 mode. It follows that both the Se–Se mode and the A_1 mode also resonate in the glasses. The independence in the intensity ratio should be due to the same magnitude of the resonant enhancements of the modes.

With further increasing Ge content ($x \gtrsim 0.28$), the intensity ratio increases with excitation energy. As suggested by the resonant enhancements of their second-order modes [Fig. 6.7(c)], both the A_1 and the Se–Se modes resonate. The increase of the intensity ratio should result from the stronger resonant enhancement of the Se–Se mode than that of the A_1 mode.

These observed changes in the Raman intensity ratio are attributed to the resonance effect with the electronic transition between the Se lone-pair states and the antibonding states of the Ge–Se bonds, which form the band-tail states. The resonant band-tail electronic states should be spatially localized around the Ge–Se bonds, namely, the $GeSe_{4/2}$ tetrahedra. Figure 6.8 (a) shows the local structure and vibrational motions around the tetrahedron where the lone-pair electron in the Se atom (shaded circle) is excited to the antibonding state of the Ge–Se bond (shaded bar). We discuss the coupling via electron-phonon interaction between the local resonant electronic-transition

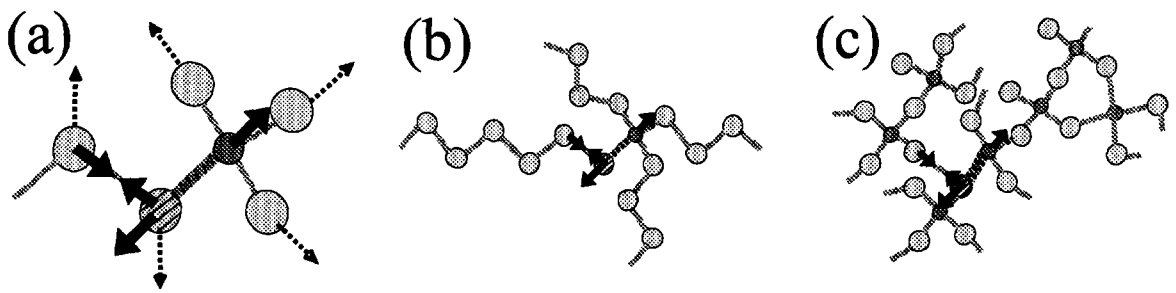

Figure 6.8: (a) Local atomic arrangement around the localized resonant electronic states. Smaller circles denote Ge atoms, and larger ones denote Se atoms. Thin dotted arrows represent schematic atomic motions of stretching modes of the tetrahedron and the Se–Se bonds. Thick solid arrows represent the expected directions to which the atoms tends to move when the lone-pair electron in the Se atom (shaded circle) is excited to the antibonding state of the Ge–Se bond (shaded bar). (b) and (c) are the local structures in Se-rich ($x \ll 0.20$) and Ge-rich glasses ($x \gg 0.20$) with the expected directions, respectively.

and the atomic vibrations, which is formulated as

$$\frac{d\omega_0}{d\xi} = \sum_{i=1}^{N} \frac{\partial \omega_0}{\partial \boldsymbol{u_i}} M_i^{-1/2} \hat{\boldsymbol{e}}_i, \tag{6.1}$$

where ω_0 is the energy of the resonant electronic states, $\partial\omega_0/\partial \boldsymbol{u_i}$ is the electronic-phonon interaction, and $\hat{\boldsymbol{e}}_i$ is eigenvectors of vibration for each atom (see, A.10 in Appendix). It is expected that the photoexcitation of the lone-pair electron weakens locally the repulsive force acting between the lone-pair orbitals of the Se atoms. As a consequence, the Se atoms may tend to approach each other. On the other hand, the photoexcitation of the electron to the antibonding state changes the stable length of the Ge–Se bond; the larger the separation between the Ge and Se atoms, the more stable the photoexcited state in a first approximation. Thus, by the photoexcitation, the atoms should tend to move away. The expected directions of the atomic motions are indicated by thick solid arrows. The direction corresponds to that of $\partial\omega_0/\partial \boldsymbol{u_i}$. We compare it to the directions of the vibrational motions when the tetrahedron and the Se_n chain segment are vibrating independently (molecular approximation), which are shown by thin dotted arrows in Fig. 6.8 (a). One can see that the photoexcitation can couple to both the breathing vibrations of the tetrahedron and the stretching vibrations of the Se–Se segment via the electron-phonon interaction.

We present here a very rough but helpful model to understand the composition dependence of the resonant behaviors. On the basis of Eq. A.5 and Eq. A.7 in Appendix

A.1, we roughly approximate the intensity ratio I(Se–Se)/I(A_1) in nonresonant condition by

$$\frac{I(\text{Se–Se})}{I(A_1)} \propto \frac{\sum \alpha_{Se}}{\sum \alpha_{CST}}, \tag{6.2}$$

where α_{Se} and α_{CST} describe the Raman polarizabilities $\sum_i \frac{\partial \tilde{\boldsymbol{\alpha}}}{\partial \boldsymbol{u_i}}$ for one Se–Se bond and one CST unit, respectively. To discuss broadly the excitation energy dependence of the intensity ratio, we suppose that only the Raman polarizabilities $\alpha_{Se,CST}$ for the Se–Se bond and the CST unit at which the resonant electronic states are localized depend on the excitation energy. In other words, we classify $\alpha_{Se,CST}$ into $\mathrm{NR}_{Se,CST}$ which are independent of excitation energy and $\mathrm{R}_{Se,CST}$ which increase when the excitation energy approaches the resonance energy. We rewrite the intensity ratio I(Se–Se)/I(A_1) as

$$\frac{I(\text{Se–Se})}{I(A_1)} \propto \frac{\sum \mathrm{NR}_{Se} + \sum \mathrm{R}_{Se}}{\sum \mathrm{NR}_{CST} + \sum \mathrm{R}_{CST}}. \tag{6.3}$$

For simplicity, we suppose that the magnitude of the resonance of the Se–Se mode is the same as that of the CST mode:

$$R_{Se,CST} = \begin{cases} \mathrm{NR}_{Se,CST} & \text{(in nonresonant condition)} \\ r \times \mathrm{NR}_{Se,CST} & (r > 1, \text{in resonant condition}). \end{cases} \tag{6.4}$$

Se-rich glasses ($x \ll 0.20$) are composed of mainly Se_n chains and a small amount of tetrahedra, as illustrated in Fig. 6.8 (b). In a glass region which involves $(m+1)$ Se–Se bonds ($m > 0$ in the Se-rich glasses) per one CST unit, the intensity ratio is given as

$$\frac{I(\text{Se–Se})}{I(A_1)} \propto \frac{m\mathrm{NR}_{Se} + \mathrm{R}_{Se}}{\mathrm{R}_{CST}} \tag{6.5}$$

$$= \begin{cases} (m+1)\dfrac{\mathrm{NR}_{Se}}{\mathrm{NR}_{CST}} & \text{(in nonresonant condition)} \\ \dfrac{m+r}{r}\dfrac{\mathrm{NR}_{Se}}{\mathrm{NR}_{CST}} & \text{(in resonant condition).} \end{cases} \tag{6.6}$$

Since $m+1 > \dfrac{m+r}{r}$ $(m > 0, r > 1)$ holds, the intensity ratio I(Se–Se)/I(A_1) decreases when the excitation energy approaches the resonance energy. With increasing Ge content, the average length of the Se_n chains becomes short, and the number of Se–Se bonds per CST units becomes small. In an ideal $Ge_{0.20}Se_{0.80}$ glass [see, Fig. 6.9(b)], there is one Se–Se bond per one neighboring CST unit. Since this case corresponds to $m = 0$ in Eq. 6.6, the intensity ratio becomes independent of the excitation energy at $x = 0.20$. On the other hand, Ge-rich glasses ($x \gg 0.20$) are composed of mainly CST units and a small amount of Se–Se bonds, as illustrated in Fig. 6.8 (c). In a glass region

which involves $(n+1)$ CST units ($n > 0$ in the Ge-rich glasses) per one Se–Se bond, the intensity ratio is given as

$$\frac{I(\text{Se–Se})}{I(A_1)} \propto \frac{\mathrm{R}_{Se}}{n\mathrm{NR}_{CST} + \mathrm{R}_{CST}} \tag{6.7}$$

$$\tag{6.8}$$

$$= \begin{cases} \dfrac{1}{n+1}\dfrac{\mathrm{NR}_{Se}}{\mathrm{NR}_{CST}} & \text{(in nonresonant condition)} \\ \dfrac{r}{n+r}\dfrac{\mathrm{NR}_{Se}}{\mathrm{NR}_{CST}} & \text{(in resonant condition).} \end{cases} \tag{6.9}$$

Since $\dfrac{1}{n+1} < \dfrac{r}{n+r}$ $(n > 0,\ r > 1)$ holds, the intensity ratio I(Se–Se)/I(A_1) increases when the excitation energy approaches the resonance energy.

6.3.3 Relation with rigidity transition

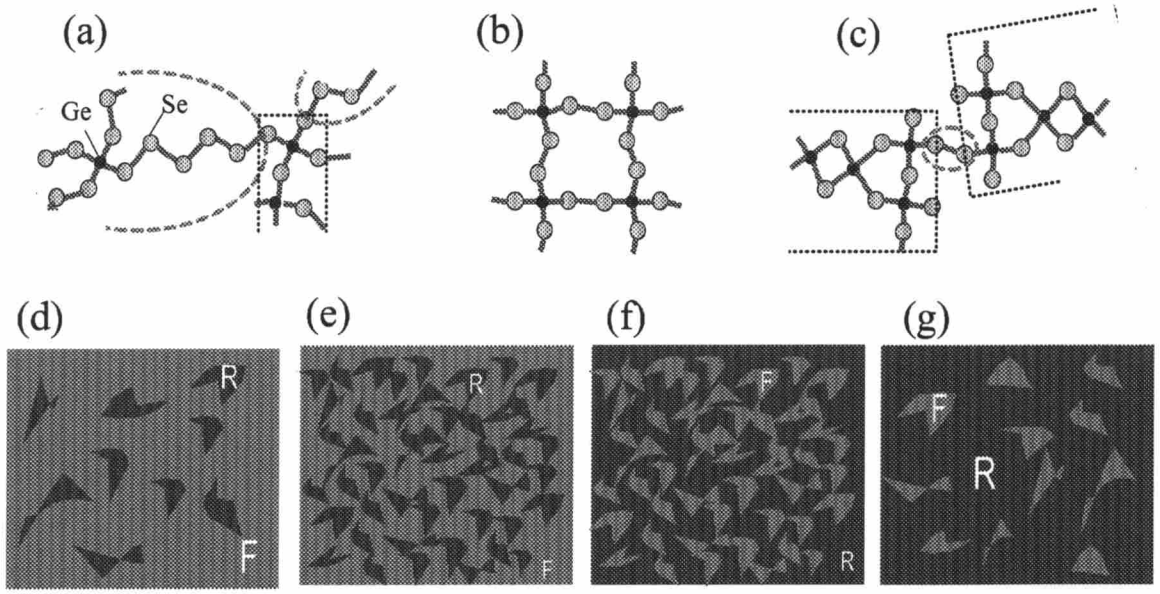

Figure 6.9: Schematic atomic arrangements of local structures in a floppy glass (a), the threshold composition glass (b), and a rigid glass (c). The floppy and rigid regions are bounded by the dashed elliptics rings and dotted open squares, respectively. The floppy (**F**) and rigid (**R**) regions in floppy [(d) and (e)] and rigid [(f) and (g)] glasses are also schematically illustrated.

The structural picture introduced in the model to explain the resonant Raman scattering results is consistent with both the rigidity percolation and the composition

dependence of relaxational modes discussed in Chap. 3. According to Thorpe [3], the Ge–Se system should contain floppy and rigid regions. In floppy glasses, the floppy regions percolate while, in rigid ones, the rigid regions percolate. The $x = 0.20$ composition is the percolation threshold at which the rigidity transition takes place. Se_n chain segments are undercoordinated ($\langle r \rangle = 2$) and comprise the floppy regions while EST units ($\langle r \rangle = 2.67$) are overcoordinated and comprise the rigid regions. CST units play a dual role; such units which cross-link Se_n chain segments are involved in the floppy regions, on the other hand, those which form part of a CST chain or are cross-linked by EST units are involved in the rigid regions, as illustrated in Fig. 6.9(a) and (c). The floppy and rigid regions in the networks are sketched in Fig. 6.9(d)–(g). One can see that, in Se-rich glasses, the floppy regions are much larger than the rigid regions while, in Ge-rich glasses, the reverse is true. When approaching the percolation threshold, the size of the larger region between the floppy and rigid ones becomes small, and the size difference should be minimized at the threshold [$x \sim 0.20$, see, Fig. 6.9(e) and (f)]. Here, we can restate the resonant Raman scattering results as follows. Broadly speaking, between the Se_n and A_1 modes, the mode of the smaller structrual region between the Se_n and CST chains shows the stronger enhancement than the other. Thus, nearly the same resonant enhancement of the two modes in medium composition range ($0.20 \lesssim x \lesssim 0.26$), is consistent with the minimum size-difference at the threshold composition. In view of structural variation, as $\langle r \rangle$ approaches the threshold, both the lengthes of Se and CST chains decrease. Together with the resonant Raman results, we suggest that the floppy and rigid regions should have their minimum sizes around the rigidty threshold.

It is worth mentioning that this structural picture based on the resonant behavior is also consistent with the compositional trend in the relaxational modes. We have attributed the relaxational mode appearing only in the floppy glasses ($x \leq 0.20$) to the rotating Se_n chain segments ($n \geq 3$); it is important to note that the Se_n ($n \leq 2$) segments cannot show the relaxational motions. In Se-rich glasses($x \ll 0.20$), the Se_n chains are long enough ($n \gg 3$). In our picture, with increasing Ge content, Se_n chains are shortened, and have the shortest length ($n = 2$) above the threshold composition, as shown in Fig. 6.9(b). As shown in Chap. 3, the relaxational modes, indeed, do not appear above threshold composition ($x \geq 0.23$).

6.4 Conclusion

We have found systematic changes in the resonant Raman spectra in Ge_xSe_{1-x} glasses. In Se-rich glasses ($0.05 \lesssim x \lesssim 0.18$), the resonant enhancement of the CST mode is stronger than that of the Se chain segments. Around rigidity percolation threshold

composition ($0.20 \lesssim x \lesssim 0.26$), the resonant enhancement is nearly the same between the two modes. In Ge-rich glasses ($x \gtrsim 0.28$), the resonant enhancement of CST mode is enhanced relative to that the Se chain segments. We have assumed that both the stretching mode of Se_n chain and the A_1 mode of CST resonant with electronic states strongly localized around the Ge–Se bond of a tetrahedron. Based on the assumption, we can explain the compositional trend of the resonant behavior, and gives a structural picture for Ge–Se system. This picture is consistent with both the percolation model of floppy and rigid regions and the compositional trend of appearance of relaxational modes.

Chapter 7

Resonant Raman scattering of glassy $GeSe_2$

In this and subsequent chapters, we study photoexcited electronic states toward understanding of photoinduced changes observed widely in chalcogenide glasses. Our aim of this chapter is to extract from resonant Raman study detailed structural information about a photoexcited center and to reveal the microscopic mechanism of the photoinduced changes in a chalcogenide semiconductor $GeSe_2$ glass.

We have observed *excess* resonant Raman enhancement at 15 K, following photodarkening, which is an increase of the absorption coefficient upon illumination, and its reversible change for the excitation power. We will explain both phenomena with the common picture for structural changes, and will discuss the mechanisms.

7.1 Introduction

Various kinds of photoinduced structural changes in chalcogenide glasses are the subjects of considerable interest from both fundamental and practical points of view. The photoinduced structural changes result from the atomic rearrangements which are caused by the energy relaxation of the photoexcited electrons through strong electron-lattice interactions. Despite a great number of the studies [38], the microscopic mechanism responsible for the photoinduced structural changes is still not well understood.

7.1.1 Experimental

We have measured resonant Raman scattering in a backscattering configuration at 15 K, and have traced the changes upon illumination. The experimental setup is displayed in Fig. 7.1. Light sources are a DCM dye laser (1.83 eV) and/or an Ar^+ ion laser (Spectra-Physics Stabilite 2017). The samples have been placed in He gas in a cryostat (Oxford Optistat).

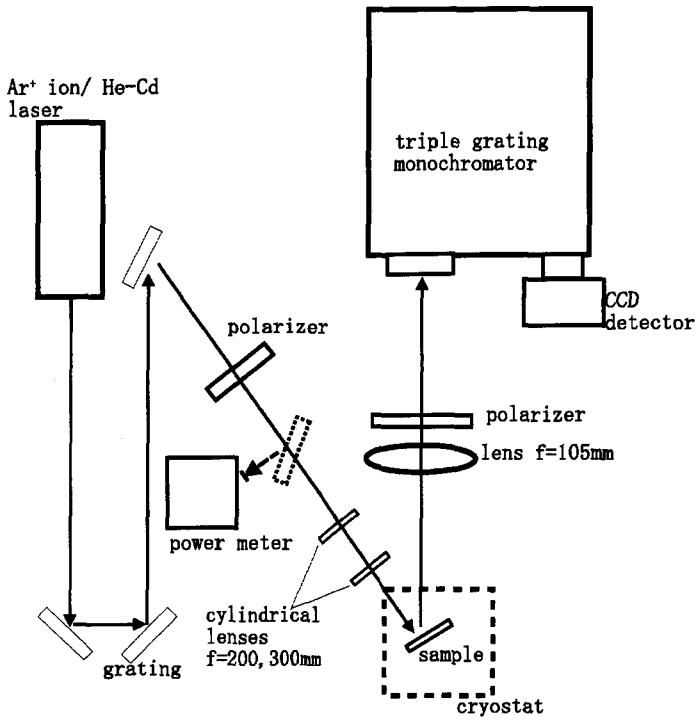

Figure 7.1: Experimental setup for low temperature Raman scattering measurement.

7.2 Results and discussion

7.2.1 Changes in resonant Raman spectra following photo-darkening

Raman spectra of $GeSe_2$ glass at 15 K, excited at 1.81 eV and 2.41 eV are presented in Fig. 7.2. With increasing excitation energy, the stretching vibration of Se–Se mode around 275 cm^{-1} is enhanced relative to the A_1 mode of CST in the similar way as that at room temperature. The inset of Fig. 7.2 shows the excitation energy dependence of the intensity ratio of the Se–Se mode to the A_1 mode, I(Se–Se)/I(A_1). We attribute the enhancement of the I(Se–Se)/I(A_1) ratio around the optical gap of 2.4 eV to the resonance effect with the electronic transition between the Se lone-pair states and the antibonding states of the Ge–Se bonds; the former forms the top of the valence band and the latter forms bottom of the conduction band.

The I(Se–Se)/I(A_1) ratios excited by lights below 2.0 eV are independent of exposure time while those excited by lights around 2.4 eV gradually increase with exposure time, and it saturates after the illumination for about 120 minutes. The exposure of light also increases the I(Ge–Ge)/I(A_1) ratio, and the increase saturates in the same way. Under the illumination the transmitted lights, which we monitor simultaneously, darken

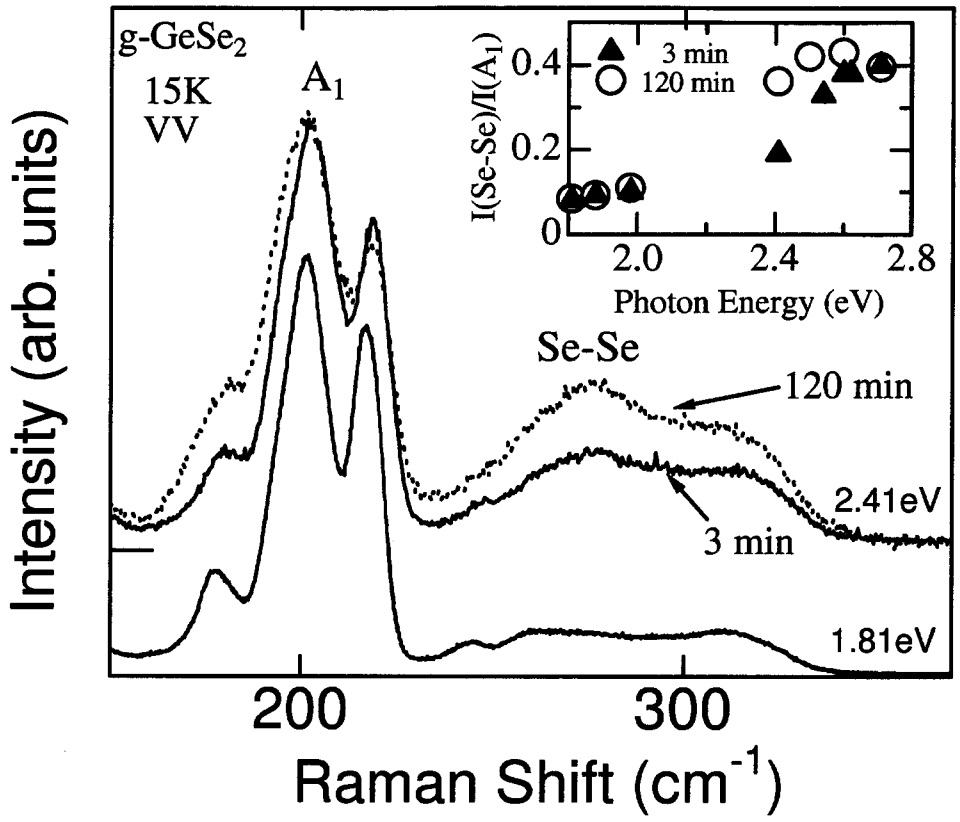

Figure 7.2: Resonant Raman spectra of $GeSe_2$ glass excited at 1.81 eV and 2.41 eV after illuminated for 3 min and 120 min. The power densities are 3 W/cm^2. The spectra are normalized to the intensity of the A_1 mode of CST around 200 cm^{-1}. The inset shows the excitation energy dependence of the intensity ratio of the Se–Se mode to the A_1 mode after illuminated for 3 min and 120 min at each excitation energy.

with exposure time and saturates after about 120 minutes as well. The decrease of the transmitted light intensity is attributed to a red shift of the optical gap, as shown in Fig. 7.3. This phenomenon is termed photodarkening. Obviously, the change of the resonant Raman spectrum with time is closely related to photodarkening. To clarify the relation, we should remove the excitation energy dependence of the efficiency to cause photodarkening. Figure 7.4 shows the comparison of the I(Se–Se)/I(A_1) ratios before and after the photodarkening is induced by a 2.41 eV light. The intensity ratio excited at 2.71 eV is not increased also by 2.41 eV light illumination. Thus, by structural changes following photodarkening, the *excess* resonant electronic states is formed as illustrated in Fig. 7.5; the narrow excess electronic states are formed below 2.7 eV. It should be noted that such an increase with time is observed only at low temperatures, and is hardly observed at room temperature.

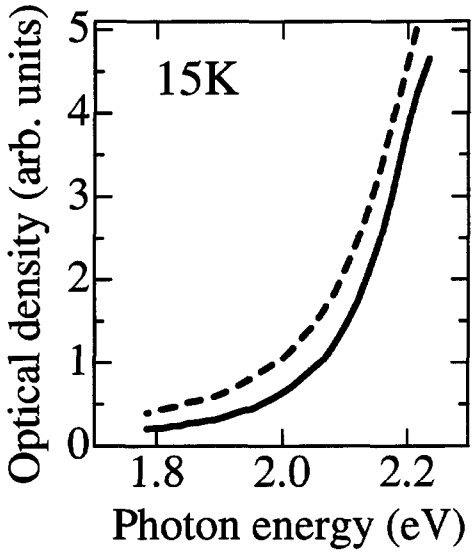

Figure 7.3: Absorption spectra at 15 K before (solid line) and after 2.41 eV light illumination with power density of 0.1 W/cm^2 for 60 min (dashed line). For the details of the experimental setup, see Section 9.2.

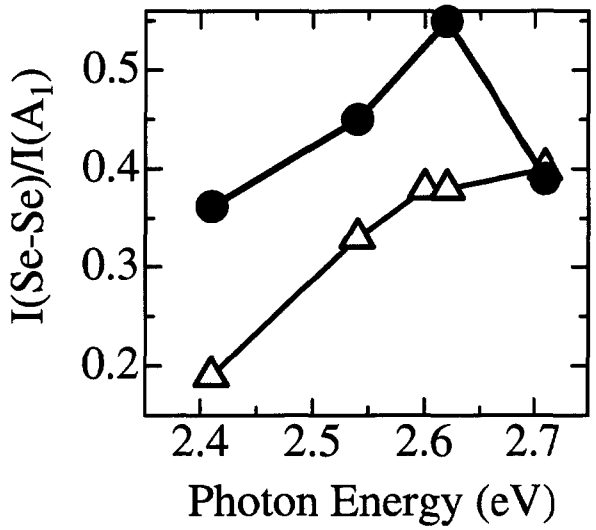

Figure 7.4: Excitation energy dependence of the intensity ratio before (△) and after 2.41 eV light illumination for 120 min (●).

7.2.2 Excitation power dependence

After the 120 min illumination of light at 2.41 eV, we can observe excitation power density dependence in resonant Raman spectra. With increasing the excitation power, the resonantly enhanced intensity ratio I(Se–Se)/I(A_1) decreases, as shown in Fig. 7.6(a). To estimate the heating effect at the excitation power, we display in Figure 7.7 the comparison of the changes in the resonant Raman spectra with temperature and excitation power. Although the resonant Raman spectra is nearly independent of temperature from 15 K to 45 K, the resonant enhancement is reduced with increasing excitation power from 3 W/cm^2 to 9 W/cm^2. Since the increase of the temperature under the 9 W/cm^2 illumination is estimated to be less than 20 K, we conclude that the decrease of the intensity ratio with increase of the excitation power is not due to heating effects but photoinduced effects.

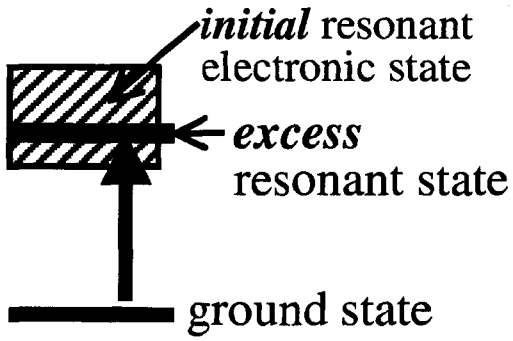

Figure 7.5: Schematic illustration of the *initial* and *excess* resonant state. The initial resonant states exist even in the as-prepared glass, and the excess resonant states are formed by illumination.

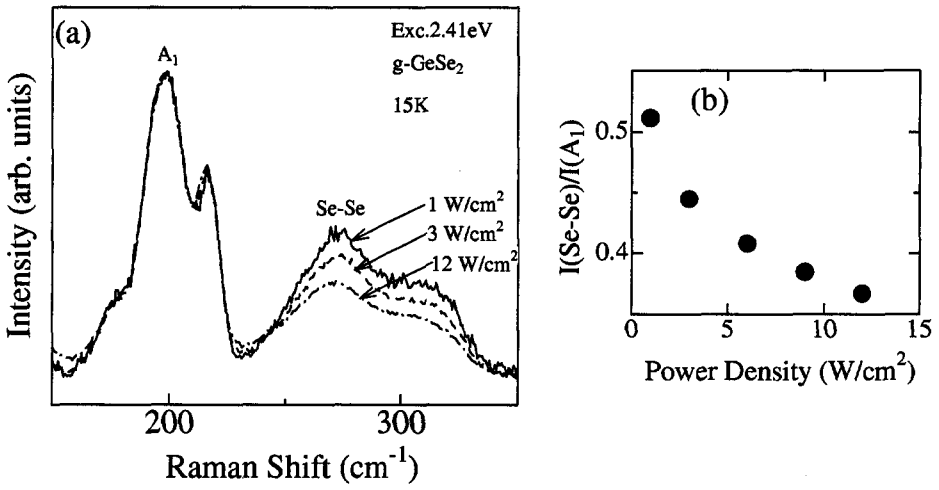

Figure 7.6: (a) Excitation power density dependence of the resonant Raman spectra at 15 K after 120 min exposure of the light of 2.41 eV. The spectra are normalized to the intensity of the A_1 mode. (b) Variation of the intensity ratio I(Se–Se)/I(A_1) with power density. With increasing power density, the intensity ratio rapidly decreases.

In Fig 7.8(a), we present the response of the intensity ratio I(Se–Se)/I(A_1) to a rapid change of the excitation power density of the 2.41 eV light. The response time of the intensity ratio to the power is within a minute. As shown in Fig. 7.8(b), the change with power density is fully reversible. Similar power dependent behavior is observed for the excitations of 2.54 eV and 2.62 eV lights. However, no power dependence is observed at the 2.71 eV excitation. We emphasize that no excess resonant enhancement is observed

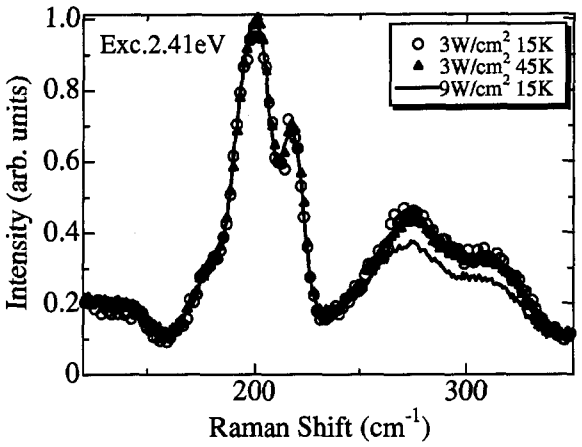

Figure 7.7: Resonant Raman spectra excited at 2.41 eV, normalized to the A_1 mode intensity. Although the spectra is nearly independent of temperature from 15 K to 45 K, the spectra changes when the excitation power is increased from 3 W/cm^2 to 9 W/cm^2.

at the excitation, as displayed in the inset of Fig. 7.2. Thus, the power dependent behavior is closely related to the excess resonant enhancement.

To further investigate the power dependence, we add another light during the Raman measurement using two laser light as depicted in Fig. 7.9(a). After the excess resonant states are formed by a 120 min illumination of 2.41 eV light, we study the effect of simultaneous illumination of 2.41 eV light on the resonant Raman spectra probed by 2.62 and 2.71 eV lights. Fig. 7.9(b) and (c) demonstrate that the resonant enhancement at 2.62 eV is largely decreased by adding 2.41 eV light while that at 2.71 eV light is not. Although the excess resonant states are certainly formed, the resonant spectrum excited at 2.71 eV is not decreased by the illumination. Thus, we find that a higher excitation-power density does not reduce the *initial* resonant enhancement occurring from the beginning (see, Fig. 7.5), but reduces the *excess* resonant enhancement induced by illumination. No reduction of the initial resonant enhancement is consistent with the power dependence of I(Se–Se)/I(A_1) shown in Fig. 7.6(b). The intensity ratio decreases with power, but it does not decrease over a constant value. This is because the *initial* resonant enhancement remains unaltered.

7.2.3 Structural model

Here, we present a structural model to explain the excess resonant enhancement and the excitation power dependence. In chalcogenides glasses, photoinduced creation of pairs of oppositely charged dangling bond defect states have been proposed mainly on

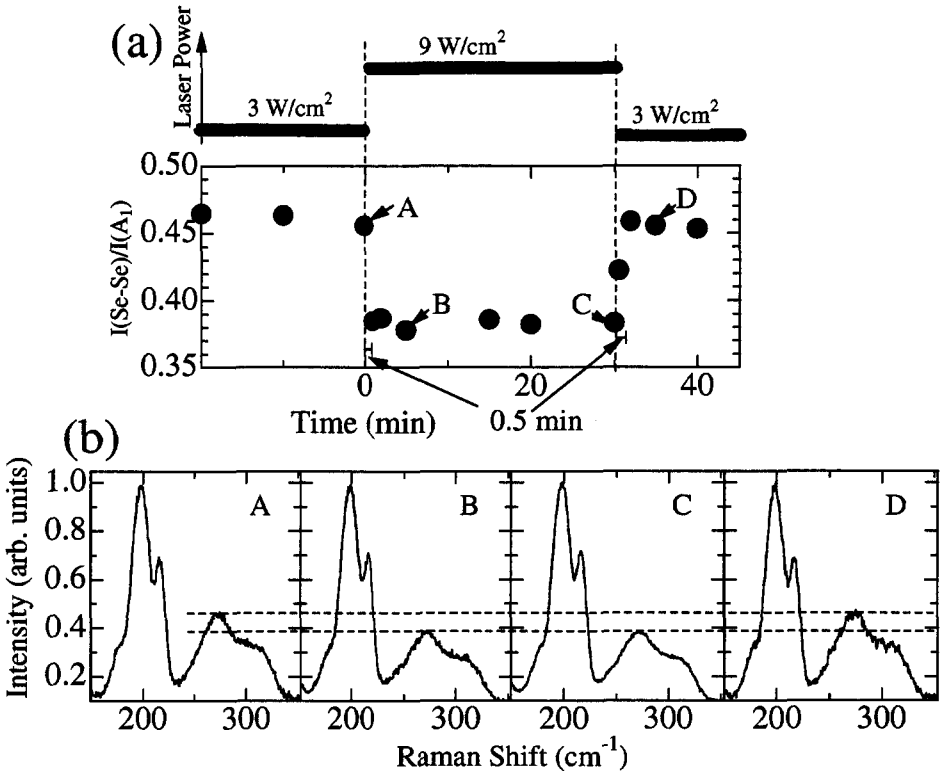

Figure 7.8: (a) Response of the intensity ratio to the power density. The excitation power is switched from 3 W/cm^2 to 9 W/cm^2 at 0 min (corresponding to the time after illuminated for 120 min), and reversed at 30 min. (b) Corresponding resonant Raman spectra at the times denoted in (a). These spectra are normalized to the A_1 mode intensity.

the basis of the observations of photoinduced ESR signals [180,181]. As the origin of the excess resonant states formed just below the optical gap, we propose photoinduced formation of Ge–Ge and Se–Se bonds through the creation of the charged defect pair, as illustrated in Fig. 7.10. We suppose that under the illumination, the charged threefold Ge and Se atoms are temporally formed, as illustrated in Fig. 7.10(b). After switching off the light, the threefold atoms are restored to initial coordinations, but the bonding configuration may be different [Fig. 7.10(c)] due to large lattice relaxation of the excited states; in our model, Ge–Ge and Se–Se bonds are formed through bond switching. This photocreated Ge–Ge and Se–Se bonds will form different electronic states with those of initially existing Ge–Ge and Se–Se bonds since the surrounding conditions are different; for instance, in this model, the Se–Se bond should be formed in the vicinity of the Ge–Ge bond. We suppose that the electronic states of the photoinduced Ge–Ge and Se–Se bonds are expected to be localized in band-tail region and resonate strongly with the

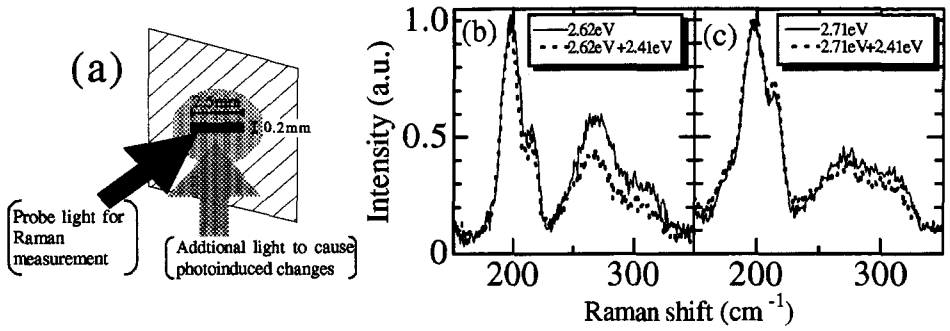

Figure 7.9: (a) Schematic view of the excitation using two laser light; a laser light is added to the probe laser light for Raman measurement. (b) and (c) are the resonant Raman spectra after the illumination of 2.41 eV light for 120 min, excited at 2.62 eV and 2.71 eV lights, respectively, and those under simultaneous illumination with the 2.41 eV light. The spectra are normalized to the intensity of the A_1 mode. When the 2.41 eV light is turned off, the spectrum at 2.62 eV returns to that before the simultaneous illumination.

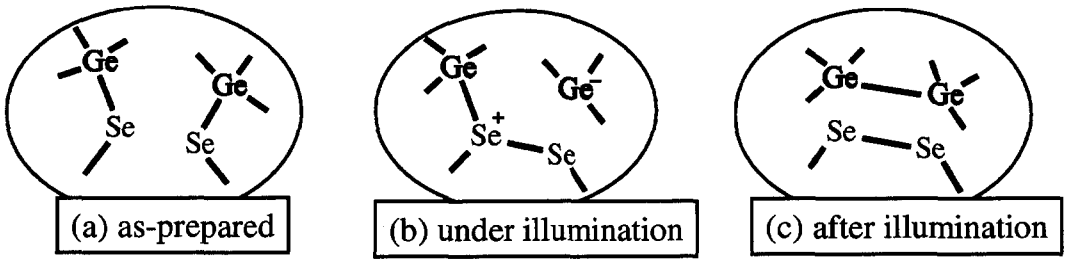

Figure 7.10: Schematic illustration of photoinduced structural changes. (a) Initial (as-prepared) bonding configuration. (b) Transient structure under illumination. Threefold Ge and Se atoms are temporally formed following bond switching. (c) One of new bonding configurations after illumination. Ge–Ge and Se–Se bonds are newly formed following bond switching.

Ge–Ge and Se–Se vibrational modes.

We assume that the photocreated structure with the Ge–Ge and Se–Se bonds can be reversed to a structure with charged threefold Se atoms similar to Fig. 7.10(b) by photo-excitation although after switching off the light most of those will relax to the structure shown in Fig. 7.10(c). To explain the power dependence of the resonant spectrum, we propose that under illumination the charged threefold Se atoms trap photoexcited carriers, and by the trapping, the resonating electronic states of the threefold Se atoms

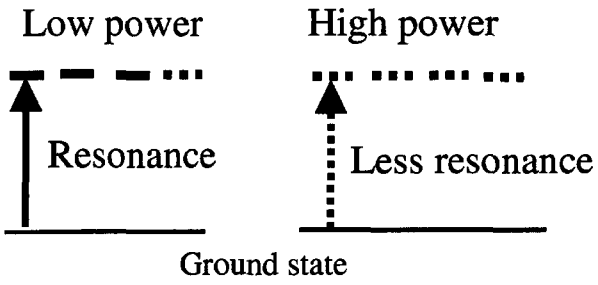

Figure 7.11: Schematic illustration of electronic states under low and high power excitations. The solid and dashed lines represent the resonant and nonresonant electronic states under the illumination, respectively.

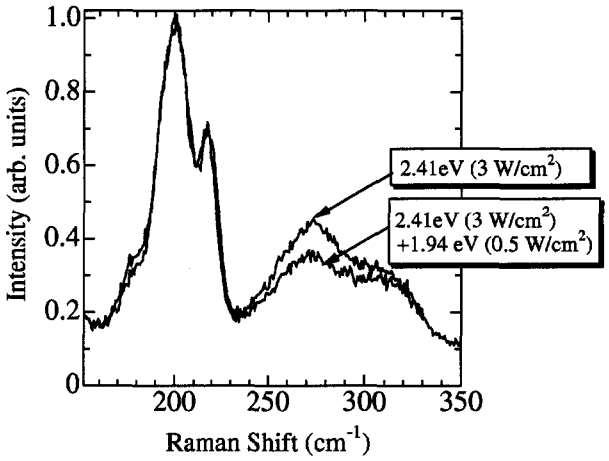

Figure 7.12: Changes in resonant Raman spectra by simultaneously adding the subgap (1.94 eV) light to the probe (2.41 eV) light. The sample has been illuminated by 2.41 eV light for 120 min beforehand.

are transformed to nonresonant states. Moreover, we suppose that relaxations of the nonresonant states to the ground electronic states of the threefold Se atoms are occurring even under the illumination. Under these assumptions, the power dependence is explained as follows. Increasing excitation power increases the number of photoexcited electrons per unit time, and increases the rate of the transition to the nonresonant states by the trapping. If the transition rate to the nonresonant states is much faster than that of the relaxation time to the ground states, the trapping of the photoexcited carriers is no longer possible due to the limitation of the number of the threefold Se atoms. In other words, under the high power excitation, all the electronic states of the threefold

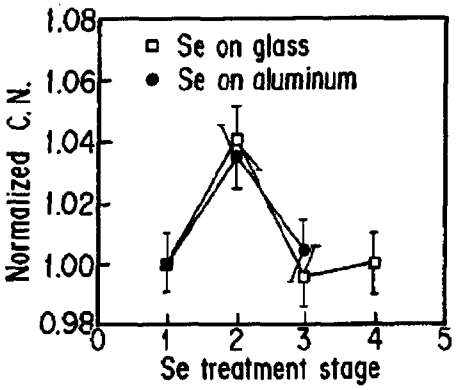

Figure 7.13: The coordination number obtained by the Se K-EXAFS data for amorphous Se deposited on silica glass and aluminum substrates. The coordination number is plotted against the treatment stage (1: as-prepared, 2: under illumination, 3: after illumination, and 4: after heat treatment at 300 K), and normalized to the data for the stage 1. From Ref. [182].

Se atoms are nonresonant, as illustrated in Fig. 7.11. This leads to the decrease of the excess resonant enhancement. Thus, the competition between the photoexcitation leading to nonresonant states and the relaxation into the structure of the ground state causes the power dependence of the resonant spectra. This model of 'trapping' of photoexcited carriers is supported by an experimental result that the decrease of the excess resonant enhancement is also caused by adding a very weak sub-gap light (Fig. 7.12). Although the sub-gap light rarely induces structural changes, trapping of photoexcited carriers occurs efficiently in the band-tail states due to large fluctuations.

The explanation of the power dependence of the resonant enhancement is based on the picture proposed in Fig. 7.10. We emphasize here that the Se–Se bond has already been formed under illumination [Fig. 7.10(b)] while the Ge–Ge bond is formed after illumination [Fig. 7.10(c)]. This picture is consistent with the results that only the Se–Se mode is largely reduced by high power excitation (Fig. 7.6) although both the Ge–Ge and Se–Se modes are enhanced in the excess resonant process (Fig. 7.2).

Since the excess resonant enhancements always follow photodarkening, the origin of the excess resonant states should be the same as that of photodarkening. Recently Kolobov *et al.* have investigated photostructural changes of amorphous Se by EXAFS (extended x-ray absorption fine structure) and Raman measurements [182,183]. They have demonstrated that the average coordination number is increased by illumination, as shown in Fig. 7.13. The light induced change of the coordination is transient; the initial coordination is restored after switching off the light while light induced structural

disorder (local structural transformation) remains. These experimental results strongly support our model of photoinduced transient threefold Se atoms for the excess resonant enhancement.

It is worth mentioning that a similar behavior for light has been observed in another chalcogenide glass As_2Se_3 by light-induced ESR and capacitance measurements [184]. These light-induced signals were annealed out at room temperature. The photoinduced changes with exposure time have two components, fast and slow. In the fast process, the response time of the photoinduced signals when the illumination was turned on and off was within a minute, and the changes were reversible. The slow process having effective relaxation time of 50 min was associated with creation of under- and/or over-coordinated defects. These behaviors of the fast and slow process for illumination is very similar to our results. The behavior of the fast process is similar to the power dependence of resonant enhancement and the slow process is to the formation of excess resonant states. Resonant Raman study for these other chalcogenides should be interesting. The advantage of our resonant Raman study lies in identification of the responsible structure for the photoinduced changes.

7.3 Conclusion

We have found that at 15 K, structural changes by illumination, which cause photodarkening, induce excess resonant enhancement of Ge–Ge and Se–Se mode relative CST mode. After the structural changes are saturated, we can observe a reversible change with the excitation power in resonant Raman spectra. Both of the excess resonant enhancement and the power dependent behavior are explained by temporal formation of threefold coordinated Ge and Se atoms following bond-switching. After switching off the light, the threefold atoms are restored to the initial coordinations, but, at that time, bond-switching occurs to create Ge–Ge and Se–Se bonds, and form the excess resonant states. The power dependence is explained by assuming that trapping of photoexcited carriers in the charged threefold Se atoms transform the excess resonant states to non-resonant ones. The newly observed photoinduced changes in resonant Raman spectra is consistent with recent works of other chalcogenide semiconductors and it will be advantageous to understanding the dynamics of the photoexcited states.

Chapter 8

Resonant Raman scattering of crystalline $GeSe_2$

In this and next chapter, we discuss the electronic structure and electron-phonon interaction in layered crystalline $GeSe_2$ (β–$GeSe_2$, the high-temperature form), and for convenience; we use c–$GeSe_2$ to denote it. Chapter 4 and 5 have suggested that $GeSe_2$ glass involves fragments topologically similar to the layered crystal. The information on the electronic structure and the electron-phonon interaction in the crystalline state is necessary to understand the photoinduced structural changes in the glassy states. Especially, we focus our attention to the structure and the relaxation process of the localized exciton, and study them by resonant Raman scattering and time resolved photoluminescence (PL). Due to strong electron-phonon interaction, the PL of c–$GeSe_2$, exhibits a large Stokes shift; the PL follows large relaxation of the photoexcited states. We investigate the initial state of the relaxation, or the exciton state, by resonant Raman scattering and the final state of the relaxation, or the luminescent state, by time-resolved PL.

8.1 Structure and vibrational properties of c–$GeSe_2$

The crystal structure of c–$GeSe_2$ is monoclinic ($P2_1/c$) with two layers per unit cell [73]. The twofold axis lies on the $\boldsymbol{a}$–$\boldsymbol{b}$ layer plane along crystallographic axis y, where $C_2^y \parallel \boldsymbol{b}$. One layer of c–$GeSe_2$ consists of parallel chains of corner-sharing $GeSe_{4/2}$ tetrahedra (CST), interconnected by pairs of edge-sharing tetrahedra (EST) as shown in Fig. 8.1.

The vibrational properties of c–$GeSe_2$ have already been investigated through infrared and Raman scattering spectroscopy [59–61,72,75,76]. Factor group analysis predicts 36 A_g + 36 B_g Raman-active modes in 144 phonon branches (72 Raman active, 69 IR active and 3 acoustic) made by the 48 atoms per unit cell. The A_g modes are observed for parallel (xx, yy, zz) and crossed (xz) polarizations while the B_g modes are observed for crossed polarizations (xy, yz). However, because of the complexity of the structure, the full assignments of the expected phonons have not been completed yet. Inoue *et al.* have assigned the Raman bands A at 211 cm^{-1} (the most intense peak) to in-phase breathing vibrations extended along the chain of CST, and A^* at 216 cm^{-1} to in-phase breathing vibrations quasi-localized at the EST by using a valence force field model combined with a bond polarizability model (VFF-BP, see Sec. A.1.1

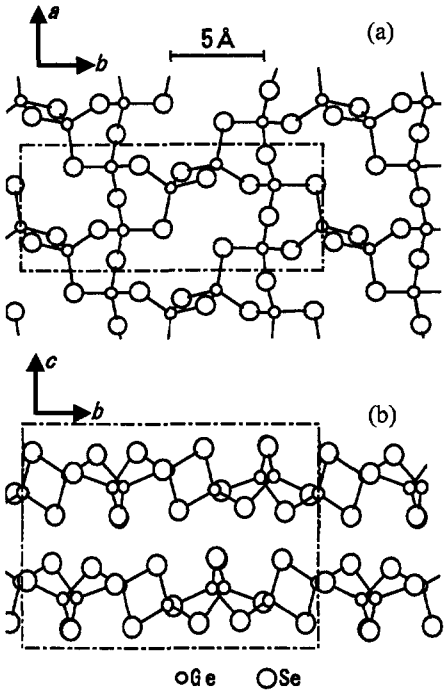

Figure 8.1: Projections of the structure of c-$GeSe_2$ (a) parallel and (b) perpendicular to the layer planes. The unit-cell is bounded by a dashed-and-dotted line.

in Appendix) [59–61].

In the $c(a,a)\bar{c}$ configuration, the A^* band is normally much weaker than the A band, but it becomes stronger than the A band at 2.71 eV excitation. This phenomenon has been ascribed to the resonance effect related to an exciton transition [58]. The exciton transition was observed in the absorption spectra of $\boldsymbol{E} \parallel \boldsymbol{a}$ near 2.7 eV at room temperature (RT) [79]. Although this exciton peak has been assigned to the transition from the 4p lone-pair states of Se atoms to the s-like antibonding states of Ge-Se bonds, the details about the exciton structure are not yet clear. In this chapter, we propose a structural model of the localized exciton by examining the relation between the resonant behaviors of the Raman modes and the calculated atomic motions in the vibrational modes.

8.2 Experimental

Single $GeSe_2$ crystals were prepared by a vapor phase growth method from melt-quenched $GeSe_2$ bulk glasses. The bulk glasses were sealed in an evacuated fused-silica ampoule in vacuum of $\sim 10^{-6}$ Torr. The ampoule had been kept at 680°C with a tem-

perature gradient of about 0.1°C/cm for two weeks. The natural cleavage (001) surfaces were used for Raman measurement.

Raman scattering was measured in the back scattering configuration. The setup is the same as shown in Section 7.1.1. Light sources in an energy range of 2.41– 2.81 eV were an Ar^+ ion laser (Spectra-Physics Stabilite 2017), and a He-Cd laser (Liconix MODEL M.35/7F). The width of the slit was 50 μm and the spectral resolution was about 1 cm^{-1}. The incident light with the power less then 15 mW is focused onto a rectangular region of about 5 mm × 0.1 mm (line-focusing).

The samples were placed in He gas at 15 K in a cryostat, or in a regular flow of Ar gas at room temperature to avoid the influence of rotational modes in a low energy region due to mainly N_2 molecules.

8.3 Results and discussion

8.3.1 Nonresonant Raman spectra

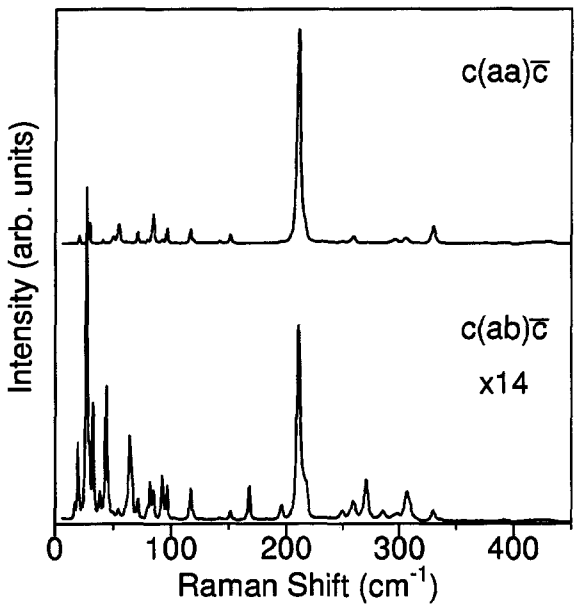

Figure 8.2: An overview of the Raman spectra of c-$GeSe_2$ at RT by 2.41 eV excitation.

An overview of the Raman spectra of c–$GeSe_2$ excited at 2.41 eV, taken in the $c(a,a)\bar{c}$ and $c(a,b)\bar{c}$ (corresponding to A_g and B_g, respectively) geometries, at RT are presented in Fig. 8.2. At this excitation energy, resonant effect is negligible since the exciton energy is about 2.7 eV at RT. In the very low-frequency region, there appear "rigid layer" (RL) modes [77,78] where the two layers in the unit cell relatively vibrate

as rigid units. The RL modes are the partner of vibrational Davydov splittings of the acoustic modes, originating from the breaking of the diperiodic symmetry of the individual layer due to the existence of a weak interlayer interaction. In principle, three RL modes are expected in c–$GeSe_2$: one compressional RL mode (B_g symmetry) in which adjacent layers beat against each other in oppositely directed motions normal to the layer plane, and two shear RL modes (A_g and B_g symmetries) in which adjacent layers slide over each other in oppositely directed motions parallel to the layer planes. However, due to complexity of the crystalline structure, the RL modes lying in higher frequency can admix with low-frequency intralayer modes having the same symmetry, and the RL character is reduced. The calculated atomic motions by VFF-BP calculation show that only the lowest frequency mode (16.6 cm^{-1}) has pure RL character. Other RL modes admix with low-frequency modes. The low-frequency modes in the spectral range from 20 cm^{-1} to 180 cm^{-1} are identified as the bond-bending vibrations which are the translational, rotational, E and lower F_2 motions of the $GeSe_{4/2}$ tetrahedra.

The modes lying from 180 cm^{-1} to 350 cm^{-1} are identified as the bond-stretching vibrations which are the A_1 and the higher F_2 motions of the tetrahedra. The Raman peaks above 350 cm^{-1} arise from multiphonon processes.

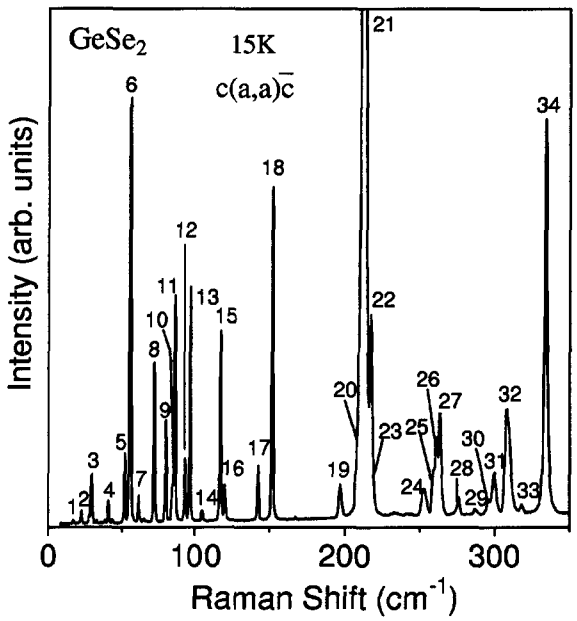

Figure 8.3: Raman spectra of c-$GeSe_2$ at 15K by 2.41 eV excitation. The observed Raman peaks are numbered from a low energy side.

We restrict our discussion on A_g modes, and resolve them by the low-temperature Raman measurement at 15 K. Since the linewidths of the Raman peaks are narrower

than those at RT, some peaks were observed or resolved only at low temperatures as shown in Fig. 8.3. Table 8.1 lists the frequencies of 34 A_g modes in 36 A_g modes predicted from the group theory. The two missing modes probably have intensites below the noise level of our measurements. The peak position of peak number 20, denoted as $P20$, is not clear because of the high intensity of the next peak ($P21$). The peak position of $P23$ (A^* mode) at 15 K is also not clear due to the low intensity in the nonresonant condition [56] Since the resonance energy shifts above 2.81 eV at 15K, an ultraviolet Raman measurement is needed to trace the resonant behavior.

8.3.2 Resonant enhancement of first-order Raman modes

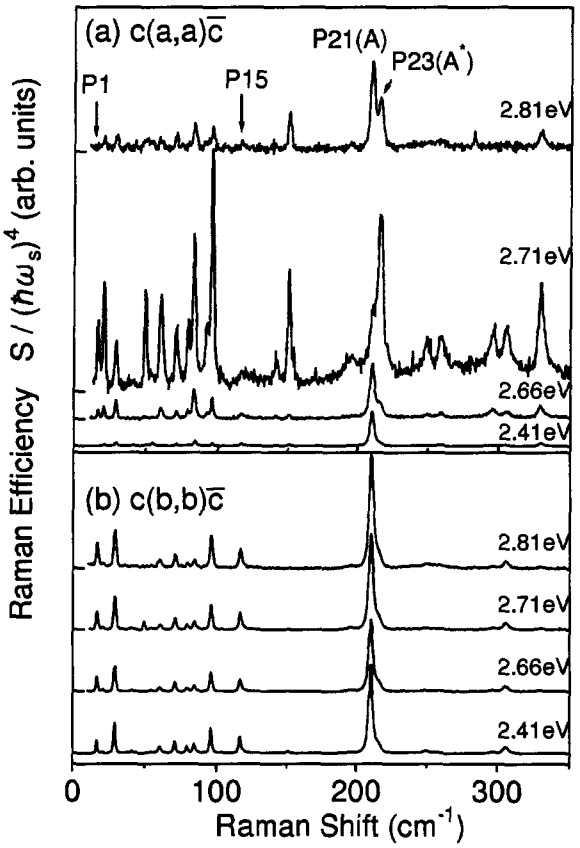

Figure 8.4: Resonant Raman spectra at RT in (a) the $c(a,a)\bar{c}$ and (b) the $c(b,b)\bar{c}$ configurations. The excitation energy is varied from 2.41 eV to 2.81 eV. The spectra are normalized to show Raman efficiency S / $(\hbar\omega_s)^4$, where S is the Raman cross section and $\hbar\omega_s$ is the scattering photon energy. They are displaced vertically for display purposes.

In backscattering configuration, Raman cross section S is obtained by the following

Table 8.1: Frequencies (in cm^{-1}) of the modes found in the first-order Raman spectra of c–$GeSe_2$ at 300 K and 15 K.

No. of peaks	300 K	15 K
1	16.6	17.0
2	20.7	22.3
3	29.3	29.4
4		40.7
5	49.6	51.7
6	54.4	55.4
7	60.5	61.3
8	71.3	71.8
9	79.4	79.8
10		84.1
11	83.7	85.8
12	92.5	93.0
13	96.1	96.7
14		104.9
15	116.4	117.0
16		120.0
17	141.6	142.4
18	150.9	151.8
19	195.8	197.1
20		~208
21	210.4	212.3
22		217.2
23	216.2	~219
24	249.3	252.9
25		258.8
26		260.9
27	259.7	263.3
28	272.2	276.0
29		287.0
30		296.0
31	296.2	299.8
32	305.1	308.2
33		318.2
34	329.4	334.1

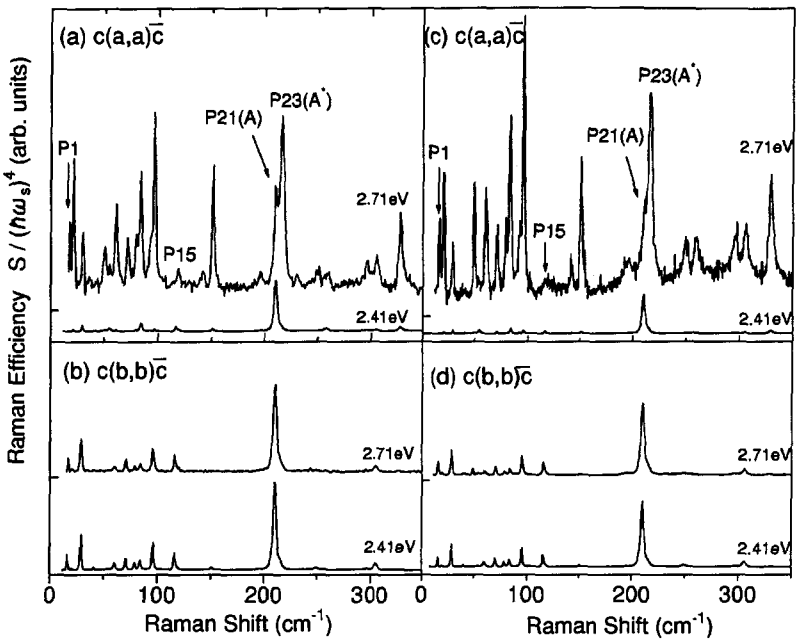

Figure 8.5: Comparison of resonant Raman spectra for two c–$GeSe_2$ grown by different technique: a Bridgman method [(a), (b)] and a vapor phase growth method [(c), (d)]. The spectra are displaced vertically for display purposes.

relation:

$$I_s \propto I_e(1-R_s)(1-R_e)\int_0^D exp[-(\alpha_s+\alpha_e)x]S\ dx, \tag{8.1}$$

where I_s denotes the Raman scattering intensity taking into account the spectral response of the setup, I_e is the incident light intensity, D is the sample thickness or penetration depth of light, R is the reflectivity, and α is the absorption coefficient; the suffix s and e are used for the scattered and incident lights, respectively. The reflectivity is measured for each excitation laser by simply using a photo-diode, and the absorption coefficient is obtained by transmittance measurement (Section 9.2). To show the degree of the resonant enhancement, we plot the ratio $S/(\hbar\omega_s)^4$, where $\hbar\omega_s$ denotes the scattering photon energy, and call the ratio "efficiency" for simplicity. Since S is in general proportional to $(\hbar\omega_s)^4$, this procedure should make the Raman efficiency excitation-independent in the absence of resonant interaction. The obtained excitation energy dependence of the Raman efficiencies for A_g modes in the $c(a,a)\bar{c}$ and the $c(b,b)\bar{c}$ configurations at RT are displayed in Fig. 8.4

In the $c(a,a)\bar{c}$ configuration, the efficiencies of almost all the Raman bands are enhanced around 2.7 eV. However, the enhancements of the $P15$ and $P21$ bands are very small. This selective enhancement suggests the localization of the resonant electronic

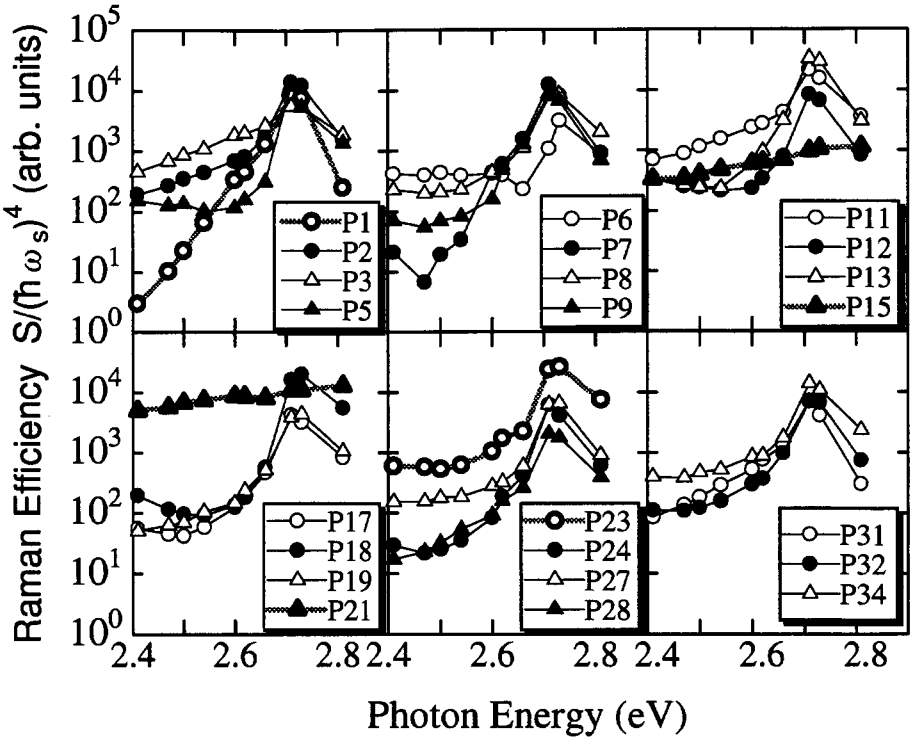

Figure 8.6: Raman efficiencies of the observed A_g modes as a function of incident photon energy. The lines are guides to the eye. We especially focus on four modes whose photon energy dependencies are drawn by the thick gray lines, see the text.

states. On the other hand, in the $c(b,b)\bar{c}$ configuration, the Raman efficiencies are almost independent of excitation energy. These enhancements of the Raman efficiencies are also observed in another samples. No significant difference is observed between resonant Raman spectra for two crystals grown by different technique: a standard Bridgman technique and a vapor phase growth method, as shown in Fig. 8.5. This sample independence confirms that the enhancements are intrinsic phenomena in c–$GeSe_2$.

The variation of the Raman spectra found in the $c(a,a)\bar{c}$ configuration is attributed to the resonance with the localized exciton since both the resonant enhancement and the exciton transition are observed only in the $\boldsymbol{E}\|\boldsymbol{a}$ polarization [79]. The enhancements of the Raman efficiencies are plotted in in Fig. 8.6(a) in logarithmic scale. Almost all the modes in $c(a,a)\bar{c}$ configuration are enhanced around the exciton transition energy of 2.7 eV while the efficiencies of $P15$ and the $P21$ do not show special peaks around 2.7 eV. We emphasize that, among all the observed A_g modes, only the two modes, $P15$ and $P21$, show nonresonant behaviors.

Atomic motions in resonant and Nonresonant modes

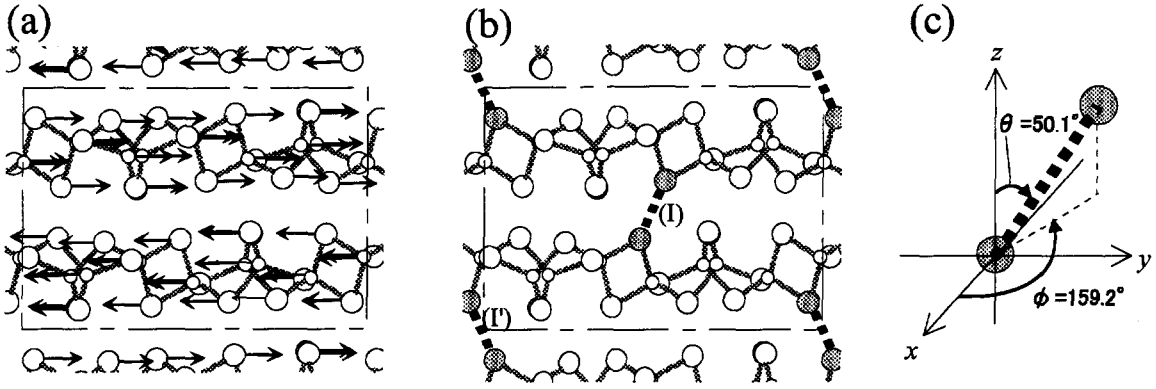

Figure 8.7: Projection of layered structure of c-$GeSe_2$ with (a) the atomic motions in the $P1$ mode and (b) the specific interlayer interactions. Smaller circles denote Ge atoms and larger ones Se atoms. The atomic displacements are calculated on the basis of E-VFF-BP model. Thick dashed lines indicate the strong π-type interlayer interaction between the Se atoms denoted by shaded circles. (c) The direction of the Se-Se interaction labeled (I), specified by two angles: the angle between the Se-Se direction and the crystallographic axis $\boldsymbol{z}$ (θ=50.1°), and the angle between the projection of the interaction to the $\boldsymbol{x}$–$\boldsymbol{y}$ plane and the $\boldsymbol{x}$ axis (ϕ=159.2°). The configuration of the interaction (I') is the same as that of the interaction (I) except the angle ϕ=-159.2°. Note that we use the crystallographic axes: $\boldsymbol{x}\|\boldsymbol{a}$, $\boldsymbol{y}\|\boldsymbol{b}$, and $\boldsymbol{z}$ slightly tilted with respect to the $\boldsymbol{c}$ axis. The monoclinic angle between $\boldsymbol{a}$ and $\boldsymbol{c}$ is β=90.65°.

Let us present the atomic motions in these resonant and nonresonant modes, calculated by E-VFF-BP (extended valence force field and bond polarizability) model [61]. Although the mechanism of the resonant interaction is not directly derived from the BP model, we show that the calculated atomic motions are very useful to understand the essential part of this selective resonant process qualitatively. The atomic motions of the lowest frequency A_g mode ($P1$) are shown in Fig. 8.7(a). All atoms in one layer move in the $\boldsymbol{b}$ direction, and those in the next layer move in the opposite direction. This mode has a pure RL character. Essentially, the RL vibration is caused by interlayer interactions, and not affected by intralayer interactions. Since the RL mode is strongly enhanced at the same energy as the other resonant modes, as shown in Fig. 8.6(a); the interlayer interactions must play an important role in the observed resonant processes. We focus on a specific interlayer interaction, denoted by (I) in Fig. 8.7(b) between the pair of Se atoms whose lone-pair orbitals are exactly parallel to each other. The interacting Se atoms are displaced on neighboring layers across the inversion center.

The distance of the Se atoms is only about 4 Å which is almost equivalent to the second nearest Se-Se distance of $GeSe_{4/2}$ tetrahedra. Large overlap integral of the parallel lone-pair orbitals leads to a strong π-type interlayer interaction between these Se atoms. The direction of the specific interlayer interaction between the Se atoms is shown in Fig. 8.7(c). The angle between directions of the interlayer interaction and the motion of the interacting Se atoms in a vibrational mode determines whether the mode is resonant or not. In the calculated A_g modes, only the two modes have the perpendicular motions of the Se atoms to the interlayer Se-Se direction [Fig. 8.8(a) and (b)]. One of the modes has been assigned decisively to the $P21$ nonresonant mode (the A mode). The other mode can also be assigned to a nonresonant mode ($P15$) because the calculated frequency is nearly the same as that of the $P15$. Thus, both of the two nonresonant modes involve Se motions almost perpendicular to the Se-Se direction. On the other hands, in the resonant modes, the motions of the Se atoms have relatively large fractions of parallel components to the interlayer Se-Se direction. For example, the Se motion of the $P23$ (the A* mode) is almost parallel to the Se-Se direction [Fig. 8.8(c)].

Structural model of exciton

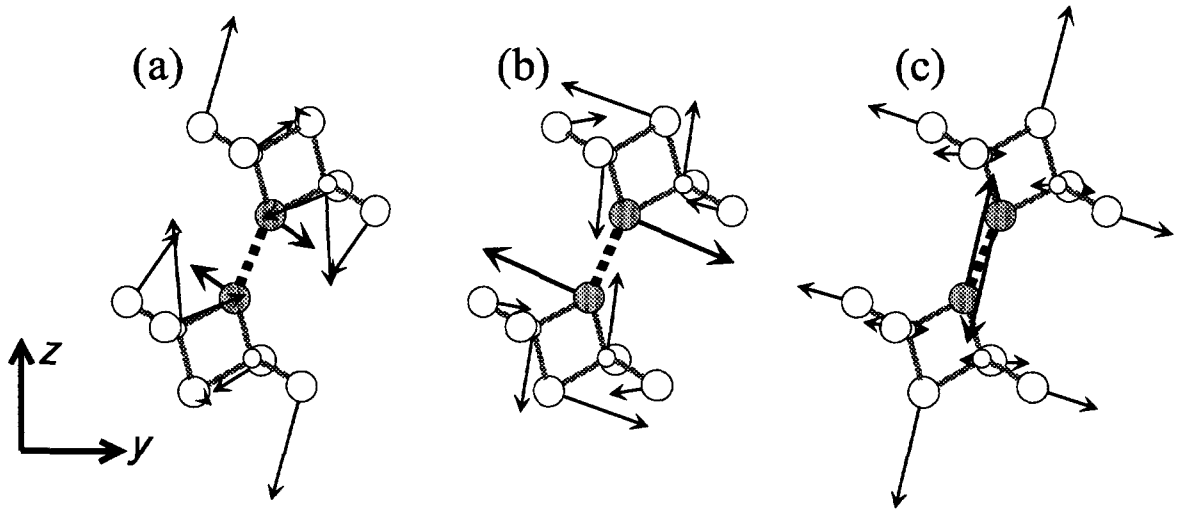

Figure 8.8: Expanded structure of c-$GeSe_2$ around the Se-Se interaction with the calculated atomic motions in (a) the $P21$, (b) the $P15$, and (c) the $P23$ modes. The interacting Se atoms (shaded circles) belong to the EST connecting the chains of CST (see Fig. 1).

We discuss here the exciton structure. The highest-filled states of c–$GeSe_2$ are derived from 4p lone-pair electrons of Se atoms [66]. The parallel lone-pair electrons of

the Se atoms at EST probably have higher energy than those at CST because the Se bonds at EST are under strain [185]. Moreover, the strong π-type interaction between the parallel lone-pair orbitals will cause π-π^* splittings, and the π^* state should be pushed up to form the top of the valence band. It is therefore expected that the hole state of the band-edge exciton arises from the π^* state. Let us assume the excitation of the lone-pair electron from the π^* state to the s-like Ge–Se antibonding state. This excitation causes a decrease in the energy of the π state of the lone-pair electrons with the approach of the interacting Se atoms and, in addition, a decrease in the energy of the Ge–Se antibonding state with an increase of the Ge–Se bond distance. Thus, the excited electron-hole pair interacts with the motion of the Se atoms parallel to the Se–Se direction (cf. Eq. A.10 in Appendix). By such an electron–lattice interaction, the excited electron–hole pair becomes localized to from the band-edge exciton.

This model also explains why the resonant enhancement is observed only in $\boldsymbol{E}\|\boldsymbol{a}$ polarization. Within the dipole approximation, the exciton transition from the lone-pair electron state to the s-like antibonding state requires the light polarized parallel to the lone-pair p orbital almost along the $\boldsymbol{a}$ axis. Thus, the $\boldsymbol{a}$ polarized light interacts resonantly with the localized exciton state coupled with the Se motion to enhance the vibrational modes. Our model for the exciton structure is summarized as follows; (i) the nature of the selective enhancement is the localized exciton; (ii) the exciton is assigned to the transition between the π^* state of the lone-pair electrons to the s-like anti-bonding state of Ge–Se bonds; (iii) the exciton is localized around the particular Se atoms forming the π-type interlayer interaction, and it interacts with the phonons where the motions of the Se atoms have a large fraction of the parallel component to the direction of the Se-Se interlayer interaction.

8.3.3 Multiphonon process

Details of resonant Raman scattering at RT and 15K

The enhancements of second- or higher-order scattering peaks are characteristic feature in resonant Raman scattering. To discuss the enhancements of the multiphonon peaks and the relation with that of the first-order modes, we show the spectra just normalized to the A (nonresonant) mode and divide the spectra into four parts. Roughly speaking, the four parts correspond to the bond-bending region (0–180 cm^{-1}) (a), the bond-stretching region of the A_1 motions of the tetrahedra (180–250 cm^{-1}) (b), the bond-stretching region of the higher F_2 motions of the tetrahedra (250–350 cm^{-1}) (c), and the multiphonon region (350–1000 cm^{-1}) (d). At RT, the multiphonon peaks are enhanced relative to the A ($P21$) mode around the same resonant energy of 2.7 eV as the first-order modes. At 15 K, the resonant energy for the first-order modes shifts above 2.81

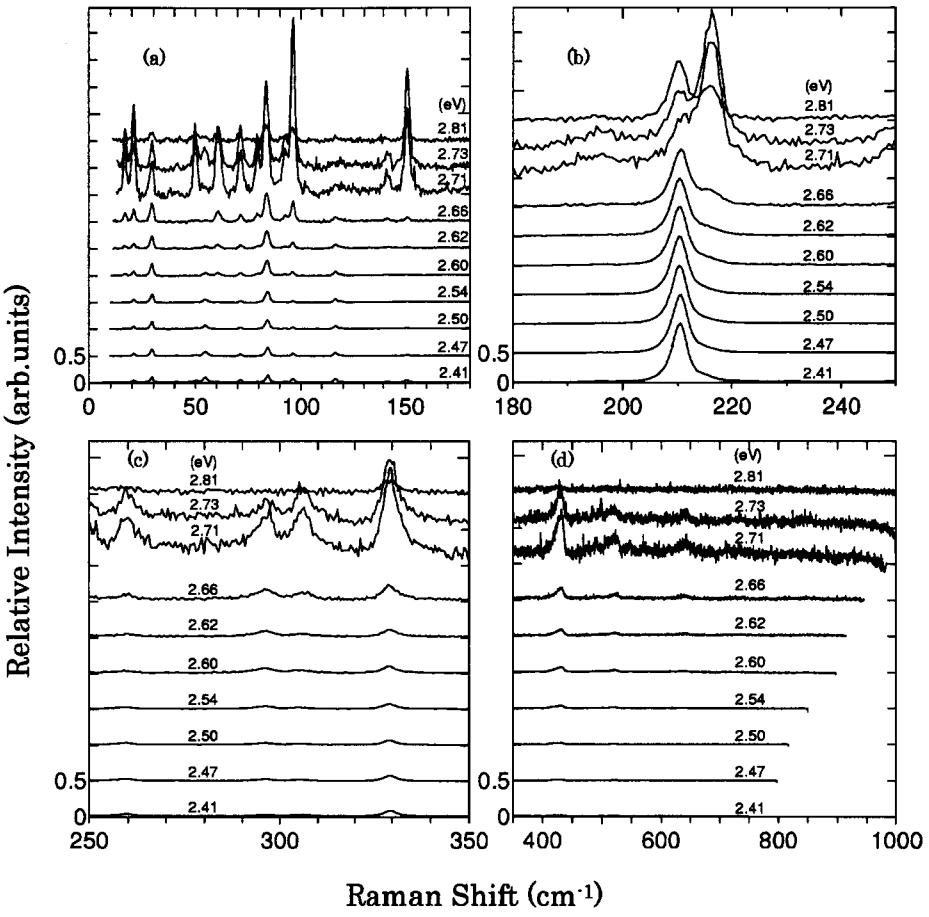

Figure 8.9: Resonant Raman spectra at room temperature taken in the $c(a,a)\bar{c}$ configuration with varying excitation photon energies from 2.41 eV to 2.81 eV. The spectra are normalized to the intensity of the A_1 mode. The spectrum (a), roughly speaking, corresponds to the bond-bending region (0–180 cm^{-1}), (b) to A_1 motions of the $GeSe_{4/2}$ tetrahedra (180–250 cm^{-1}), (c) to higher F_2 motions of the tetrahedra (250–350 cm^{-1}), and (d) to multiphonon processes (350–1000 cm^{-1}).

eV as the band gap energy shifts about ~0.23 eV from that at RT. Although the first-order resonant modes are not enhanced significantly in the excitation energy range, the multiphonon peaks are strongly enhanced. Such a multiphonon enhancement is caused by the resonance with indirect transition. The observation only at low temperatures is due to the sharpening of the electronic levels. At 15 K, some modes in the bond-bending region decrease relative to the A mode around 2.7 eV. This behavior is referred as an "antiresonance" which occurs below the resonance energy as a result of an interference of a a resonant and a nonresonant contributions [186] . The antiresonance is drastic at low temperatures also due to the sharpening of the electronic levels.

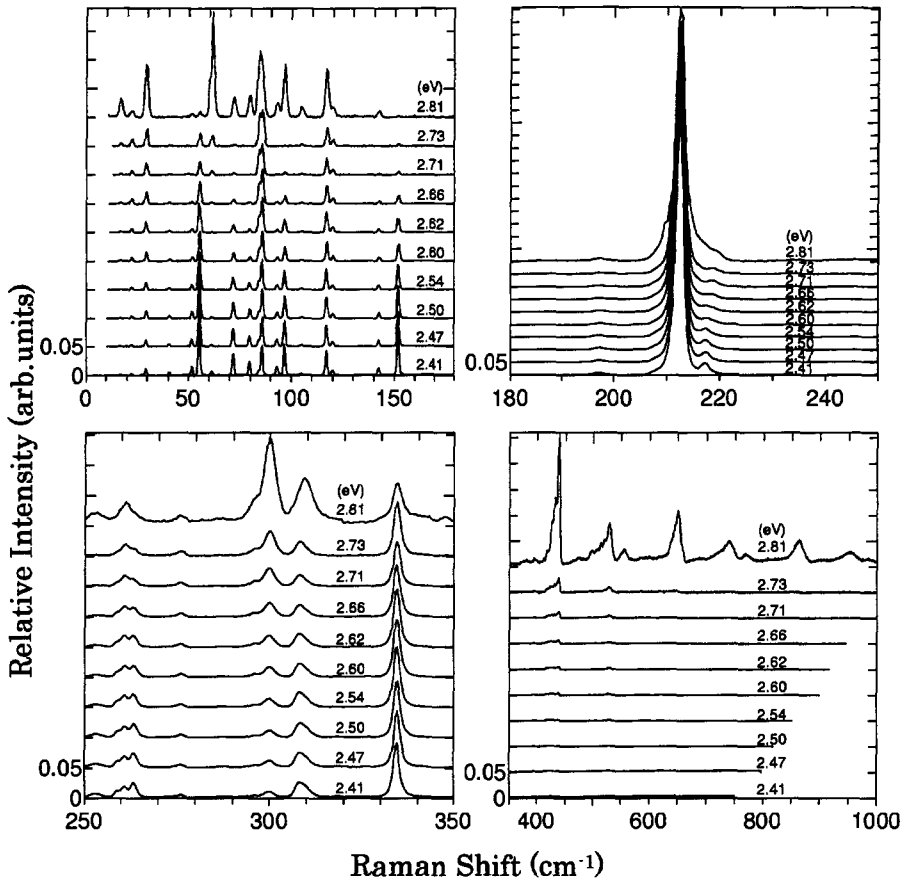

Figure 8.10: Resonant Raman spectra at 15K taken in the $c(a,a)\bar{c}$ configuration.

Selection rules for multiphonon scattering

To assign the multiphonon peaks, we describe here the selection rules for second- or higher-order Stokes Raman scattering. First, we show the law of the conservation of wave vector for first-order Raman scattering:

$$\boldsymbol{k}_s = \boldsymbol{k}_L - \boldsymbol{q}_1, \tag{8.2}$$

where $\boldsymbol{k}_L$ is the wave vector of incident light, $\boldsymbol{k}_s$ is that of scattered light, and $\boldsymbol{q}_1$ is that of a phonon. Since $\boldsymbol{k}_L$, $\boldsymbol{k}_s \ll \boldsymbol{q}_1$, only the scattering for $\boldsymbol{q}_1 \simeq 0$ is allowed. For second order Raman scattering, the sum of the $\boldsymbol{q}$ vectors of the two phonons is zero, i.e.,

$$\boldsymbol{q}_1 + \boldsymbol{q}_2 = 0. \tag{8.3}$$

All phonons in the Brillouin zone can contribute the second-order Raman spectrum; the spectra reflects the two phonon joint density of states. For third-order scattering, it follows that

$$\boldsymbol{q}_1 + \boldsymbol{q}_2 + \boldsymbol{q}_3 = 0. \tag{8.4}$$

If, in the third-order scattering, the two phonons, whose wave vectors are $\boldsymbol{q}_1$ and $\boldsymbol{q}_2$, are contributing also to the second-order scattering; the wave vector of the third phonon, $\boldsymbol{q}_3$, should be zero.

Next, we show the selection rules for the symmetries of phonon modes. The character table of c–$GeSe_2$ is shown in Table 8.2. The A_g and B_g modes are observed in the Raman

Table 8.2: Character table of c–$GeSe_2$. (E: identity operation, S_2: twofold screw operation, i: inversion operation)

	E	S_2	i
A_g	1	1	1
A_u	1	1	-1
B_g	1	-1	1
B_u	1	-1	-1

scattering spectrum, while the A_u and B_u modes are observed in the infrared absorption spectrum. The two phonon Raman process at the Γ point ($\boldsymbol{q}$=0) is allowed when the direct product of the modes contains the A_g or B_g symmetry; the overtones, $A_g \times A_g$, $A_u \times A_u$, $B_g \times B_g$, and $B_u \times B_u$ should be observed in the A_g spectrum, and the combinations, $A_g \times B_g$ and $A_u \times B_u$ should be observed in the B_g spectrum. This selection rule for Γ point of Brillouin zone is also valid for X and Y points because the symmetries of those points are the same as that of the Γ point.

Table 8.3: Frequencies of the first-order A_g, $B_g(\boldsymbol{q} \sim 0)$ at 15 K and those of the A_u, $B_u$modes at RT in 200-220 cm^{-1}. The $r1$, $r2$ are from Ref. [72,75]. The corresponding phonon branches for A_g and B_g modes are denoted as $a1$∼$a5$, and those for the A_u and B_u modes as r1∼r2.

branch number	A_g	B_g
$a1$	∼208	∼208
$a2$	212.3	212.5
$a3$		∼215
$a4$	217.2	217.2
$a5$	∼219	220.0
	A_u	B_u
$r1$		213
$r2$	216	216

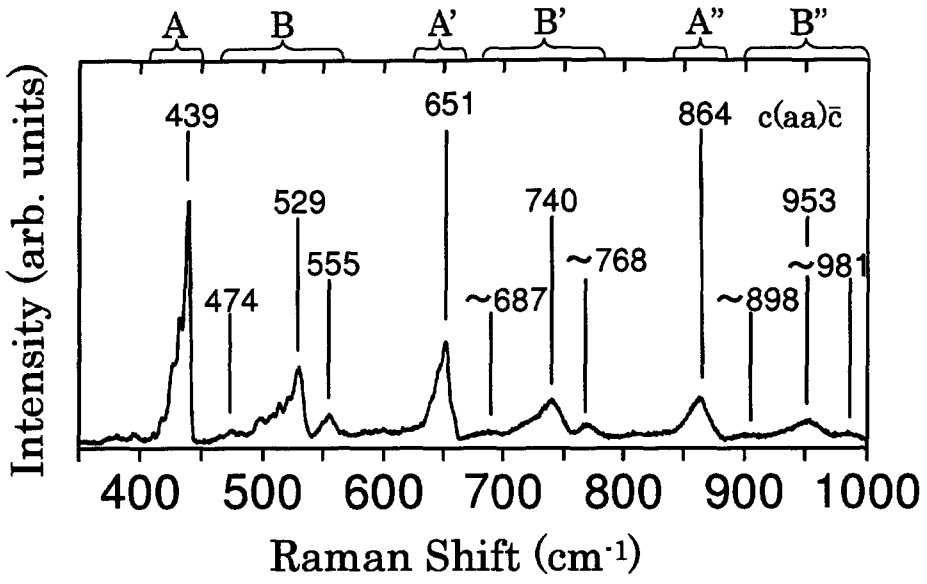

Figure 8.11: Expanded view of the Raman spectra at 15K in the multiphonon region. The spectra are taken in the $c(a,a)\bar{c}$ configuration with excitation energy at 2.81eV. The spectral feature in the **A** region resemble that in the **A'** and **A"** region, and the spectral feature in the B region resemble that in the **B'** and **B"** region.

With these selection rules in mind, we assign the multiphonon peaks observed in resonant Raman spectra shown in Figure 8.11. First, we assign the multiphonon peaks around 400 cm^{-1} (**A** region, denoted above the figure). The candidates for the phonons contributing to the multiphonon peaks are listed in Table 8.3. We use the same label $a1 \sim a5$ for both A_g and B_g modes. This is because we could not unfortunately distingish $A_g \times A_g$ from $B_g \times B_g$ due to the very small energy difference between the A_g and B_g modes. Probably, both modes will contribute to the overtone peak although the $A_g \times A_g$ modes will dominate. The strongly enhanced peak at 439 cm^{-1} can be ascribed to the overtone of the modes in $a5$ branch ($\sim$219 cm^{-1}), based on the frequencies of the candidates and the strong resonance of the A^* mode (the mode with $\boldsymbol{q}\sim 0$ in $a5$ branch). Since the dispersion of the phonon branch corresponding to the A^* mode is very small as shown in Fig. 2.27, all the modes in the $a5$ branch are the candidates. But, this resonance is caused by the indirect transition as confirmed by the strong enhancement of the overtone peak in the absence of the resonance of the A^* peak at 2.81 eV. Thus, the strong peak at 439 cm^{-1} are assigned to the overtone of the phonons in the $a5$ branch with $\boldsymbol{q}\neq 0$. The assignments of other peaks in the **A** region is very difficult because the frequencies of the A_u and B_u modes at 15 K are not clear, and the dispersion curves around 200 cm^{-1} are very complicated.

In the **B** region, three intense multiphonon peaks are observed at 474, 529, and 555 cm^{-1}. Because there are no peaks around the half frequencies of the three peaks, the three peaks should be ascribed to the combinations of different modes. Since the spectral feature around 529 cm^{-1} closely resembles that around 439 cm^{-1}, the strong resonant mode $a5$ will contribute to the three peaks. The candidates for the other Raman modes contributing to the three peaks are shown in Table 8.4. The three

Table 8.4: Frequencies of the first-order A_g, B_g ($\boldsymbol{q}\sim 0$) at 15 K and those of the A_u, B_u modes at RT in 250–350 cm^{-1}. The s1, s2 are from Ref. [72,75]. The corresponding phonon branches for A_g and B_g modes are denoted as $f1\sim f5$, and those for the A_u and B_u modes as $s1\sim s2$.

branch number	A_g	B_g
$f1$	252.9	253.0
$f2$	308.2	309.1
$f3$	334.1	334.2
	A_u	B_u
$s1$	305	306
$s2$	331	334

peaks at 474, 529 and 555 cm^{-1} can be assigned to the combination of the modes in the branches, $a5+f1$, $a5+f2$ and $a5+f3$, respectively, from their energy position. Since these modes resonate with indirect transition, as in the 439 cm^{-1} peak, the contributing mode in the $a5$ branch should have a non-zero wave number. From Eq. 8.3, it follows that the contributing mode in the $f1\sim f3$ also has a non-zero wave number.

Taking a general view of Fig. 8.11, it is found that the spectral features in the **A'** and **A"** regions resemble that in the **A** region, and the spectral features in the **B'** and **B"** regions resemble that in the B region. All the energy difference between the peaks in **A–A'**, **A'–A"**, **B–B'**, and **B'–B"** regions are 211$\sim$213 cm^{-1}. This energy corresponds to that of the A mode which is the mode with $\boldsymbol{q}$=0 in the $a2$ branch. The peaks in the **A'** and **B'** regions are caused by the A mode in addition to the modes forming the peaks in the **A** and **B** regions In the same way, the peaks in the **A'** and **B'** regions are caused by the A mode in addition to the modes forming the peaks in the **A"** and **B"** regions. The zero wave number of the third or the higher order phonon is consistent with the selection rules in Eq. 8.3 and Eq. 8.4. The assignments for the multiphonon peaks are summarized in Table 8.5. Some discrepancies in frequency will be explained by the phonon dispersions.

Table 8.5: The assignments of the peaks in the multiphonon region The a2($\boldsymbol{q}$=0) denotes the mode in the a2 branch with $\boldsymbol{q}$=0 (the A mode).

c(aa)$\bar{c}$	
Frequency (cm^{-1})	assignment
439	$2 \cdot a5$ ($\boldsymbol{q}\neq 0$)
474	$a5$ ($\boldsymbol{q}\neq 0$) + $f1(\boldsymbol{q}\neq 0)$
529	$a5(\boldsymbol{q}\neq 0)$ + $f2(\boldsymbol{q}\neq 0)$
555	$a5(\boldsymbol{q}\neq 0)$ + $f3(\boldsymbol{q}\neq 0)$
651	$2 \cdot a5(\boldsymbol{q}\neq 0)$ + $a2(\boldsymbol{q}=0)$
687	$a5(\boldsymbol{q}\neq 0)$ + $f1(\boldsymbol{q}\neq 0)$ + $a2(\boldsymbol{q}=0)$
740	$a5(\boldsymbol{q}\neq 0)$ + $f2(\boldsymbol{q}\neq 0)$ + $a2(\boldsymbol{q}=0)$
768	$a5(\boldsymbol{q}\neq 0)$ + $f3(\boldsymbol{q}\neq 0)$ + $a2(\boldsymbol{q}=0)$
864	$2 \cdot a5(\boldsymbol{q}\neq 0)$ + $2 \cdot a2(\boldsymbol{q}=0)$
898	$a5(\boldsymbol{q}\neq 0)$ + $f1(\boldsymbol{q}\neq 0)$ + $2 \cdot a2(\boldsymbol{q}=0)$
953	$a5(\boldsymbol{q}\neq 0)$ + $f2(\boldsymbol{q}\neq 0)$ + $2 \cdot a2(\boldsymbol{q}=0)$
981	$a5(\boldsymbol{q}\neq 0)$ + $f3(\boldsymbol{q}\neq 0)$ + $2 \cdot a2(\boldsymbol{q}=0)$

8.4 Conclusions

First, we have observed almost all the Raman-active A_g modes of c–$GeSe_2$ and have investigated the resonant behaviors in a throughout spectral range of the first-order Raman modes. The resonance of the RL mode and the difference of the atomic motions in the resonant and the nonresonant modes suggest the structure of the localized exciton located around the particular pair of Se atoms forming the π-type interlayer interaction.

Next, we have also observed the resonant enhancements of the peaks in the multiphonon region at 15 K and have assigned the peaks from the selection rules. The phonon branch $a5$, in which the zone-center A^* mode strongly resonates in the first order scattering, contributes to all the strong multi-phonon peaks. The third- and forth-order scattering originate from the addition of the zone-center A mode in the $a2$ branch to the modes contributing to the second-order scattering.

Chapter 9

Photoluminescence of crystalline $GeSe_2$

In this chapter, relaxation processes of the photoexcited states in layered crystalline $GeSe_2$ are studied by time-resolved photoluminescence measurement. We resolve two photoluminescence bands, P1 and P2, from their decay kinetics. We show that one of the relaxation pathways to the P2 band arises from a band edge exciton state. We discuss the relaxation process of the exciton on the basis of the luminescence characteristics and the structural model of the exciton proposed in Chap. 8.

9.1 Introduction

Generally, photoluminescence (PL) spectra of chalcogenide semiconductors exhibits a large Stokes shift and a fairly broad linewidth due to their strong electron–lattice interaction. Such interesting PL properties have been the subject of extensive studies [87,187]. A similarity of the PL spectra and time-decays between the crystalline and amorphous forms has been reported in several chalcogenide semiconductors, including As_2Se_3 and $GeSe_2$ [81,187]. This suggests a common relaxation mechanism that arises from the intrinsic chemical bonds rather than native defects or impurities. Toward a general understanding of the relaxation process of the photoexcited states in chalcogenide semiconductors, we have studied the PL properties of a typical chalcogenide semiconductor, layered crystalline $GeSe_2$ (c–$GeSe_2$) which is "a keystone" to investigate those of the Ge–Se glasses [57]. The luminescence properties of crystalline $GeSe_2$ are similar to the layered crystalline As_2Se_3 (c–As_2Se_3) [187]. Ristein *et al.* have proposed, based on the optically detected magnetic resonance (ODMR) measurement [83], that the luminescent center of c–As_2Se_3 is a self-trapped triplet exciton, and the relaxation of the photoexcited states is initiated by trapping of a hole at a center of inversion symmetry lying between layers. Across the inversion center, the lone-pair electrons of two Se atoms strongly interact with each other. Such a local configuration of the initial state of the relaxation in c–As_2Se_3 is very similar to the configuration of a band edge exciton in c–$GeSe_2$. The band edge exciton is quasi-localized to the edge-sharing bi-tetrahedra across the inversion center. As we shall show later, this exciton relaxes to a luminescent state. In this work, we study the luminescence properties by time-resolved measurement, and discuss the electronic and structural relaxation processes of the band

edge exciton, based on the structure proposed in Section 8.3.2.

9.2 Results and discussion: absorption measurement

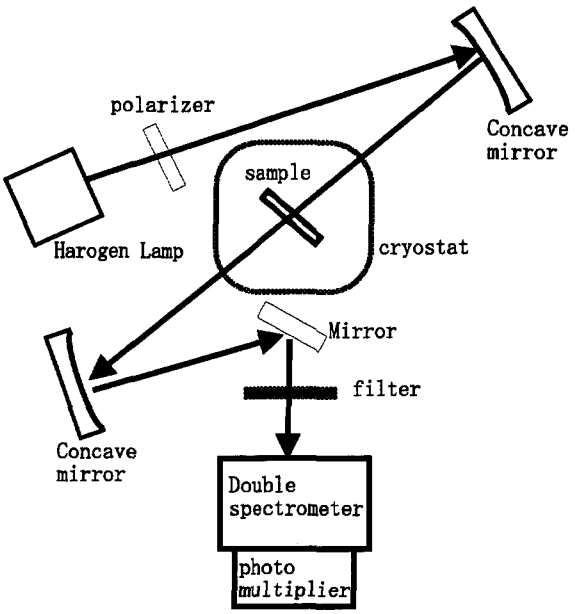

Figure 9.1: Schematic diagram of the absorption measurement

A schematic diagram of the absorption measurement is shown in Fig. 9.1. A halogen lamp was used as the light source. A double polychromator (SPEX 1680B) and a photo-multiplier (HAMAMATU R928) were used to measure the transmission spectra. Absorption spectra were derived from the transmitted light, assuming a constant reflectivity of R~0.2 [80] in the measured photon energy region.

The absorption spectrum of c–$GeSe_2$ at 15K is displayed in Fig. 9.2. As confirmed by the resonant Raman study, the absorption spectra below 2.9 eV corresponds mainly to indirect transition. The exciton absorption peak is observed at 2.85 eV in $\boldsymbol{E} \parallel \boldsymbol{a}$ polarization and not observed in $\boldsymbol{E} \parallel \boldsymbol{b}$ polarization. The fairly broad linewidth of the exciton peak has been attributed to the existence of strong electron-phonon interactions.

9.3 Results and discussion: photoluminescence measurement

Single $GeSe_2$ crystals were prepared by a vapor phase growth method from melt-quenched $GeSe_2$ bulk glasses as described in Section 8.2. A schematic diagram of

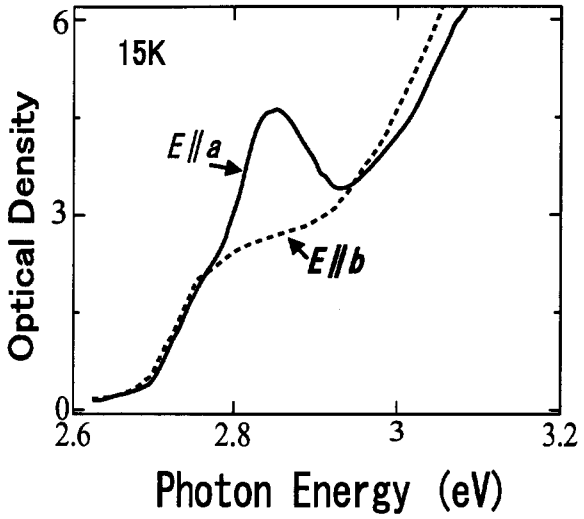

Figure 9.2: Absorption spectra of c–$GeSe_2$ at 15 K in the $\boldsymbol{E}\|\boldsymbol{a}$ and $\boldsymbol{E}\|\boldsymbol{b}$ polarization.

the PL measurement is depicted in Fig. 9.3. The cw laser lights in an energy range of 2.54–2.81 eV are used. For time-resolved measurement, the lights are chopped by an acousto-optic modulator or an electro-optic modulator. The laser pulse is shown in Fig. 9.4; the width was 3 msec and the frequency was 166.6 Hz. The PL spectra were taken by using a monochromator, a photo-multiplier (HAMAMATSU R5509-71A), and a gated photon counter (Stanford SR400).

PL spectra

Gaussian shaped PL spectra with ~0.3 eV FWHM around 1 eV are shown in Fig. 9.5. The PL peak energy increases from 0.99 eV to 1.14 eV with increasing excitation energies from 2.54 eV to 2.81 eV. The FWHM has its maximum at the excitation energy about 2.66 eV. The shift of the peak energy and the increase of the FWHM imply the existence of two PL bands.

9.3.1 Decay kinetics

We resolve the two PL bands of c–$GeSe_2$ by the time-resolved measurement. Figure 9.6 shows the decay kinetics measured at four luminescent photon energies indicated by arrows in Fig. 9.5. For the excitation at 2.54 eV, 2.71 eV, or 2.81 eV; the decay curves are nearly independent of the luminescent photon energy. The decay curves excited at 2.71 and 2.81 eV are identical. Thus, we identify two separate PL bands: the PL band excited at 2.54 eV (P1) and the band excited at 2.71 eV and 2.81 eV (P2). For the

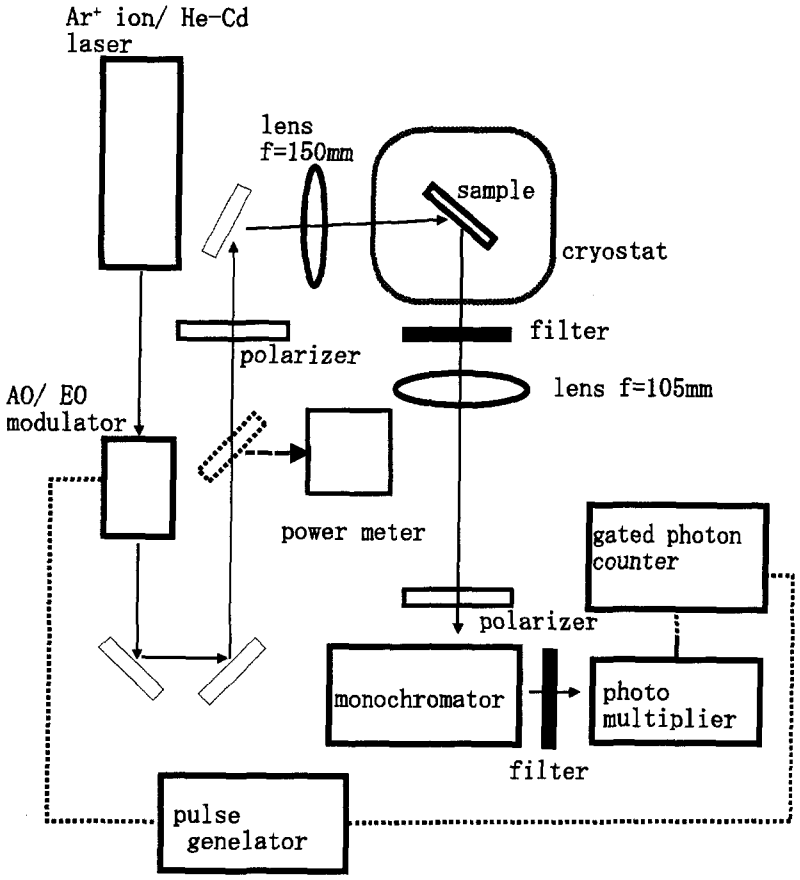

Figure 9.3: Experimental setup for time-resolved photoluminescence measurement.

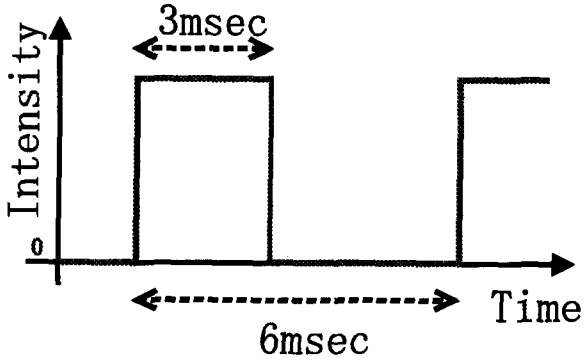

Figure 9.4: Schematic illustration of excitation light pulse chopped by AO or EO modulator. The pulse width is 3 msec and the frequency is 166.6 Hz.

excitation at 2.62 eV and 2.66 eV, the decay curves at a lower luminescent energy side resembles that of the P1 band, and, with increasing the measured luminescent photon

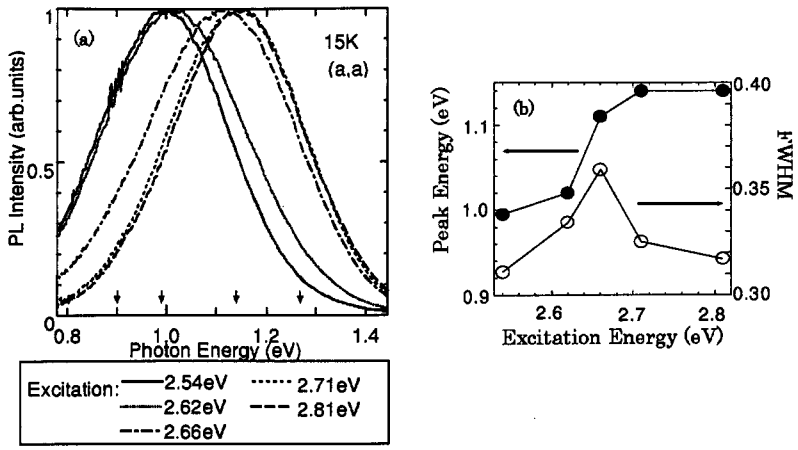

Figure 9.5: (a) Photoluminescence spectra of c–$GeSe_2$ at 15K for the excitation photon energies of 2.54~2.81 eV. The incident light polarization is parallel to the a axis, and the detected polarization is also parallel to the a axis. We use the symbol (a,a) to refer to this configuration. The spectra are normalized to the peak intensity. The arrows indicate the energy position at which we measure the decay curves. (b) PL peak energy and FWHM obtained by a single Gaussian curve fit.

energies, the decay curves approach that of the P2 band. The decay curves excited at 2.62 eV and 2.66 eV are composed of those of the P1 and P2 bands. The shift of the peak energy in the PL spectra, shown in Figs. 9.5, can be explained by the change of the intensity ratio between the P1 and P2 bands.

Excitation spectra

We can separate the PL spectra into the two Gaussian curves corresponding to the P1 and P2 band, as shown in the inset of Fig. 9.7. The obtained peak energies and FWHM's are listed in Table 9.1 Resolved excitation spectra of the P1 and P2 bands

Table 9.1: Peak energies and FWHM of the P1 and P2 bands at 15 K

	Peak energy (eV)	FWHM (eV)
P1	0.99	0.31
P2	1.14	0.32

are displayed in Fig. 9.7. The excitation spectrum for the P1 band has a peak around

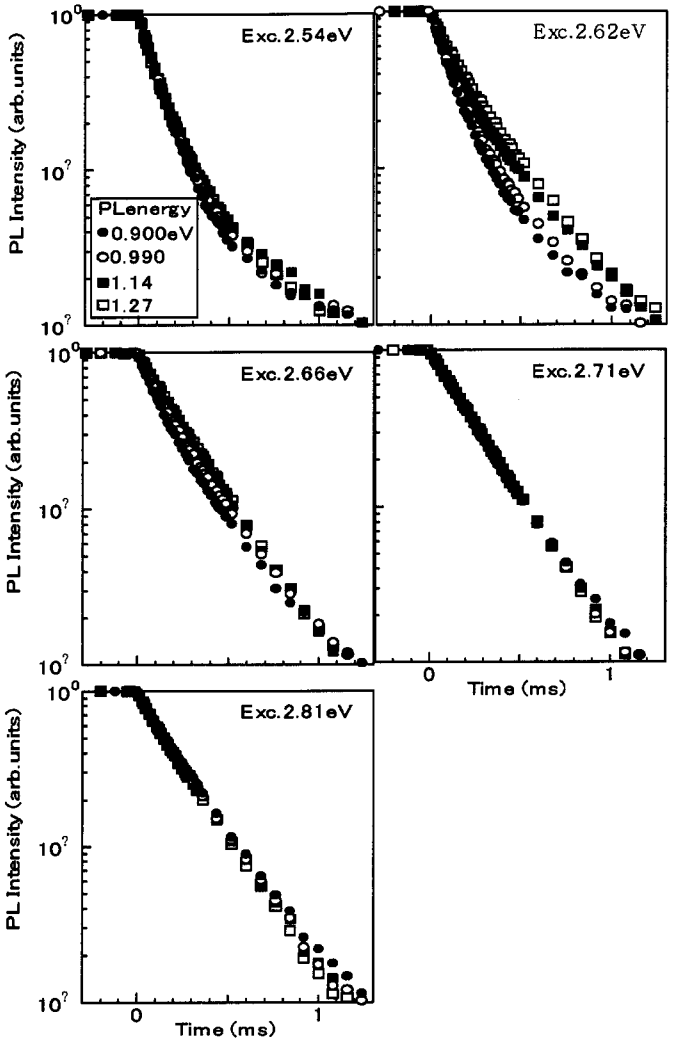

Figure 9.6: Decay curves of the photoluminescence at 15 K for various excitation photon energy. The measured luminescent photon energies are indicated by arrows in Fig. 9.5.

2.6 eV while that of the P2 band increases monotonically and, above 2.71 eV, P2 band dominates. This is consistent with the results of decay kinetics.

9.3.2 Polarization dependence

Figure 9.8 shows the polarization dependence in the PL spectra and the decay kinetics. No polarization dependence is observed both in the P1 and P2 bands. In addition, we investigated the PL spectra and the decay curves for various orientations of the detected polarization in the a–b, and the a–c planes, and found that they are independent of the orientation of the polarization. It should be noted that the possibility of circular

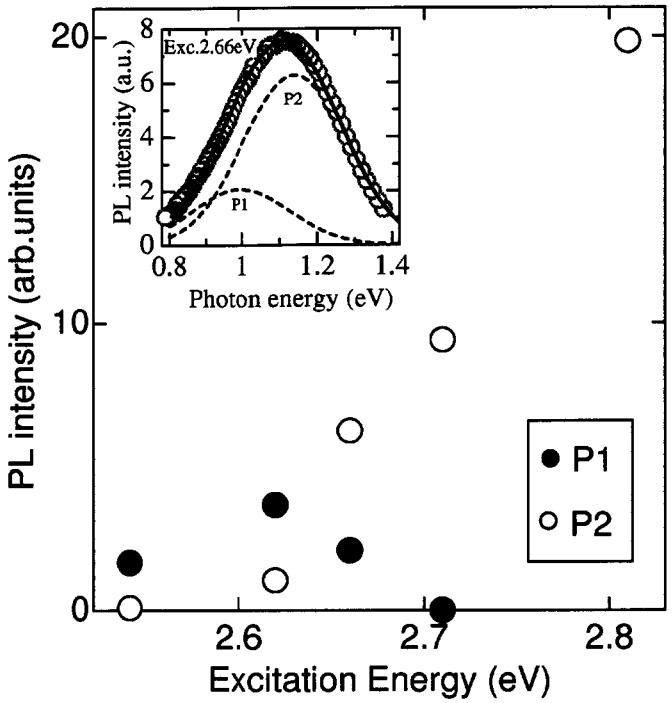

Figure 9.7: Excitation energy dependence of the photoluminescence intensities of the P1 and P2 bands at 15 K. The PL spectra are deconvoluted by two Gaussians, as shown in the inset. The photoluminescence intensities are normalized to the incident photon flux.

polarization of the luminescence is excluded by the experiments using a $\lambda/4$ waveplate. These polarization independences are probably due to the isotropy of the radiative centers of the P1 and P2 bands on the a–b layer plane. In the following discussion, we treat only the PL in the (a,a) configuration.

9.3.3 Temperature dependence

In the temperature range from 2 K to 40 K, the peak energies of the PL spectra excited at 2.54 eV and 2.71 eV are independent of temperature, as shown in Fig. 9.9; one PL band, P1 or P2, is excited by 2.54 eV or 2.71 eV light, respectively. Figure 9.10 shows the temperature dependence of the decay kinetics at the peak energies of the P1 and P2 bands. The temperature dependence of the decay kinetics is apparently different between P1 and P2 bands . To investigate the temperature dependence of the decay times, we fit the decay curves by exponential functions. The decay curves are fitted well by assuming the fast and slow components of the P1 band, and one component of

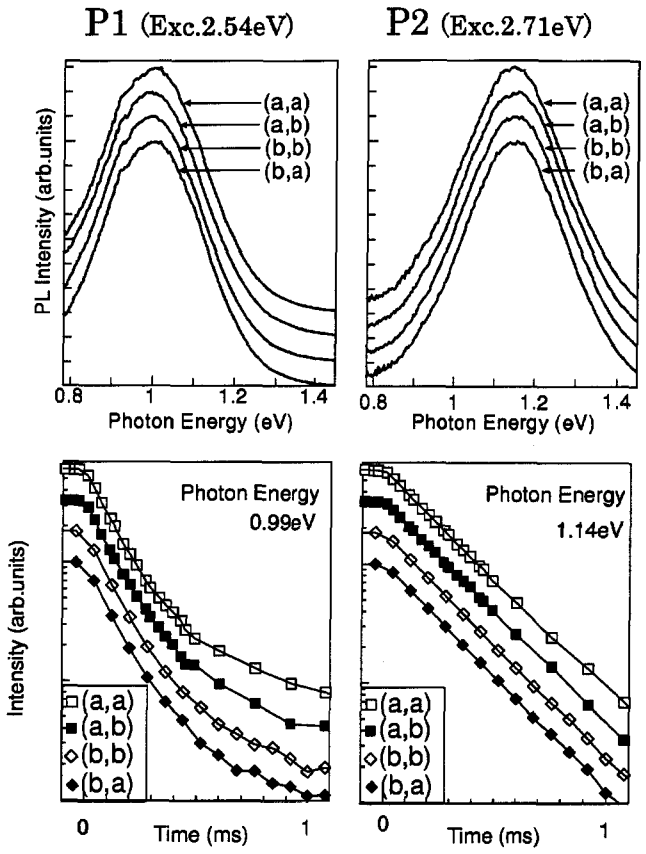

Figure 9.8: Polarization dependence of the photoluminescence spectra and the decay curves of P1 and P2 bands at 15 K. The decay curves are measured at the peak energies of the PL's. The photoluminescence spectra and the decay curves are displaced vertically for clarity.

the P2 band;

$$I_{\mathrm{P1}} = A\exp\left(-\frac{t}{\tau_{fast}}\right) + (1-A)\exp\left(-\frac{t}{\tau_{slow}}\right), 0 < A < 1 \tag{9.1}$$

$$I_{\mathrm{P2}} = \exp\left(-\frac{t}{\tau}\right) \tag{9.2}$$

where A, τ_{fast}, τ_{slow}, and τ are introduced as adjustable parameters. The obtained decay times are listed in Table 9.2.

Fig. 9.11 shows an Arrhenius plot of the decay rates. With increasing temperature, the decay rates of the fast and the slow components of the P1 band increase more rapidly than that of the P2 band, reflecting the difference of the activation energies. The activation energies are obtained by fitting with following equation formed by a superposition of a temperature-independent and a thermally activated form,

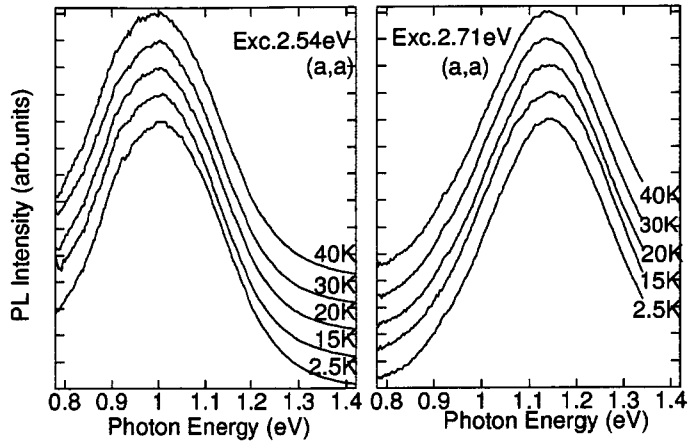

Figure 9.9: Photoluminescence spectra in the (a,a) configuration from 2.5 K to 40 K with excitation energy at 2.54 eV and 2.71 eV. The spectra are vertically displaced for display purpose. The peak energies of the PL spectra do not change in this temperature range.

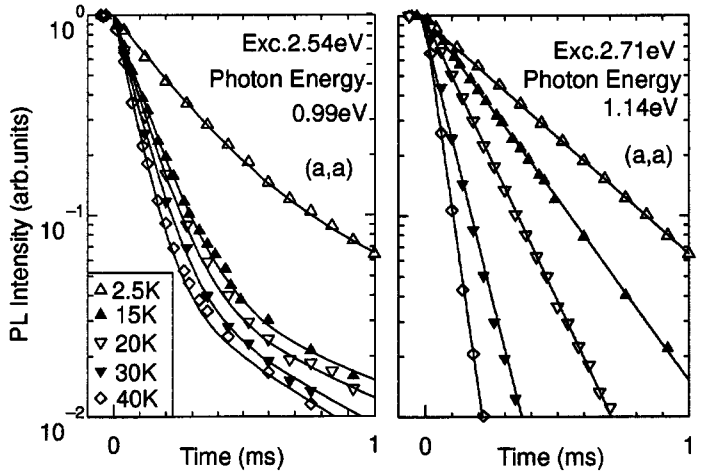

Figure 9.10: Temperature dependence of the decay curves with excitation energy at 2.54 eV and 2.71 eV. The decay curves are measured in the (a,a) configuration at the peak energies of the P1 and P2 bands.

$$\nu = \nu_r + m \exp\left(-\frac{\Delta E}{k_B T}\right), \tag{9.3}$$

where m, ΔE are adjustable parameters. As the temperature-independent recombination rate ν_r, we have used the decay rate at 2.5 K. The obtained activation energies,

Table 9.2: Temperature dependence of decay times

T(K)	decay time τ (μsec)		
	P1		P2
	fast	slow	
2.5	2.3×10^2	1×10^3	3.7×10^2
15	1.1×10^2	8×10^2	2.4×10^2
20	9.7×10	7×10^2	1.6×10^2
30	8.3×10	6×10^2	8.3×10
40	6.8×10	5×10^2	4.8×10

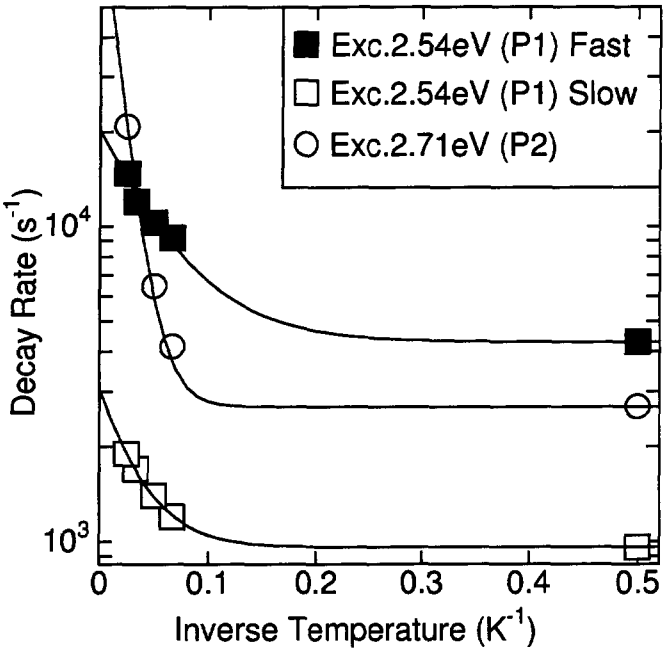

Figure 9.11: Arrhenius plot of the decay rates of fast and slow components of the P1 band, and the P2 band.

ΔE, are listed in Table 9.3. Because of the weakness of the intensity of the slow component of the P1 band, the experimental error of the decay rate is larger than the other values.

Table 9.3: Activation energies of the P1 and P2 bands

		ΔE (meV)
P1	fast	1.7 ± 0.5
	slow	~3 ± 1
P2		5.7 ± 0.3

9.3.4 Triplet models for the nature of the P1 and P2 bands

Thermal activation energy for nonradiative transition has been reported to about 95 meV [188] on the basis of the temperature dependence of the PL intensity. This value is extremely high, compared with the obtained activation energies. Below 40K, the nonradiative process is negligible.

As mentioned before, the origin of the luminescence in $GeSe_2$ is similar to that in As_2Se_3. Ristein *et. al.* have proposed a self-trapped triplet exciton model for the nature of the luminescence of As_2Se_3 [83]. The luminescence from triplet states have a long decay time since dipole transitions from a pure triplet to a singlet ground state are strictly forbidden, and the luminescence from triplet states are caused by the mixing of singlet and triplet character. Both of the P1 and P2 bands in *c*–$GeSe_2$ have reasonably long decay times (10^2~10^3 μsec) for triplet luminescences. Then, we assume that the radiative centers of the P1 and P2 bands are the triplet states of a self-trapped exciton (STE).

Figure 9.12 shows schematic energy levels of triplet models for the P1 and P2 bands. The triplet levels are labeled as T_1, T_2, and T_3 with radiative decay times ν_1, ν_2, and ν_3, respectively. The energy splittings of the highest triplet level, T_3 , from the other two levels, T_1 and T_2 , correspond to the activation energies listed in Table 9.3. The cross relaxation rates are given by $m\exp(-\Delta E_{13}/k_BT)$, $m\exp(-\Delta E_{23}/k_BT)$. In this model, we neglect the cross relaxation between the T_1 and T_2 levels within the optical life times since the mutual splitting of the two levels is about 1 meV (8 cm^{-1}), which is an energy at which there exist no optical phonons (see Sec. 8) and exists only a low density of acoustic phonons. The biexponential decay kinetics of the P1 band is explained by assuming that the transition rates between the T_3 level, and the other two levels are much faster than the radiative decay rate ν_3, and much slower than ν_1 and ν_2. In this condition, the carriers at the T_3 level are thermally transferred to the T_1 or T_2 level before radiative recombination, and the carriers at the T_1 or T_2 level radiatively recombine before the thermal activation to the T_3 level. Thus, the luminescences from the T_1 and T_2 levels decay independently; they are the fast and slow component of the luminescence.

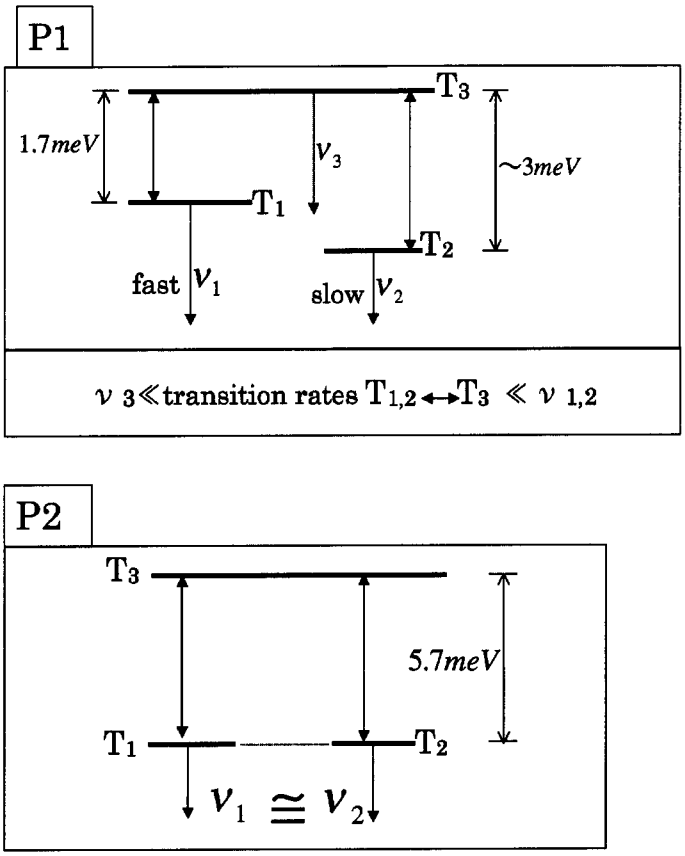

Figure 9.12: Schematic energy levels of the triplet models for the P1 and P2 bands. The energy splitting of the highest triplet level, T_3, from the other two levels, T_1 and T_2, are regarded as the activation energies obtained from our experiments.

Next we discuss the P2 band which shows the single exponential decay. The single exponential behavior of the P2 band should be explained by assuming that the two levels T_1 and T_2 are degenerate: $\nu_1 = \nu_2$ and $\Delta E_{13} = \Delta E_{23}$. We have ruled out an alternative interpretation that all the triplet levels are in thermal equilibrium to show single exponential decay. In this alternative interpretation, $m\exp(-\Delta E_{13,23}/k_BT) \gg \nu_1$, ν_2 should be held. However, the relaxation rate, $m\exp(-\Delta E_{13,23}/k_BT)$, at 2.5 K is about 10^{-7} Hz which is much slower than the decay rate (10^4 Hz) of the P2 band.

We assign the thermal activation energies, 1.7 meV, 3 meV, and 5.7 meV, (13.7 cm^{-1}, 24 cm^{-1}, and 46.0 cm^{-1}, respectively) to the splittings of the highest-lying level, T_3, and the other two levels, T_1 and T_2. The energies are close to those of the low-frequency optical phonons listed in Section. 8.3.2. The cross relaxation between the T_3 level and the other two levels should be caused by the emission or absorption of these

phonons.

9.3.5 Radiative structures

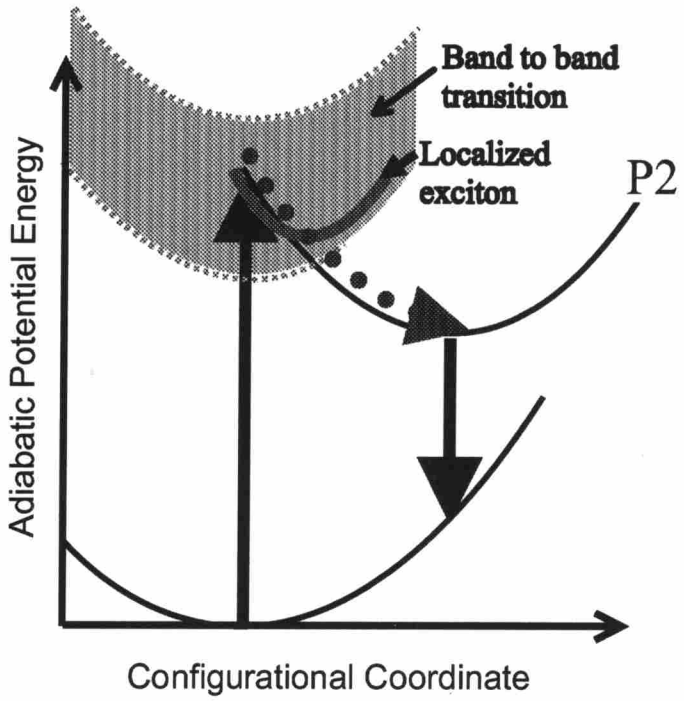

Figure 9.13: Schematic configuration coordinate diagram proposed for P2 luminescent state.

Before discussing the radiative structures, we show that the band edge exciton relaxes to the P2 luminescent state in view of polarization dependence of optical properties. The PL spectra and the decay kinetics do not depend on the polarization of the incident and detected lights, as shown in Fig. 9.8. Both photoexcited carriers created by the lights of $\boldsymbol{E}\|\boldsymbol{a}$ and $\boldsymbol{E}\|\boldsymbol{b}$ polarizations relax to the same PL state. Moreover, the quantum efficiency of the PL excited at 2.81 eV is the same for both polarizations in spite of the strong anisotropy in the absorption coefficient; in the $\boldsymbol{E}\|\boldsymbol{a}$ polarization, the exciton absorption is added to a band-to-band absorption. From these polarization independent quantum efficiency, it follows that both the electron-hole pairs excited by the band to band transition and the quasi-localized band edge exciton relax to the P2 band, as shown in Fig. 9.13.

Now we discuss the relaxation process of the exciton, based on the model proposed in Sec. 8.3.2. The band-edge exciton is localized around the inversion center where a strong π-type interlayer interaction, denoted by thick dashed line in Fig. 9.14, exists

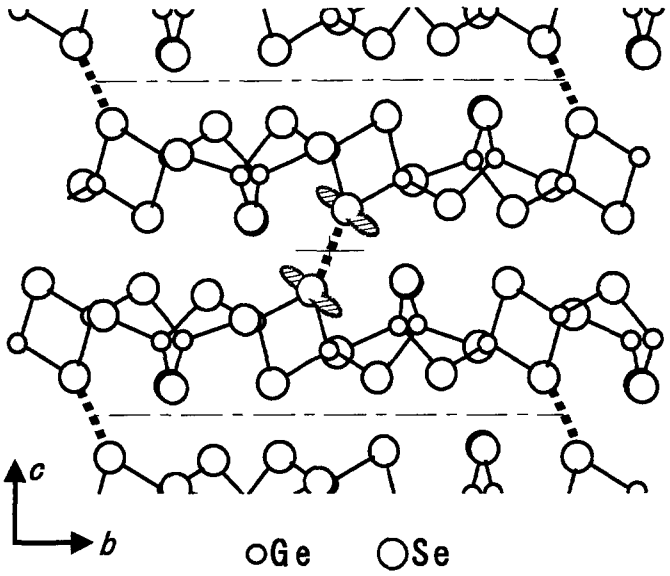

Figure 9.14: Projection of the layered structure of c–$GeSe_2$. The inversion center is indicated by a cross symbol. Thick dashed lines indicate the strong π-type interlayer interaction between the Se atoms whose lone-pair orbitals (shaded regions) are exactly parallel to each other.

between exactly parallel lone-pair orbitals of Se atoms. The exciton is assigned to the transition from the π^* state of the lone-pair electrons to the antibonding state of Ge-Se bonds forming the bottom of the conduction band. Because the hole state arising from the π^* state is localized around the Se atoms, the creation of the hole state will reduce the electron repulsive force between the Se atoms. It makes the Se atoms approach each other, and causes the enhancement of the π interaction, leading to further increase of the π–π^* splitting. On the other hand, the photoexcitation of electron to the antibonding states will weaken the local covalent Ge-Se bonds, which causes further relaxation. Thus, by lattice relaxation, both electron and hole states are moved deeper into the optical gap to form the luminescent center of the P2 band. It is noteworthy that this relaxation process is similar to the formation process of a self-trapped exciton in c–As_2Se_3 [83].

Through the relaxation process with distortion of local bonds the luminescent center should be strongly localized. If this luminescent state is relatively extended along the layer plane, the PL would show an anisotropic optical property. The polarization independence of the P2 bands for the $\boldsymbol{a}$–$\boldsymbol{b}$ and the $\boldsymbol{a}$–$\boldsymbol{c}$ planes supports the localization of the luminescent center. We conclude that the band edge exciton quasi-localized at the edge-sharing tetrahedra is further localized to form the P2 luminescent center. The

P2 luminescent state is strongly localized around the inversion center located between particular Se atoms on neighboring layers. It should be noted that as shown in Fig. 9.13, the photoexcited carriers by band-to-band transitions also relax to the P2 state in the same way.

9.4 Conclusions

We clearly separate two PL bands, the P1 and P2 bands, from time-resolved measurement, whose peak energies are 0.99 eV and 1.14 eV, respectively. The decay kinetics of the P1 and P2 bands is apparently different; the P1 band shows single exponential behavior while the P2 band shows biexponential behavior. According to the temperature dependence of the decay times, we obtain the thermal activation energies of the P1 and P2 bands. The PL properties can be explained by the triplet model. In addition, on the basis of the exciton structure and the polarization independence. Through the discussion on the relaxation process of the band edge exciton, we propose a local structure of the radiative center; the P2 luminescent center is strongly localized around the inversion center located between adjacent layers.

Chapter 10

Summary

In this thesis, we have presented a comprehensive study of the roles of nanoscopic structural units in Ge_xSe_{1-x} glasses in relaxation behaviors around T_g, structural changes toward crystallization, electronic structures around band-tails, and relaxation processes of photoexcited carriers. First, we have shown that the variation of Se_n ($n > 2$) chain segments essentialy determines relaxational behaviors of networks. We have also shown that the compositional dependence of resonant Raman spectra is explained by the variation in lengths of the Se_n chain and the CST chain. Second, we have found that intrinsic inhomogeneity in Ge–Ge ethan-like units, Se-Se bonds, and fragments similar to β–$GeSe_2$ can cause significantly different macroscopic structural changes in $GeSe_2$ glass. Finally, we have demonstrated that threefold coordinated Se atoms forming Se–Se bonds play a key role in the photoinduced structural change and the dynamics of photoexcited carriers in $GeSe_2$ glass.

In chapter 3, we have investigated quasielastic contribution in the low-frequency Raman spectra of Ge_xSe_{1-x} glasses, and have found that the quasielastic contribution appears in the floppy glasses ($x \leq 0.20$) but it does not in the rigid ones ($x \geq 0.23$). The quasielastic intensity and damping rate is obtained by a single Lorentzian fitting for each quasielastic contribution. The temperature independence of the damping rates indicates that the quasielastic contribution originates from the fast (β) process of relaxation. The composition dependence of the quasielastic intensity suggests that relaxational modes have the same origin as floppy modes, either of which is attributed to the rotating motions of Se_n segments ($n > 2$). The transition of the relaxational dynamics from floppy to rigid supports the validity of the constraint counting concept for the dynamical properties, and the sharp-transition behavior gives an evidence for the self-organization concept.

In chapters 4 and 5, we have investigated structural changes upon heating toward crystallization in $GeSe_2$ glasses by high- and low-frequency Raman scattering. We have found that three distinct phases (β–, α–, and ϕ-$GeSe_2$) can be formed from apparently the same glass structure ("trifurcated crystallization"). High-frequency dynamics upon heating is mainly attributed to transformation from the ethane-like units involving Ge–Ge bonds to the CST units, which leads to an ordering of the CST chains. On the other hand, low-frequency dynamics upon heating is mainly attributed to growth of cohesive domains similar to β-$GeSe_2$. The trifurcated behavior is the evidence of the

existence of inhomogeneous distributions of Ge–Ge ethan-like units, Se–Se bonds, and the domains. We have also shown that the structural changes are reversible. The reversibility demonstrates the importance of such structural units and domains on the stability of the glassy network.

In chapter 6, we have systematically examined the resonant Raman enhancements of the breathing CST mode and the stretching Se chain (Se–Se) mode in Ge_xSe_{1-x} glasses at RT. The resonant enhancement of the CST mode is stronger than that of the Se chain segments in Se-rich glasses ($0.05 \lesssim x \lesssim 0.18$). We have found that with increasing Ge content, the magnitude of the enhancement decreases, and then, the resonant enhancements of the two modes become nearly the same around the rigidity percolation threshold ($0.20 \lesssim x \lesssim 0.26$). With further increasing Ge content, the enhancement of the Se–Se mode is stronger than that of the CST mode in Ge-rich glasses ($x \gtrsim 0.28$). Based on this compositional trend of the resonant behavior, we have suggested that the floppy and rigid regions have their minimum sizes around the rigidity threshold. This corresponds to the disappearance of relaxational modes at the threshold because the Se_n segments with minimum length ($n = 2$) cannot show rotating motions.

In chapter 7, we have investigated resonant Raman spectra in $GeSe_2$ glass at 15 K, and have found an excess resonant enhancement of Se–Se mode relative to CST mode. We have conclude that the enhancement is caused by the photoinduced structural change inducing the photodarkening. We have also studied the reversible change of the excess resonant enhancement with the excitation power. We have demonstrated that the power dependent behavior has the same origin as that of the excess resonant enhancement, both of which are attributed to a creation of transient threefold coordinated Se atoms that form Se–Se bonds. We have proposed that the transient defective state results in bond-switching which induces photodarkening or formation of excess resonant states.

In chapters 8 and 9, we have investigated the resonant Raman spectra and time-resolved photoluminescence of β-$GeSe_2$ at RT and 15K. We have found that almost all the modes including a rigid layer mode resonate with localized exciton while two modes do not. On the basis of the results of a VFF-BP model calculation, we have demonstrated an essential difference in the atomic motions between the resonant and nonresonant modes, and have suggested that the structure of the localized exciton located around the particular pair of Se atoms forming the π-type interlayer interaction. Furthermore, by photoluminescence (PL) measurement, we have traced the relaxation process of the localized exciton. We have clearly separated the PL into two PL bands, P1 and P2, from its decay kinetics, and then we have demonstrated that the localized exciton relaxes into the P2 band. Based on this fact, we have found that the P2

luminescent center is strongly localized around the inversion center located between adjacent layers.

Our view of the structure that involves the inhomogeneously distributed structural units and domains on a nanoscopic scale would certainly add to a better understanding of the structure and transformations in network glasses in general. In addition, the investigation of structures of Ge–Se glasses is also important because of the increasing potential in industrial applications, such as solar cells, electronic switching and memory devices [189,190], X-ray image detectors [191], IR optical devices [193] optical storage materials [192,194], high resolution photoresists [195], and chemically stable and water resistant passivation layers [196].

Appendix A

Raman scattering

A.1 Light scattering by a structural unit

A.1.1 Nonresonant condition

Let us consider a vibrational mode of frequency ω_v in a structural unit or a molecule with N atoms. This mode is characterized by displacements of the N atoms with time dependences $exp(\pm\omega_v t)$ and amplitudes u_i(i=1,2,...N). The amplitude u_i are related to the normal mode coordinate ξ through the normal mode transformation [186,197]:

$$\boldsymbol{u_i}(\pm\omega_v t) = M_i^{-1/2}(\boldsymbol{e_i}\xi e^{-i\omega_v t} + c.c.), \tag{A.1}$$

where $\sum_{i=1}^{N} |\boldsymbol{e_i}|^2 = 1$, M_i is the mass of atom i, and $c.c.$ stands for the complex conjugate of the preceding term. The set of vectors $\boldsymbol{e_i}$ represents the eigenvector of the vibrational mode.

Here we assume that ω_v is small compared with the "electronic energies" which determine the polarizability α induced by an electronic modulation. As the simplest case, we discuss the polarizability α produced by an electron, with charge e and mass m, tied to atomic cores by a restoring force $k = \omega_0^2 m$, where ω_0 is the vibrating frequency of the harmonic oscillator. In this case,

$$\alpha = \frac{e^2 m}{\omega_0^2 - \omega^2 - i\omega\gamma}, \tag{A.2}$$

where γ is the damping constant. The above assumption for ω_v is given as:

$$\omega_v^2 \ll \left|\omega_0^2 - \omega^2 - i\omega\gamma\right|. \tag{A.3}$$

This condition means that the light energy is away from the resonance energy.

In this condition, we can treat the phonon as a static deformation of the molecule and define at each constant of time a polarizability $\alpha(\omega_L, \xi)$ (adiabatic approximation). By expanding $\alpha(\omega_L, \xi)$ in powers of ξ, we find

$$\tilde{\boldsymbol{\alpha}}(\omega_L, \xi) = \tilde{\boldsymbol{\alpha}}(\omega_L) + \frac{\partial\tilde{\boldsymbol{\alpha}}}{\partial\xi}\xi e^{-i\omega_v t} + c.c. + \frac{1}{2}\frac{\partial^2\tilde{\boldsymbol{\alpha}}}{\partial\xi^2}\xi^2 e^{-i(2\omega_v)t} + c.c. + \frac{1}{2}\frac{\partial^2\tilde{\boldsymbol{\alpha}}}{\partial\xi\partial\xi^*}(\xi\xi^* + \xi^*\xi) + ... \tag{A.4}$$

In the classical light scattering theory (dipole radiation), this modulation of the polarizability produces scattered radiation at the frequencies $\omega_s = \omega_L$, $\omega_L \pm \omega_v$, and

$\omega_L \pm 2\omega_v$, which corresponds to Rayleigh scattering, first-order Raman scattering, and second-order Raman scattering (overtone), respectively. The first-order Stokes Raman scattering cross section is given by:

$$\frac{d\sigma_s}{d\Omega} = \frac{\omega_s^4}{(4\pi\epsilon_0)^2 c^4} \left| \hat{\boldsymbol{e}}_s \cdot \frac{\partial \tilde{\boldsymbol{\alpha}}}{\partial \xi} \cdot \hat{\boldsymbol{e}}_L \right|^2 < \xi\xi^* >, \tag{A.5}$$

where <> represent the thermodynamical average over the ground state of the structural unit. By replacing ξ and ξ^* by the operators ξ and $\xi^\dagger$ (second-quantization), the thermodynamical average term is written as

$$< \xi\xi^\dagger > = < n|\xi|n+1 >< n+1|\xi^\dagger|n > = \frac{\hbar}{2\omega_v}(n+1), \tag{A.6}$$

where n is the Bose factor.

For the discussion of difference of the Raman cross section between the vibrational modes, the essential term is the "Raman polarizability" $\partial\tilde{\boldsymbol{\alpha}}/\partial\xi$. The normal coordinate ξ corresponds to an ensemble of static atomic displacements given by Eq. A.1 with $t = 0$. Hence $\partial\tilde{\boldsymbol{\alpha}}/\partial\xi$ can be written as

$$\frac{\partial \tilde{\boldsymbol{\alpha}}}{\partial \xi} = \sum_{i=1}^{N} \frac{\partial \tilde{\boldsymbol{\alpha}}}{\partial \boldsymbol{u_i}} \times \frac{\partial \boldsymbol{u_i}}{\partial \xi} = \sum_{i=1}^{N} \frac{\partial \tilde{\boldsymbol{\alpha}}}{\partial \boldsymbol{u_i}} M_i^{-1/2} \hat{\boldsymbol{e}}_i. \tag{A.7}$$

This equation enables us to calculate $\partial\tilde{\boldsymbol{\alpha}}/\partial\xi$ since $\partial\tilde{\boldsymbol{\alpha}}/\partial\boldsymbol{u_i}$ can be obtained by performing calculations of the polarizability of the structural units with all possible small deformations $\boldsymbol{u_i}$. Since such a first principle calculation is very difficult, many semi-empirical methods have been proposed. One of those calculations is bond polarizability method [198] which assigns to each bond a polarizability which is a function of the bond length l only. In other words, the Raman polarizability is written by only the two differential polarizabilities; a parallel one to the bond direction $\partial\alpha_\parallel/\partial l$ and a perpendicular one $\partial\alpha_\perp/\partial l$.

A.1.2 Resonant condition

To discuss resonant Raman scattering, we replace the polarizability $\tilde{\boldsymbol{\alpha}}$ by a sum of terms of the simple formula A.2, where the various ω_0 will be the electronic excitation energies. To preserve the tensorial character of $\tilde{\boldsymbol{\alpha}}$, we multiply the formula A.2 by the "oscillator strength tensor" $\tilde{\boldsymbol{F}}$. Thus, for ω near a given ω_0, we approximate $\tilde{\boldsymbol{\alpha}}$ by

$$\tilde{\boldsymbol{\alpha}} = \frac{e^2 m \tilde{\boldsymbol{F}}}{\omega_0 - \omega^2 - i\omega\gamma} + constant. \tag{A.8}$$

The Raman polarizability is written by diffentiating this as

$$\frac{d\tilde{\boldsymbol{\alpha}}}{d\xi} = \frac{2\omega_0(e^2 m)\tilde{\boldsymbol{F}}}{[\omega_0 - \omega^2 - i\omega\gamma]^2} \frac{d\omega_0}{d\xi} + \frac{e^2 m}{\omega_0 - \omega^2 - i\omega\gamma} \frac{d\tilde{\boldsymbol{F}}}{d\xi} \tag{A.9}$$

There are two contributions to the Raman polarizability: one is the change in excitation energy ω_0 with ξ, that is a diagonal matrix element of the *electron-phonon interaction*, and the change in $\tilde{\boldsymbol{F}}$ with ξ. The former is dominant unless $d\omega_0/d\xi$ vanishes, possibly as a result of symmetry selection rule. Throughout this paper, we focus on only the former since the vanishment will be improbable in disordered materials and crystal with low symmetry. Thus, the essential term for the resonant enhancement is $d\omega_0/d\xi$. For discussing the resonant process with strongly localized electronic states, the following expression of this term, obtained in the similar way to Eq. A.7, is very useful:

$$\frac{d\omega_0}{d\xi} = \sum_{i=1}^{N} \frac{\partial \omega_0}{\partial \boldsymbol{u_i}} M_i^{-1/2} \hat{\boldsymbol{e}}_{\boldsymbol{i}}. \tag{A.10}$$

Antiresonance

Here we introduce another interesting behavior for ω near ω_o, referred to as an *antiresonance*. As a result of an interference of a resonant (A.9) and a nonresonant ($\sim$constant) contribution to $d\tilde{\boldsymbol{\alpha}}/d\xi$ of *opposite signs*, the cross section σ decreases when ω approaches ω_0. The cross section decreases to zero before ω_0 and increases above the point. This antiresonance behavior can usually be fitted with the following expression:

$$\frac{\sigma}{\omega^4} = \left(A - \frac{B}{(\omega_0^2 - \omega^2)^2} \right)^2, \tag{A.11}$$

where A and B are adjustable fitting parameters.

A.2 Light scattering by crystals

The classical theory of Raman scattering in crystals with N unit cells can be obtained in a similar way as the above arguments for a structural unit or a molecule. Using Bloch's theorem, the eigenvectors of the lth unit cell, labeled by the position vector $\boldsymbol{R_l}$, are related to those of the unit cell at the origin $\boldsymbol{e_i}$ through

$$\boldsymbol{e_{il}} = \boldsymbol{e_i} e^{i\boldsymbol{q}\cdot\boldsymbol{R_l}}, \tag{A.12}$$

where $\sum_i^{unitcell} |\boldsymbol{e_{il}}(\boldsymbol{q})|^2 = 1$ and $\boldsymbol{q}$ is the wave vector of the phonon mode. The vibrational amplitude of a given atom of mass M_i in the cell $\boldsymbol{R_l}$ in the mode with frequency $\omega_v(\boldsymbol{q})$, becomes

$$\boldsymbol{u_{il}}(\boldsymbol{q}, \pm\omega_v t) = N M_i^{-1/2} [\boldsymbol{e_i}(\boldsymbol{q}) \xi_i(\boldsymbol{q}) e^{i[\boldsymbol{q}\cdot\boldsymbol{R_l} - \omega_v t]} + c.c.], \tag{A.13}$$

where ξ_i is the normal coordinate for the atom i. From the wave vector selection rule discussed below, it follows that only the scattering for $\boldsymbol{q} \cong 0$ is possible. The Stokes

Raman scattering cross section is obtained from Eq. A.5 by replacing the polarizability $\tilde{\alpha}$ with the susceptibility $\tilde{\chi}$

$$\frac{d\sigma_s}{d\Omega} = \frac{\omega_s^4 V}{(4\pi\epsilon_0)^2 c^4} \left| \hat{e_s} \cdot \frac{\partial \tilde{\chi}}{\partial \xi} \cdot \hat{e_L} \right|^2 < \xi(0)\xi^*(0) >, \tag{A.14}$$

where V is the scattering volume.

A.3 Wave vector selection rules –Difference between crystal and glass–

To discuss the wave vector selection rules, we introduce another useful expression for Raman cross sections. In this section, we show the essential part of the expression and ignore the tensorial character. The cross section is proportional to the dynamical structure factor $S(\boldsymbol{k}, \omega)$ given by the Fourier transformation of the space-time correlation function of the susceptibility fluctuations $\delta\chi(\boldsymbol{r}, t)$ [199,200]:

$$\frac{d\sigma_s}{d\Omega} \propto \omega_s^4 S(\boldsymbol{k}, \omega) \tag{A.15}$$

$$S(\boldsymbol{k}, \omega) \propto \int d\boldsymbol{r} \int d\boldsymbol{r}' < \delta\chi^*(\boldsymbol{r}, t)\delta\chi(\boldsymbol{r}', 0) > e^{-i[\boldsymbol{k}(\boldsymbol{r}-\boldsymbol{r}')-\omega t]}, \tag{A.16}$$

where $\boldsymbol{k} = \boldsymbol{k_L} - \boldsymbol{k_s}, \omega = \omega_L - \omega_s$, and $<>$ represent a space-time correlation. By introducing lattice displacement at $\boldsymbol{r}$, $R(\boldsymbol{r}, t)$, the susceptibility fluctuations is written as $\delta\chi(\boldsymbol{r}, t) = A(\boldsymbol{r})R(\boldsymbol{r}, t)$. This formula can be rewritten as

$$\delta\chi(\boldsymbol{r}, t) \propto \int d\boldsymbol{q} A(\boldsymbol{q}) R(\boldsymbol{q}) e^{-i[\boldsymbol{q}\boldsymbol{r}-\omega(\boldsymbol{q})t]}. \tag{A.17}$$

Keeping the relation $R^*(\boldsymbol{q})R(\boldsymbol{q}') = 0$ $(\boldsymbol{q} \neq \boldsymbol{q}')$ in mind, we obtain the space-time correlation function:

$$< \delta\chi^*(\boldsymbol{r}, t)\delta\chi(\boldsymbol{r}', t) > \propto \int d\boldsymbol{q} |A(\boldsymbol{q})|^2 < R^*(\boldsymbol{q})R(\boldsymbol{q}) > e^{i[\boldsymbol{q}(\boldsymbol{r}-\boldsymbol{r}')-\omega(\boldsymbol{q})t]}. \tag{A.18}$$

Substitution this formula for A.16 gives

$$S(\boldsymbol{k}, \omega) \propto \int d\boldsymbol{q} |A(\boldsymbol{q})|^2 < R^*(\boldsymbol{q})R(\boldsymbol{q}) > \int d\boldsymbol{r}'' e^{i(\boldsymbol{q}-\boldsymbol{k})\boldsymbol{r}''} \int dt e^{-i[\omega(\boldsymbol{q})-\omega]}, \tag{A.19}$$

where $\boldsymbol{r}'' = \boldsymbol{r} - \boldsymbol{r}'$. Since our Raman measurement time is always much longer than the characteristic time of the phonon vibration, the following time correlation always holds:

$$\frac{1}{2\pi} \int dt e^{-i[\omega(\boldsymbol{q})-\omega]} = \delta(\omega(\boldsymbol{q}) - \omega). \tag{A.20}$$

This is the energy conservation rule: $\omega = \omega_L - \omega_s = \omega(\boldsymbol{q})$. In crystals, the phonon correlation length, in which the vibrations are continuously wave-like and uniform, is

much longer than the wavelength of the light. In this condition, the following space correlation holds:

$$\frac{1}{(2\pi)^3}\int d\boldsymbol{r}'' e^{i(\boldsymbol{q}-\boldsymbol{k})\boldsymbol{r}''} = \delta(\boldsymbol{q}-\boldsymbol{k}). \tag{A.21}$$

This is the wave vector selection rule: $\boldsymbol{k} = \boldsymbol{k_L} - \boldsymbol{k_s} = \boldsymbol{q} \sim 0$. On the other hand, in disordered materials, this space correlation does not definitely hold due to the short phonon correlation length. This means that in strongly disordered materials such as glasses all the modes can contribute to the Raman scattering. In other words, the Raman scattering cross section is proportional to the vibrational density states $g(\omega)$. According to Shuker and Gammon [53], the first-order Raman scattering intensity of the strongly disordered materials is given as

$$I(\omega) = C(\omega)g(\omega)[n(\omega)+1]/\omega, \tag{A.22}$$

where $C(\omega)$ is the light-vibration coupling coefficient and $[n(\omega)+1]/\omega$ is the term coming from A.6.

Appendix B

Fracton model

Alexander and Orbach have pointed out the isomorphism between diffusion on a lattice and vibrational dynamics [165]. If the lattice is a fractal structure, the scaling of the diffusion coefficient with distance will lead to localization of vibrational modes in the acoustic range. The density of such localized modes ("fractons") reflects the scaling behavior of the diffusion coefficient and will scale with frequency according to the law $g(\omega) \propto \omega^{\tilde{d}-1}$, where $\tilde{d}$ is the spectral dimensionality which describe the degree of the localization of lattice vibration. We introduce in this chapter anomalous diffusion on fractals, onto which the low-frequency vibrational dynamics is mapped.

B.1 Diffusion on fractals

As a model for the diffusion, we consider a simple random walk on a fractal lattice [201]. The fractal dimension D_f is defined by the scaling of the mean mass M with their characteristic linear size L:

$$< M(L) > \propto L^{D_f}. \tag{B.1}$$

In the random-walk model, the walker advances one step to a nearest neighbor site

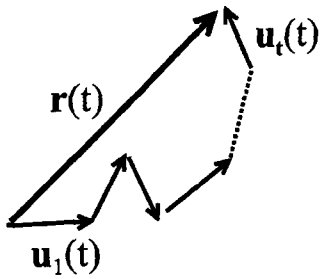

Figure B.1: Location of the walker $\boldsymbol{r}(t)$ after t steps $\sum_{i=1}^{t} \boldsymbol{u}_i$

in unit time. The walker can step with equal probability to any of the nearest neighbors. One of the main parameters characterizing a random walk is the mean square

displacement $< r^2(t) >$ made by the walker in t unit time (t steps):

$$< r^2(t) >= \left\langle \left(\sum_{i=1}^{t} \boldsymbol{u_i} \right)^2 \right\rangle = t + 2 \sum_{i>j}^{t} \langle \boldsymbol{u_i} \cdot \boldsymbol{u_j} \rangle . \tag{B.2}$$

where the walkers steps are denoted by $\boldsymbol{u_i}$ $(i = 1, 2, .., t)$, as shown in Fig B.1. For normal diffusion, the correlations $< \boldsymbol{u_i} \cdot \boldsymbol{u_j} >$ are all zero, and then, $< r^2(t) >$ is given as

$$< r^2(t) >= t. \tag{B.3}$$

On the other hand, the diffusion on fractals is anomalous, and the $< r^2(t) >$ scales with t as

$$< r^2(t) > \propto t^{2/D_w}, \tag{B.4}$$

where D_w is termed as the fractal dimension of the walk, and usually $D_w > 2$. The anomalous diffusion corresponds to the slowing down of the diffusion due to the obstacles such as holes, bottlenecks and dead ends which should appear in disordered system.

We now map the problem of anomalous diffusion to the vibrational density of states. The VDOS $g(\epsilon)$ is related to the probability $P(0, t)$ of the random walker to return to the origin after t unit time [165] as

$$P(0, t) = \int_0^\infty g(\epsilon) e^{-\epsilon t} d\epsilon. \tag{B.5}$$

Since the number of sites which a random walker has visited is proportional to the volume $V(t) \propto < r^2(t) >^{D_f/2} \propto t^{D_f/D_w}$ (see, Eq. B.4), $P(0, t)$ scales as

$$P(0, t) \propto 1/V(t) \propto t^{-D_f/D_w}. \tag{B.6}$$

Using Eqs. B.5 and B.6, the density of states $g(\epsilon)$ is written as

$$g(\epsilon) \propto \epsilon^{D_f/D_w - 1} = \epsilon^{\tilde{d}/2-1}, \tag{B.7}$$

where we define the spectral dimensionality as $\tilde{d} \equiv 2D_f/D_w$. Thus, the spectral dimensionality is identified as the relevant dimension for the density of states in a fractal lattice. We can rewrite the VDOS by letting $\epsilon \rightarrow \omega^2$ as

$$g(\omega) \propto \omega^{\tilde{d}-1}. \tag{B.8}$$

B.2 Nodes-links-blobs model

As a helpful model to understand the anomalous diffusion, we illustrate in Fig. B.2 the nodes-links-blobs picture [202,203]. The backbone consists of a network of quasi-one dimensional strings (links) tied together at nodes, and connecting more strongly

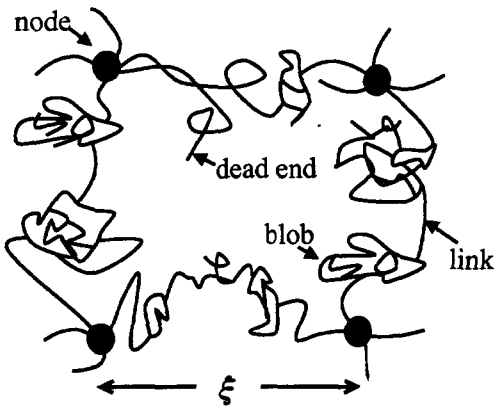

Figure B.2: Schematic illustration of the nodes-links-blobs model for the backbone of percolation clusters. The solid circles indicate nodes forming the homogeneous network.

bonded regions (blobs). The typical separation of the nodes forming the macroscopically homogeneous network equals the correlation length ξ of the percolation network, defined as the mean distance between two sites belonging to the same cluster. In the nodes-links model [204], from ξ upward, the network supports phonons; the vibrations of those nodes form a band that cannot extend beyond the cutoff frequency which separate the phonon and fracton regions. In other words, ξ is the boundary between the delocalized vibrations (phonon) and the localized ones (fracton). Here, it should be noted that such a change of vibrational dynamics is not only derived by the nodes-links model, but it is more generally demonstrated in percolation networks [204–207].

Bibliography

[1] R. Zallen, in *The Physics of Amorphous Solids* (Wiley, New York, 1983).

[2] J. C. Phillips, J. Non-Cryst. Solids **34**, 153 (1979); Phys. Today **35**, 27 (1982).

[3] M. F. Thorpe, J. Non-Cryst. Solids **57**, 355 (1983).

[4] H. He and M. F. Thorpe, Phys. Rev. Lett. **54**, 2107 (1985).

[5] For a recent review, see, K. Murase, in *Insulating and Semiconducting Glasses*, edited by P. Boolchand (World Scientific, 2000), Chap. 6c, p. 415.

[6] H. Fritzsche, in *Fundamental Physics of Amorphous Semiconductors*, edited by F. Yonezawa (Springer Verlag, Berlin, 1981), p. 1.

[7] K. Tanaka, in Ref [6], p. 104.

[8] P. Bak, *How Nature Works: The Science of Self-Organized Criticality*, (Copernicus, New York, 1996).

[9] P. Boolchand, X. Feng, D. Selvanathan, and W. J. Bresser, *Rigidity Theory and Applications*, edited by M. F. Thorpe and P. M. Duxbury (Kluwer Academic/ Plenum Publishers, 1999), p.279.

[10] *Phase Transition and Self-organization in Electronic and Molecular Network*, edited by J. C. Phillips and M. F. Thorpe (Kluwer Academic/ Plenum Publishers, 2001).

[11] W. H. Zachariasen, J. Am. Chem. Soc. **54**, 3841 (1932).

[12] P. Tronc, M. Bensoussan, A. Brenac, and C. Sebenne, Phys. Rev. B **8**, 5947 (1973).

[13] K. Murase, T. Fukunaga, K. Yakushiji, T. Yoshimi, and I. Yunoki, J. Non-Cryst. Solids **59& 60**, 883 (1983).

[14] P. Boolchand, in Ref. [5], Chap. 6b, p. 369.

[15] J. C. Phillips, in Ref. [9] P. 155; M. F. Thorpe, D. J. Jacobs, N. V. Chubynsky, and A. J. Rader, ibid., p239.

[16] M. F. Thorpe, D. J. Jacob, and B. R. Djordjević, in Ref. [5], p. 95.

[17] R. Azoulay, H. Thibierge, and A. Brenac, J. Non-Cryst. Solids **18**, 33 (1975).

[18] K. Murase and T. Fukunaga, in *Defects in Glasses*, edited by F. L. Galeener, D. L. Griscom, and M. J. Weber, [Mater. Res. Soc. Symp. Proc. **61**], 101 (1986).

[19] X. Feng, W. J. Bresser, and P. Boolchand, Phys. Rev. Lett. **78**, 4422 (1997).

[20] M. Tatsumisago, B. L. Halfpap, J. L. Green, S. M. Lindsay, and C. A. Angell, Phys. Rev. Lett. **64**, 1549 (1990).

[21] U. Senapati and A. K. Varshneya, J. Non Cryst. Solids, **185**, 289 (1995).

[22] A. Feltz, H. Aust, and A. Bleyer, J. Non Cryst. Solids, **55**, 179 (1983).

[23] W. A. Kamitakahara, R. L. Cappelletti, P. Boolchand, F. Gompf, D. A. Neumann, and H. Mukta, Phys. Rev. B **44**, 94 (1991).

[24] S. Asokan, E. S. R. Gopal, and G. Parthasarathy, Phys. Rev. B **35**, 8369 (1987); S. Asokan, E. S. R. Gopal, and G. Parthasarathy, Philos. Mag. B **57**, 49 (1988).

[25] W. J. Bresser, P. Boolchand, and P. Suranyi, Phys. Rev. Lett. **56**, 2493 (1986).

[26] M. Taniguchi, T. Kouchi, I. Ono, S. Hosokawa, M. Nakatake, H. Namatame, and K. Murase, J. Electron Spectroscopy and Related Phenomena **78**, 507 (1996).

[27] Y. Wang, O. Matsuda, K. Inoue, O. Yamamuro, T. Matsuo, and K. Murase, J. Non-Cryst. Solids **232–234**, 702 (1998).

[28] M. Nakamura, O. Matsusa, and K. Murase, Phys. Rev. B **57**, 10228 (1998).

[29] M. F. Thorpe, D. J. Jacobs, M. V. Chubynsky, and J. C. Phillips, J. Non-Cryst. Solids **266–269**, 859 (2000).

[30] M. F. Thorpe and M. V. Chubynsky, Lectures for the Summer 2000 workshop on "Properties and Applications of Amorphous Semiconductors and Glasses", to be published in the NATO ASI Series, edited by M. F. Thorpe and L. Tichy.

[31] S. R. Ovshinsky, Phys. Rev. Lett. **21**, 1450 (1968).

[32] S. R. Ovshinsky and H. Fritzsche, IEEE Trans. on Electron Devices **ED20**, 91 (1973).

[33] S. R. Ovshinsky, J. Appl. Photographic Eng. **3**, 35 (1977).

[34] M. Kastner, Phys. Rev. Lett. **28**, 355 (1972).

[35] R. A. Street, Solid State Commun. **24**, 363 (1977).

[36] M. Kastner, D. Adler, and H. Fritzsche, Phys. Rev. Lett. **37**, 1504 (1976).

[37] G. Pfeiffer, M. A. Paesler, S. C. Agarwal, J. Non-Cryst. Solids **114**, 130 (1989).

[38] For a review, see, K. Shimakawa, A. V. Kolobov, and S. R. Elliott, Adv. Phys. **44**, 475 (1995).

[39] H. Fritzsche, in Ref. [5], Chap. 10, p. 653.

[40] M. Frumer, A. P. Firth, and A. E. Owen, Philos. Mag. B **50**, 463 (1984).

[41] C. Y. Yang, M. A. Paesler, and D. E. Sayers, Phys. Rev. B **36**, 9160 (1987).

[42] S. A. Dembovskii. G. Z. Vinogradova and A. S. Pashinkin, Ruu. J. Inorg. Chem. **10**, 903 (1963).

[43] C. Z. Vinogradova, S. A. Dembovskii and N. B. Sivkova, Ruu. J. Inorg. Chem. **13**, 1051 (1968).

[44] L. Ross and M. Bourgon, Can. J. Chem. **47**, 2555 (1969).

[45] P. Quenez, P. Khodadad and R. Ceolin, Bull. Soc. Chem. Fr. **1**, 177 (1972).

[46] J. C. Malaurent and J. Dixmier, J. Non Cryst. Solids **35/36**, 1227 (1980).

[47] R. S. Nemanich and S. A. Solin, Solid State Commun. **21**, 273 (1977).

[48] W. J. Bresser, P. Boolchand, P. Suranyi, and J. P. De Neufville, Phys. Rev. Lett. **46**, 1689 (1981).

[49] U. Walter, D. L. Price, S. Susman, and K. J. Volin, Phys. Rev. B **37**, 4232 (1988).

[50] J. C. Phillips, J. Non-Cryst. Solids **43**, 37 (1981).

[51] P. H. Fuoss and A. Fischer-Colbrie, Phys. Rev. B **38**, 1875 (1988).

[52] P. Vashishta, R. K. Kalia, and I. Ebbsjö, J. Non Cryst. Solids **106**, 301 (1988); P. Vashishta, R. K. Kalia, G. A. Antonio, and I. Ebbsjö, Phys. Rev. Lett, **62**, 1651 (1989).

[53] R. Shuker and R. W. Gammon, Phys. Rev. Lett. **25**, 222 (1970).

[54] G. Lucovsky, J. P. deNeufville, and F. L. Galeener, Phys. Rev. B **9**, 1591 (1974).

[55] R. J. Nemanich, G. A. N. Connel, T. M. Hayes, and R. A. Street, Phys. Rev. B **18**, 6900 (1978).

[56] P. M. Bridenbaugh, G. P. Espinosa, J. E. Griffiths, J. C. Phillip, and J. P. Remeika, Phys. Rev. B **20**, 4140 (1979).

[57] K. Murase, K. Inoue and O. Matsuda, in *Current Topics in Amorphous Materials -Science and Technology-*, edited by Y. Sakurai, Y. Hamakawa, T. Masumoto, K. Shirae and K. Suzaki (Elsevier, Amsterdam, 1993), p47.

[58] O. Matsuda, K. Inoue, and K. Murase, Solid State Commun. **75**, 303 (1990).

[59] K. Inoue, O. Matsuda, and K. Murase, Solid State Commun. **79**, 905 (1991).

[60] K. Inoue, O. Matsuda, and K. Murase, J. Non-Cryst. Solids **150**, 197 (1992).

[61] K. Inoue, O. Matsuda, and K. Murase, Physica B **219& 220**, 520 (1996).

[62] K. Jackson, A. Briley, S. Grossman, D. V. Porezag, and M. R. Pederson, Phys. Rev. B **60**, R14 985 (1999).

[63] M. Cobb, D. A. Drabold, and R. J. Cappelletti, Phys. Rev. B **54**, 12162 (1996).

[64] S. Hosokawa, K. Nishihara, Y. Hari, and M. Taniguchi, Phys. Rev. B **47**, 15509 (1993).

[65] E. Bergignat, G. Hollinger, H. Chermette, P. Pertosa, D. Lohez, M. Lannoo, and M. Bensoussan, Phys. Rev. B **37**, 4506 (1988).

[66] K. Inoue, T. Katayama, K. Kawamoto, and K. Murase, Phys. Rev. B **35**, 7496 (1987). The crystal orientation is mistaken in the literature; replace $\parallel$ a with $\perp$ a, and vice versa. It will cause no influence on conclusions.

[67] M. Lanoo and M. Bensoussan, Phys. Rev. B **16**, 3546 (1977)

[68] R. J. Kobliska and S. A. Solin, Solid State Commun. **10**, 231, (1972).

[69] H. Kawazoe, H. Tanagita, Y. Watanabe, and M. Yamane, Phys. Rev. B **38**, 5661 (1988).

[70] K. Tanaka and M. Yamaguchi, J. Non-Cryst. Solids **227-230**, 757 (1998).

[71] M. Yamaguchi, T. Shibata, K. Tanaka, J. Non-Cryst. Solids **232-234**, 715 (1998).

[72] Z. V. Popović and H. J. Stolx, phys. stat. sol. (b) **108**, 153 (1981).

[73] G. von Dittmar and H. Schäfer, Acta Crystallogr. , Sect. B : Struct. Crystallogr. Cryst. Chem. **32**, 2726 (1976).

[74] G. von Dittmar and H. Schäfer, Acta Crystallogr. , Sect. B : Struct. Crystallogr. Cryst. Chem. **32**, 1188 (1976).

[75] Z. V. Popović and Radŏs Gajić, Phys. Rev. B **33**, 5878 (1986).

[76] Zoran V. Popović, Z. Jakšić, Y.S.Raptis, and E.Anastassakis, Phys. Rev. B **57**,3418 (1998).

[77] R. Zallen, M. L. Slade, and A. T. Ward, Phys. Rev. B **3**, 4257, (1971).

[78] R. Zallen and M. L. Slade, Phys. Rev. B **9**, 1627, (1974).

[79] S. A. Boiko, D. I. Bletskan, and S. F. Terekhova, phys. stat. sol. (b) **90**, K49 (1978).

[80] Z. V. Popović and A. Breitschwerdt, Phys. Lett. **110A**, 426 (1985).

[81] L. H. Robins and M. A. Kastner, in *Optical Effects in Amorphous Semiconductors* , AIP Conf. Proc. No. 120, edited by P. C. Taylor and S. G. Bishop (AIP, New York, 1984), p. 183.

[82] L. H. Robins and M. A. Kastner, Phys. Rev. B **35**, 2867 (1987).

[83] J. Ristein, P. C. Taylor, W. D. Ohlsen, and G. Weiser, Phys. Rev. B **42**, 118 (1990).

[84] Y. Wang, T. Komamine, T. Nakaoka, O. Matsuda, K. Inoue, and K. Murase, J. Non-Cryst. Solids, **266-269**, 904-907 (2000).

[85] T. Nakaoka, Y. Wang, O. Matsuda, K. Inoue, and K. Murase J. Luminescence, **87-89**, 617-619 (2000).

[86] V. A. Vassilyev, M. Koós, and I. Kósa Somogyi, Philos. Mag. B **39**, 333 (1979).

[87] Y. Saitoh, Master Thesis, Osaka Univ. (1998).

[88] *Dynamics of Disordered Materials*, edited by D. Richter, A. J. Dianoux, W. Petry, and J. Teixeira, Springer Proceedings in Physics Vol. 37 (Springer Verlag, Berlin, 1989).

[89] *Relaxations in Complex Systems*, edited by K. L. Ngai and G. B. Wright (North Holland, Amsterdam, 1991).

[90] C. A. Angell, K. L. Ngai, G. B. Mckenna, P. F. Mcmillan, S. W. Martin, J. Appl. Phys. **88**, 3133 (2000).

[91] F. Fujara and W. Petry, Europhys. Lett. 4, 571 (1987); M. Kiebel, E. Bartsch, O. Debus, F. Fujara,W. Petry, and H. Sillescu, Phys. Rev. B 45, 10 301 (1992).

[92] B. Frick, D. Ritcher, W. Petry, and U. Buchenau, Z. Phys. B **70**, 73 (1988); B. Frick and D. Richter, Phys. Rev. B **47**, 14 795 (1993).

[93] T. Kanaya, T. Kawaguchi, and K. Kaji, J. Chem. Phys. **98**, 8262 (1993).

[94] J. Colmenero, A. Arbe, and A. Alegría, Phys. Rev. Lett. **71**, 2603 (1993).

[95] S. P. Love, A. J. Sievers, B. L. Halfpap, and S. M. Lindsay, Phys. Rev. Lett. **65**, 1792 (1990).

[96] Y. Tsuchiya, J. Non Cryst. Solids **122**, 205 (1990).

[97] R. Bohmer and C. A. Angell, Phys. Rev. B **45**, 10091 (1992).

[98] E. Rössler, A. P. Sokolov, A. Kisliuk, and D. Quitmann Phys. Rev. B **49** 14967 (1994).

[99] A. Brodin and L. M. Torell, J. Raman Spectrosc. **27** 723 (1996).

[100] M. Kruumlger, M. Soltwisch, I. Petscherizin, and D. Quitmann, J. Chem. Phys. 96, 7352 (1992).

[101] A. P. Sokolov, E. Roumlssler, A. Kisliuk, and D. Quitmann, Physica **A201**, 67 (1993).

[102] A. P. Sokolov, E. Roumlssler, A. Kisliuk, and D. Quitmann, Phys. Rev. Lett. **71**, 2062 (1993).

[103] G. Winterling, Phys. Rev. B **12**, 2432 (1975).

[104] V. Z. Gochiyaev, V. K. Malinovsky, V. N. Novikov, and A. P. Sokolov, Philos. Mag. B **63**, 777 (1991).

[105] S. N. Yannopoulos and G. N. Papatheodorou, Phys. Rev. B **62**, 3728 (2000).

[106] L. Saviot, E. Duval, N. Surovstev, J. F. Jal, and A. J. Dianoux, Phys. Rev. B **60**, 18 (1999); A. Fontana, R. Dellánna, M. Montagna, F. Rossi, G. Viliani, G. Ruocco, M. Sampoli, U. Buchenau, and A. Wischnewski, Europhys. Lett. **47**, 56 (1999).

[107] N. Theodorakopoulos and J. Jäckle, Phys. Rev. B **14** (1976) 2637; J. Jäckle, in *Amorphous Solids: Low Temperature Properties*, edited by W. A. Phillips (Springer, Berlin, 1981), p. 151.

[108] Ch. Simon, G. Faivre, R. Zorn, F. Batallan, and J. F. Legrand, J. Phys. I (France) **2**, 307 (1992).

[109] W. Gotze, in *Liquids, Freezing and the Glass Transition*, edited by J. P. Hansen, D. Levesque, and J. Zinn Justin (North Holland, Amsterdam, 1990); W. Gotze and L. Sjogren, Rep. Prog. Phys. **55**, 241 (1992).

[110] D. Caprion and H. R. Schober, Phys. Rev. B **62**, 3709 (2000).

[111] F. Mezei, W. Knaak, and B. Farrago, Phys. Rev. Lett. **58**, 571 (1987).

[112] R. Kohlrausch, Pogg. Ann. Phys. **91**, 198 (1854); G. Williams and D. C. Watts, Trans. Faraday Soc. **66**, 80 (1970); G. Williams, D. C. Watts, S. B. Dev, and A. M. North, ibid. **67**, 1323 (1971).

[113] J.G. Kirkwood, J. Chem. Phys. **7**, 505 (1939).

[114] P.N. Keating, Phys. Rev. **145**, 637 (1966).

[115] Y. Cai and M.F. Thorpe, Phys. Rev. **B** 40, 10535 (1989).

[116] Y. Wang, M. Nakamura, T. Nakaoka, O. Matsuda, K. Murase, J. Non-Cryst. Solids, to be published.

[117] D. J. Jacob, L. A. Kuhn, and M. F. Thorpe, in Ref. [9], p. 357.

[118] M. H. Cohen and G. S. Grest, Phys. Rev. B **20**, 1077 (1979).

[119] P. Boolchand, J. Grothaus, W. J. Bresser, and P. Suranyi, Phys. Rev. B **25**, 2975 (1982); P. Boolchand, J. Grothaus, and J. C. Phillips, Solid State Commun. **45**, 183 (1983).

[120] R. L. Cappelletti, M. Cobb, D. A. Drabold, and W. A. Kamintakahara, Phys. Rev. B **52**, 9133 (1995); M. Cobb, D. A. Drabold, and R. L. Cappelletti, Phys. Rev. B **54**, 12 162 (1996).

[121] C. Massobrio, A. Pasquarello, and R. Car, Phys. Rev. Lett. **80**, 2342 (1998).

[122] I. Petri, P. S. Salmon, and H. E. Fisher, Phys. Rev. Lett. **84**, 2413 (2000).

[123] K. M. Kandil, M. F. Kotkata, M. L. Theye, A. Gheorghiu, C. Senemaud, and J. Dixmier, Phys. Rev. B **51**, 17 565 (1995).

[124] K. Inoue, K. Kawamoto, and K. Murase, J. Non-Cryst. Solids **95&96**, 517 (1987).

[125] J. E. Griffiths, G. P. Espinosa, J. P. Remeika, and J. C. Phillips, Solid State Commun. **40**, 1077 (1981); Phys. Rev. B **25**, 1272 (1982).

[126] E. Haro, Z. S. Xu, J. F. Morhange, M. Balkanski, G .P. Espinosa, and J. C. Phillips, Phys. Rev. B **32**, 969 (1985).

[127] S. Sugai, Phys. Rev. Lett. **57**, 456 (1986).

[128] M. Nakamura, Y. Wang, O. Matsuda, K. Inoue, and K. Murase, J. Non-Cryst. Solids **198-200**, 740 (1996).

[129] T. Nakaoka, Y. Wang, K. Murase, O. Matsuda, and K. Inoue, Phys. Rev. B **61**, 15569 (2000).

[130] S. Susman, K. J. Volin, D. G. Montague, and D. L. Price, J. Non-Cryst. Solids **125**, 168 (1990).

[131] N. Afify, Phys. Rev. B **48**, 16 304 (1993).

[132] A. Feltz, H. Zickmuller, and G. Pfaff, in *Amorphous and Liquid Semiconductors*, edited by W. E. Spear (Centre for Industrial Consultancy and Liaison, University of Edinburgh, Edinburgh, 1977), p. 125; G. Lucovsky, R. J. Nemanich, and F. L. Galeener, ibid., p. 130.

[133] K. Sakai, K. Yoshino, A. Fukuyama, H. Yokoyama, T. Ikari, and K. Maeda, Jpn. J. Appl. Phys. **39**, 1058 (2000).

[134] S. Stølen, H. B. Johnsen, C. S. Bøe, T. Grande, and O. B. Karlsen, J. Phase Equilib. **20**, 17 (1999).

[135] P. Boolchand and W. J. Bresser, Phil. Mag. B, **80**, 1757 (2000).

[136] C. T. Moynihan and J. Schroeder, J. Non-Cryst. Solids **160**, 52 (1993).

[137] M. T. Cicerone and M. D. Ediger, J. Chem. Phys. **103**, 5684 (1995).

[138] D. N. Perera and P. Harrowell, Phys. Rev. E **54**, 1652 (1996).

[139] B. Doliwa and A. Heuer, Phys. Rev. Lett. **80**, 4915 (1998).

[140] K. C. Mills, in *Thermodynamic Data for Inorganic Sulphides, Selenides and Tellurides*, (Butterworths, London, 1974).

[141] I. Petri, P. S. Salmon, and W. S. Howells, J. Phys. Condens. Matter, **11**, 10219 (1999).

[142] I. T. Penfold and P. S. Salmon, Phys. Rev. Lett. **67**, 97 (1991).

[143] Q. Williams and R. Jeanloz, Science **239**, 902 (1988).

[144] P. H. Poole, T. Grande, C. A. Angell, and P. F. McMillan, Science **275**, 322 (1997).

[145] D. J. Lacks, Phys. Rev. Lett. **84**, 4629 (2000).

[146] O. Mishima and H. E. Stanley, Nature (London) **396**, 329 (1998).

[147] K. Murase and T. Fukunaga, in *Optical Effects in Amorphous Semiconductors*, edited by P. C. Taylor and S. G. Bishop, AIP Conf. Proc. No. **120** (AIP, New York, 1984), p. 449.

[148] U. Senapati and A. K. Varshneya, J. Non-Cryst. Solids **197**, 210 (1996).

[149] C. A. Angell, in *Relaxation in Complex Systems*, edited by K. L. Ngai and G. B. Wright (Off. Naval Res., Arlington, 1984), p. 3.

[150] C. A. Angell, J. Phys. Chem. Solids **49**, 863 (1988).

[151] G. Adam and J. H. Gibbs, J. Chem. Phys. **43**, 139 (1965).

[152] M. Goldstein, J. Chem. Phys. **51**, 3728 (1969).

[153] C. A. Angell *et al.*, in *Slow Dynamics in Condensed Matter*, edited by K. Kawasaki, M.Tokuyama, and T. Kawakatsu, AIP Conf. Proc. **256** (AIP, New York, 1992), p. 4.

[154] T. Nakaoka, Y. Wang, O. Matsua, K. Inoue, and K. Murase, J. Non-Cryst. Solids, to be published.

[155] S. C. Moss and D. L. Price, in *Physics of Disordered Materials*, edited by D. Adler, H. Fritzsche, and S. R. Ovshinsky (Plenum, New York, 1985), p. 77.

[156] S. R. Elliott, J. Non Cryst. Solids **97–98**, 159 (1987).

[157] S. Susman, D. L. Price, K. J. Volin, R. J. Dejus, and D. G. Montague, J. Non Cryst. Solids **106**, 26 (1988).

[158] I. T. Penfold and P. S. Salmon, J. Phys. Condens. Matter **2**, SA233 (1990).

[159] O. Uemura, Y. Sagara, and T. Satow, Phys. Status Solidi A **32**, K91 (1975); O. Uemura, Y. Sagara, D. Muno, and T. Satow, J. Non-Cryst. Solids **30**, 155 (1978).

[160] L. E. Busse and S. R. Nagel, Phys. Rev. Lett. **47**, 1848 (1981).

[161] L. E. Busse, Phys. Rev. B **29**, 3639 (1984).

[162] S. R. Elliott, Europhys. Lett. **19**, 201 (1992).

[163] C. I. Nicholls and H. M. Rosenberg, J. Phys. C **17**, 1165 (1984).

[164] A. Fontana, F. Rocca, and M. P. Fontana, Phys. Rev. Lett. **58**, 503 (1987).

[165] S. Alexander and R. Orbach, J. Phys. (Paris) Lett. **43**, L625 (1982).

[166] E. Duval, A. Boukenter, and T. Achibat, J. Phys. Condens. Matter **2**, 10227 (1990).

[167] A. Boukenter and E. Duval, Phil. Mag. B **77**, 557 (1998).

[168] T. Achibat, A. Boukenter, E. Duval, G. Lorenz, and S. Etienne, J. Chem. Phys. **95**, 2949 (1991).

[169] T. Achibat, A. Boukenter and E. Duval, J. Chem. Phys. **99** 2046 (1993).

[170] T. Ohsaka and T. Ihara, Phys. Rev. B **50** 9569 (1994).

[171] M. Nakamura, O. Matsusa, Y. Wang, and K. Murase, Physica B **263 & 264**, 330 (1999).

[172] E. Duval, N. Garcia, A. Boukenter, and J. Serughetti, J. Chem. Phys. **99** 2040 (1993); M. Montagna, G. Viliani, and E. Duval, J. Raman Spectrosc. **27** 707 (1996).

[173] A. P. Sokolov, U. Buchanau, W. Steffen and A. Wischnowski, Phys. Rev. B **52** R9815 (1995).

[174] A. P. Sokolov, A. Kisliuk, D. Quitmann, and E. Duval, Phys. Rev. B **48**, 7692 (1993).

[175] M. J. Stephen, Phys. Rev. 187, **279** (1969).

[176] S. Alexander, E Courtens, and R Vacher, Physica A **195**, 286 (1993).

[177] Y. Shi and C. Gong, Phys. Rev. A **46**, 8009 (1992); Phys. Rev. E **49**, 99 (1994).

[178] S. G. Louie, Phys. Rev. B **26**, 5993 (1982).

[179] H. Oheda, Jpn. J. Appl. Phys. **18**, 1973 (1979).

[180] S. G. Bishop, U. Strom, and P. C. Taylor, Phys. Rev. Lett. **34**, 1346 (1975); Phys. Rev. B **15**, 2278 (1977).

[181] D. K. Biegelsen and R. A. Street, Phys. Rev. Lett. **44**, 803 (1980).

[182] A. V. Kolobov, H. Oyanagi, Ka. Tanaka, and Ke. Tanaka, Phys. Rev. B **55**, 726 (1997).

[183] A. V. Kolobov, H. Oyanagi, A. Roy, and Ka. Tanaka, J. Non-Cryst. Solids, **232-234**, 80 (1998).

[184] A. Ganjoo, K. Shimakawa, N. Yoshida, T. Ohno, A. V. Kolobov, and Y. Ikeda, Phys. Rev. B **59**, 14856 (1999), and references therein.

[185] D. E. Aspnes, J. C. Phillips, K. L. Tai, and P. M. Bridenbaugh, Phys. Rev. B **23**, 816 (1981).

[186] M. Cardona, in *Light Scattering in Solids II*, edited by M. Cardona, and G. Güntherodt (Springer-Verlag, Berlin, 1982).

[187] V. A. Vassilyev, M. Koós, and I. Kósa Somogyi, Sov. Phys. Solid State, **31**, 782 (1989).

[188] Y. Wang, Doctral Thesis, Osaka Univ. (1997).

[189] C. Jodemchrov and S. Parvanov, Mater. Chem. Phys. **21**, 455 (1989).

[190] S. R. .Ovshinsky, in Ref. [5], Chap. 12, p. 729.

[191] S. O. Kasap and J. A. Rowlands, in Ref. [5], Chap. 12, p. 781;

[192] M. Mitkova, in Ref. [5], Chap. 12, p. 813.

[193] A. Lehmann, E. Broese, and B. Schroter, Phys. Status Solidi B **162**, K53 (1991).

[194] P. Galarneau, C. Maluin, A. Singh, and R. A. Lossard, Appl. Opt. **27**, 4591 (1988).

[195] K. C. Tai, W. R. Sanclair, R. G. Vadimsky, and J. M. Maron, J. Vac. Sci. Technol. **16**, 1977 (1979).

[196] B. Schroter, M. Abraham, E. Broese, P. Weissbrodt, and N. Malcher, Surf. Interface Anal. **14**, 835 (1989).

[197] E. B. Wilson, Jr., J. C. Decius, P. C. Cross, *The Theory of Infrared and Raman spectra* (McGraw-Hill, New York 1955).

[198] M. Wolkenstein, Compt. Rend. Acad. Sci. URSS, **34**, 185 (1941).

[199] W. Hayes and R. London, *Scattering of Light by Crystals* (Wiley, New York, 1978).

[200] B. J. Berne and R. Pecora, *Dynamic Light Scattering* (Wiley, New York, 1976).

[201] For a general review, see, S. Havlin, in *The Fractal Approach to Heterogeneous Chemistry*, edited by D. Adler (John Wiley & Sons, 1989), p251.

[202] P. G. de Gennes, J. Phys. (Paris) Lett. **37**, L1 (1976).

[203] H. J. Herrmann and H. E. Stanley, Phys. Rev. Lett. **53**, 1121 (1984).

[204] K. Yakubo, E. Courtens, and T. Nakayama, Phys. Rev. B **42**, 1078 (1990).

[205] A. Aharony, S. Alexander, O. Entin Wohlman, and R. Orbach, Phys. Rev. B **31**, 2565 (1985).

[206] S. Feng, Phys. Rev. B **32**, 5793 (1985).

[207] A. Rahmani, C. Benoit, E. Royer-Vilanova, and G. Poussigue, J. Phys. Condens. Matter **5**, 7941 (1993).

List of publications

1. T.Nakaoka, Y.Wang, O.Matsuda, K.Inoue, and K.Murase, "Relaxation process of band edge exciton in layered crystalline $GeSe_2$", J. Luminescence, **87-89**, 617-619 (2000).

2. T.Nakaoka, Y.Wang, O.Matsuda, K.Inoue, and K.Murase, "Resonant Raman scattering in crystalline $GeSe_2$", Phys. Rev. B **61**, 15569-15572 (2000).

3. Y.Wang, T.Komamine, T.Nakaoka, O.Matsuda, K.Inoue, and K.Murase, "Effect of thermal annealing on dynamics of photoluminescence in a–$GeSe_2$ films"', J. Non-Cryst. Solids, **266-269**, 904-907 (2000).

4. T.Nakaoka, Y.Wang, O.Matsuda, K.Inoue, and K.Murase, "Structural Reconstruction Followed by Crystallization in $GeSe_2$ Glasses", J. Non-Cryst. Solids, (in printing).

5. Y. Wang, M. K. Nakamura, T. Nakaoka, O. Matsuda, K. Murase, "Thermal relaxation of Ge-Se glasses and connectivity of network", J. Non-Cryst. Solids, (in printing).

6. T. Nakaoka, Y. Wang, O. Matsuda, K. Inoue, K. Murase, "Correlation of structural relaxation at glass transition with network connectivity in Ge_xSe_{1-x} glasses", Proceedings of 25th International Conference on the Physics of Semiconductors, Osaka, (in printing).

7. T. Nakaoka, Y. Wang, O. Matsuda, K. Inoue, K. Murase, "Reversible photoinduced structural changes in $GeSe_2$ glass at low temperature", Proceedings of 25th International Conference on the Physics of Semiconductors, Osaka, (in printing).

8. Y. Wang, M. Nakamura, T. Nakaoka, O. Matsuda, K. Murase, "Stiffness transition and connectivity in amorphous chalcogenide semiconductors", Proceedings of 25th International Conference on the Physics of Semiconductors, Osaka, (in printing).

9. T. Nakaoka, Y. Wang, K. Inoue, and K.Murase, "Trifurcated crystallization and inhomogeneity in $GeSe_2$ glass", Phys. Rev. B, submitted.

10. Y. Wang , T. Nakaoka, K. Murase, "Thermal relaxation and criticality of the stiffness transition", in *Phase Transitions and Self-Organization in Electronic and Molecular Materials*, edited by J. C. Phillips and M. F. Thorpe (Kluwer Academic/ Plenum Publishers), (in printing).